DYNAMICS OF HARD AND SOFT COLLOIDS IN CONFINED

GEOMETRIES AND ON STRUCTURED SURFACES

A Dissertation
Presented to
The Academic Faculty

by

Sri Charan Yarlagadda

In Partial Fulfillment
of the Requirements for the Degree
Doctor of Philosophy in the
School of Chemical & Biomolecular Engineering

Georgia Institute of Technology
August 2015

DYNAMICS OF HARD AND SOFT COLLOIDS IN CONFINED

GEOMETRIES AND ON STRUCTURED SURFACES

Approved by:

Dr. Victor Breedveld, Advisor
School of Chemical & Biomolecular
Engineering
Georgia Institute of Technology

Dr. Sven Behrens
School of Chemical & Biomolecular
Engineering
Georgia Institute of Technology

Dr. Michael Filler
School of Chemical & Biomolecular
Engineering
Georgia Institute of Technology

Dr. Yulin Deng
School of Chemical & Biomolecular
Engineering
Georgia Institute of Technology

Dr. Alberto Fernandez-Nieves
School of Physics
Georgia Institute of Technology

Date Approved: April 29, 2015

Dedicated to my beloved wife Keerti and my beloved mom & dad.

In loving memory of my sister:

Sri Chandana.
(December 19, 1986 ~ July 16, 2002)

ACKNOWLEDGEMENTS

I would like to express my special appreciation and thanks to my advisor Professor Dr. Victor Breedveld, for his constant support and able guidance. I would like to thank him for all the time he spent with me encouraging my research and for allowing me to grow as a research scientist. His advice, both research-wise and career-wise have been extremely helpful. I would also like to thank my committee members, Dr. Michael Filler, Dr. Sven Behrens, Dr. Alberto Fernandez and Dr. Yulin Deng for serving as my committee members and for all the research ideas they bestowed on me. In addition, I would like to thank them for letting my defense be a pleasing event, and for their intellectual comments and suggestions. I would especially like to thank my research group (both past and present members) for supporting me throughout my defense and also for being a huge helping hand in all my research activities. In addition, I would also like to thank NSF as it was the primary source of my funding, without which this work would not have been possible.

A special thanks to my parents for their unconditional love and support throughout my career. All the words in the world cannot describe how grateful I am to them for all of the sacrifices they made on my behalf. I would also like to thank all of my friends especially Swetha and Rajiv who constantly motivated me to reach my goal and for also being my writing buddies during the last few weeks. I am indebted to Karthik for helping me with my introduction section by proofreading it. I would also like to thank Keerti (now also my wife), Anusha, Bhavana, Praneeth & family, and Anirrudh for being my closest friends and making my life in Atlanta memorable. In the end, I would like express my

deepest appreciation to the joy of my life, my wife Keerti who gave me love, happiness,

hope, supported me during the difficult times and also helped me with my writing.

TABLE OF CONTENTS

LIST OF TABLES

LIST OF FIGURES

LIST OF SYMBOLS

D	Bulk diffusion coefficient
ζ	Zeta potential
κ	Debye-Hückel parameter
κ^{-1}	Debye length
σ	Surface charge density
ψ_0	Surface potential
N_A	Avogadro number
c_i^{∞}	Concentration of ions of type i
z_i	Valency of the ion
ε	Dielectric constant
ε_0	Permittivity of free space
k_B	Boltzmann constant
T	Temperature
ψ_d	Potential at the diffuse layer
Ω^{ss}	Repulsive electrostatic energy between two spheres
R	Radius of a sphere
R_g	Radius of gyration
d	Diameter of a particle
η	Viscosity
R_H	Hydrodynamic radius
MSD	Mean squared displacement
τ	Lag time

d	dimensionality
R_L	Radius of large-sphere
R_S	Radius of small-sphere
r	Center to center separation
Π	Osmotic pressure
Φ	Volume fraction
c	Concentration
R	Ideal gas constant
M	Molecular weight of solute
A_2	Second virial coefficient
A_3	Third virial coefficient
ΔV	Overlap volume
ζ	Correlation length
x	Distance of separation
Δr	change in radius
$V(db)$	Dumbbell-dumbbell overlap volume
$V(cyl)$	Cylinder-cylinder overlap volume
I	Ionic strength
C^*	Threshold concentration for molecular overlap
U	Depletion interaction energy
f	Drag coefficient
F	Force
v	Speed
Ca	Capillary number
ΔG	Gibbs free energy

ΔG_o	Osmotic contribution to Gibbs free energy
ΔG_i	Interfacial free energy contribution to Gibbs free energy
ϕ_p	Volume fraction of polymer
m_{AP}	Ratio of equivalent number of molecular segments of solvent to polymer
χ_{AP}	Flory-Huggins parameter
γ	Interfacial energy
$\bar{V}_A$	Molar volume of the solvent
V_f	Pervaded free volume
V_p	Volume occupied by the polymer
α	Fraction of free volume of the polymer
ρ	Drop density
ρ_p	Density of polystyrene
ρ_t	Density of toluene
V_s	Volume of swollen particle
V_i	Initial volume of the particle
K	Wall drag multiplier
$D_{||}$	Hindered lateral diffusivity
$f_/$	Hindrance coefficient near a rigid wall
h	Distance between the particle center and wall
$f_{||}$	Hindrance coefficient between two walls
H	Wall spacing
$\bar{f}_{||}$	Average hindrance coefficient between two walls
P_B	Boltzmann probability
L	Characteristic Boltzmann length

ρ_S	Density of a hard sphere
ρ_0	Density of fluid
F_D	Drag force
V_B	Absolute velocity of the drop centroid
D	Diffusivity
Pe	Peclet number
pK_a	Acid dissociation constant
R_N	Normalized radius
S	Shell thickness parameter
T_s	Thickness of the shell
R_c	Radius of the core
$\mathbf{R_{H,0}}$	Radius of the C/S microgel at standard conditions

LIST OF ABBREVIATIONS

2D	Two-dimensional
3D	Three-dimensional
AO	Asakura & Osawa
AAc	Acrylic acid
APS	Ammonium persulfate
BIS	N,N'-Methylene bisacrylamide
C_s	Salt concentration
C_p	Polymer concentration
CCD	Charged coupled device
CMC	Critical micelle concentration
CSR	Critical swelling ratio
C/S	Core/shell
DI	Deionized
DIC	Differential interference contrast
DLS	Dynamic light scattering
DLVO	Derjaguin-Landau-Verwey-Overbeek
DNA	Deoxyribonucleic acid
HCP	Hexagonal closed packing
ICP	Inductively coupled plasma
IDL	Interactive Data Language
LCST	Lower critical solution temperature
LSA	Linear superposition approximation

MKA	Morton-Kaizerman-Altier
MSD	Mean squared displacement
MW	Molecular weight
NIPAm	N-isopropylacrylamide
PCS	Photon correlation spectroscopy
PD	Polydispersity
PDMS	Polydimethylsilosane
PEG	Poly(ethylene glycol)
PEO	Poly(ethylene oxide)
PMMA	Poly(methyl methacrylate)
pNIPAm	Poly(N-isopropylacrylamide)
pNIPAm-co-AAc	Poly(N-isopropylacrylamide-co-acrylic acid)
PPO	Poly(propylene oxide)
PS	Polystyrene
PTVM	Particle tracking video microscopy
SDS	Sodium dodecyl sulfate
SR	Swelling ratio
STS	Surface technology systems
TIRM	Total internal reflection microscopy
VLS	Vapor-liquid-solid
VPT	Volume Phase Transition

SUMMARY

In this thesis, we are interested in investigating the interactions of colloidal particles with each other and with the neighboring confining walls. In particular, our main focus lies on the depletion interactions and hydrodynamic interactions in confined geometries. For the first part of the thesis, we look into the modeling and experimental studies of particle-particle and particle-surface depletion interactions in the bulk and on various geometries of interest. Most current applications for depletion interactions involve the method of destabilization of colloidal dispersions using a depletant to create large aggregates, which can subsequently be removed through filtration processes. Our interest lies in a more sophisticated application: modeling and experimentation of shape-selective interactions to depict depletion-induced self assembly as a viable way to fabricate various 2D/3D architectures on the nano- and microscale. We first used numerical modeling to compute depletion interaction strengths for simple geometries which eventually guided our experiments to make interactions highly selective. The model helped us in identifying the important parameters to finetune these interactions and shed light on geometric design rules to optimize desirable shape-selective interactions on a variety of complex geometries. The modeling studies combined with the experimental studies provided us with an understanding of how these interactions operate.

The second part of the thesis reports experimental studies that highlight the differences between hard and soft colloids, and particularly focuses on their confinement dynamics. While hard sphere suspensions have been the most widely studied colloidal

system, most colloidal systems in the real world exhibit softness: emulsions, microgels, star polymers, surfactant micelles etc. Despite their ubiquity, the confinement dynamics of soft sphere systems is relatively poorly understood. Therefore, the focus of our research was to investigate the impact caused by confinement on the dynamics of soft sphere systems. For this purpose, we developed a simple yet effective experimental setup which uses monodisperse silica spacers to create uniform confinement cells that entrap the hard and soft sphere systems while allowing measurement of hindered diffusivities via video microscopy and particle tracking. It was found that both soft sphere systems that we investigated (swollen polymer particles, core/shell microgels) behave differently from hard sphere systems under all degrees of confinement that were measured. While the nature of softness for the swollen polymer particles is that they have drop-like characteristics (deformable, interfacial mobility), microgels particles are characterized by a porous structure (deformable, compressible). The nature of the soft spheres used allowed us to vary the softness of the particles, i.e. through the swelling ratio of the swollen polymer particles and via the cross-linker concentration and shell thickness in the case of microgels. Both systems were found to show hard-sphere-like confinement behavior in the limit of decreasing softness.

Chapter 1

Introduction

1.1 Colloids

If one of the fundamental states of matter (solids, liquids, and gases) is finely dispersed in another then we have what we call a 'colloidal system'. Colloidal systems are so ubiquitous in our everyday life that we take them for granted. For example, blood, paint, smoke, ink, cosmetics, lubricants, pharmaceutics, and many food dispersions such as ketchup, milk, and mayonnaise are all colloidal systems that take advantage of some of the unique properties of colloids. A thorough knowledge of colloidal behavior is relevant and desirable, because of their paramount importance in terms of design and operation of these products that we use every day. The study of colloidal behavior aims to obtain a better understanding of their stability, interactions, flow behavior and phase behavior, so that we can manipulate the materials to suit our needs. The classification of colloids is done based on the particle size and is independent of the material or shape of the particles. As long as they fall in the size range 1nm to 10 μm, colloids can consist of any kind of material and can come in many shapes like spheres, ellipsoids, rods, etc. On the microscopic lengthscale, colloidal particles exhibit a constant, ceaseless, irregular motion, which can be described mathematically as a stochastic process and is usually referred to as Brownian motion. Due to continuous thermally driven collisions between solvent molecules and colloidal particles, they exhibit this kind of motion driven by energy of magnitude $k_B T$. Because of this, Brownian motion is oftentimes cited as an indirect proof for the existence of the atoms and molecules [1]. At any moment in time,

the discrete collisions endured by a colloid particle with surrounding molecules from all directions are not evenly distributed, which results in net random displacements that lead to self-diffusion of the colloidal particles in the surrounding medium. Typically, colloidal particles are sufficiently large and slow to be observed by optical techniques, such as conventional light microscopy. Therefore, colloidal suspensions are used as model systems for complex atomic systems and processes such as nucleation [2], growth, and melting of crystals [3]. The colloids employed in this thesis are fluorescent spherical particles with diameters of roughly a micrometer. Therefore, for all experiments, colloidal dynamics could be investigated with optical fluorescence microscopic techniques, giving direct observations of the phenomena being studied.

The science of colloids is firmly rooted in the interfacial behavior of the colloids and has been widely investigated over the last few decades. The field of Interfacial science is fundamentally concerned with how colloids and their assemblies behave structurally and dynamically on the nanoscale at or near interfaces, as opposed to the bulk. The major focus of our proposed work has to do with the non-bulk behavior of colloids. Colloidal suspensions are often bounded by walls and their behavior close to walls is quite different from the bulk because transport is typically hindered close to a surface. Due to this fact, a rich variety of processes like templated self-assembly [4], shear-induced resuspension [5] arise as hydrodynamic forces are paired with other particle-boundary interactions. The rich variety of colloidal interactions has been studied for a long time and it is still a very active field that deserves further investigation. The intricate microstructural configurations of suspended colloidal particles caused by interactions can lead to fascinating phenomena like colloidal self-assembled monolayers, colloidal micelles

2

formation etc. There are many forces that play an important role in the interaction of colloids including excluded volume interactions, electrostatic interactions, and van der Waals forces. In this thesis, we study the 'non-bulk' colloid-surface interactions mediated by two different phenomena: (1) Entropically driven depletion induced interactions (due to presence of a non-adsorbing polymer), and (2) Wall hydrodynamic interactions of colloidal particles. The following section discusses the main interaction forces that govern colloidal systems at the microscopic level.

1.2 Forces in colloidal systems

The forces between colloidal particles and/or surfaces play an enormous role in the stability and behavior of colloidal systems. Some of the most important forces are van der Waals forces, electrostatic double layer forces, entropic depletion forces, solvation, and steric forces. The overall force acting on a colloidal particle can be obtained by summing all forces that are present in a particular system, with individual forces often counteracting each other. For example, the van der Waals forces are responsible for aggregation of colloids [6], and coalescence of emulsions/bubbles [7] while the electrostatic double layer forces are often exploited for the stabilization of emulsions and foams [8]. The combination of competing van der Waals and double layer forces in such systems is described effectively by the Derjaguin-Landau-Verwey-Overbeek (DLVO) theory [9, 10]. In the remainder of this section, we first examine the various intermolecular forces that can exist in colloidal solutions and then describe the effects of their combined actions in relation to the systems that are of specific interest for this thesis.

1.2.1 Van der Waals forces

The van der Waals forces originate at an atomic or molecular level and involve momentary attraction between molecules and atoms. They have a shorter effective range than double layer forces, but play an important role in numerous interfacial and colloidal phenomena like adsorption of materials (surfactants), aggregation, surface tension etc. The van der Waals force between two bodies of the same material (i.e. having the same dielectric constant) is always attractive. However, for two different bodies, the force can either be attractive or repulsive depending upon the medium between them. Therefore, the intervening medium has a very significant effect on the van der Waals attraction between two bodies. Van der Waals interaction between molecules consists of three components: (i) London dispersion force (interaction between two induced dipoles) (ii) Keesom orientation force (interaction between two permanent dipoles) and (iii) Debye induction force (interaction between one permanent dipole and one induced dipole). Each of these three components has an interaction energy that varies with the inverse sixth power of the distance. The London dispersions forces are always present and are usually the most important of these three components because they exist between all atoms and molecules, even the non-polar molecules. Although the time-averaged dipole moment of the non-polar molecules is zero, fluctuations in the electron density in the molecules will cause temporary dipoles resulting in London dispersion forces. These forces can operate up to a range of ~10 nanometers. The Debye and Keesom interaction forces, on the other hand, have a smaller range but can also be important in interfacial phenomena but their existence depends upon the properties of the molecules. We will not be discussing the van der Waals forces and their mathematical expressions in detail. For additional details

about each of these three components, we refer the reader to the in-depth discussion provided by Israelachvili [11].

1.2.2 Electrostatic forces

Colloidal particles often carry an electrical charge to enhance their stability against aggregation. The presence of electrostatic double layer surrounding the particles results in a repulsive barrier barring them from approaching each other closely enough to aggregate. The electrical properties of colloidal dispersions lead to some of the most important electrokinetic phenomena in colloidal science, such as electrophoresis, electroosmosis and streaming potential. The electrostatic double layer due to the presence of surface charge is responsible for all these electrokinetic phenomena. The surface charge of the colloid particles is expressed in terms of the zeta potential (ζ), which is one of the elements which quantify the stability of the colloid system. There are many origins of this surface charge like ionization of surface groups [12] and adsorption of charged species (polyelectrolyte or ionic surfactants) [13], depending on the nature of the particle and also its surrounding medium. The acquiring of a net surface charge affects the distribution of ions in the surrounding region, resulting in a Coulombic attraction and increased concentration of counterions close to the surface, thus forming an electrical double layer around each particle. At the same time, osmotic pressure drives the counterions away from the surface, resulting in a balance between the Coulomb attraction and osmotic repulsion. Note that the overall colloidal system must be electrically neutral, since the surface charge is always balanced by an equal amount of opposite charge in the continuous phase. The electrostatic double layer close to the surface is consists of two regions with distinct physiochemical properties: the inner Stern layer and the outer Gouy-

Chapman layer. The Stern layer contains packed, adsorbed ions that are usually immobile due to strong chemical interactions. This compact layer is usually described as a monolayer formation and therefore modeled using a Langmuir isotherm. The outer Gouy-Chapman layer, on the other hand, has more loosely associated ions and is referred to as diffuse; its thickness is described by the Debye screening length (represented by κ^{-1} where κ is known as Debye-Hückel parameter). The thickness of the diffuse layer decreases with an increase in electrolyte concentration due to the enhanced screening of charges at the interface. The mathematical modeling of the diffuse double layer will not be discussed in great detail here, but, broadly speaking, charged surfaces can be characterized by their surface charge density σ and surface potential ψ_0. To describe the variation of potential from the surface or distribution of ions in the solutions, one must solve the Poisson-Boltzmann equation, a non-linear second order partial differential equation that requires two boundary conditions. Although there is no general solution of this equation, in the limit of low, constant surface potential ψ_0, the solution predicts an asymptotic far field behavior and an exponentially decaying profile for ψ with the distance x:

$$\psi \approx \psi_0 e^{-\kappa x} \tag{1.1}$$

The Debye length can be calculated from the following equation,

$$1/\kappa = \left[\frac{N_A e^2}{\varepsilon \varepsilon_0 k_B T} \sum_i z_i^2 \, c_i^\infty \right]^{-1/2} \tag{1.2}$$

where c_i^∞ is the concentration of ions of type i expressed in mol/m³, N_A is the Avogadro number, e is the electronic charge, z_i is the valency of the ion, ε is the dielectric constant of the medium and ε_0 is the permittivity of the free space, $k_B T$ is the product of the Boltzmann constant, k_B, and the temperature, T. The summation must be carried out over all ion species in solution. Debye screening length is inversely proportional to electrolyte concentration and valency of electrolyte, so that increases in those parameters cause a rapid decay of the electric potential, as schematically illustrated in Figure 1.1. However, Equation 1.1 is invalid when the potential is not small and a complete solution of the Poisson-Boltzmann equation allows for a better description of the variation of potential with distance from the surface. For our numerical formulations, we considered Stern theory over Gouy-Chapman theory as it is more advanced because it distinguishes between the total double layer potential (ψ_0) and the potential at the diffuse layer (ψ_d). Using Stern theory, linear superposition approximation [14] and Derjaguin
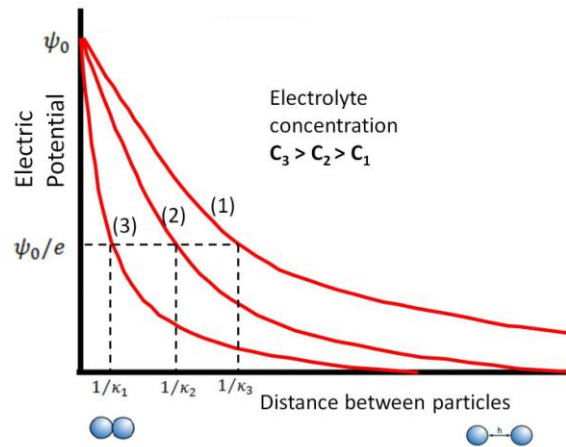
Figure 1.1 Potential as a function of distance between the particles. Debye length ($1/\kappa$) is the distance at which the potential, ψ_0 has dropped to (1/e) of its value at the surface ψ_0.

approximation, the repulsive energy of interaction between two spheres (Ω^{ss}) of radius R is given by,

$$\Omega^{ss} = 64\pi R \, k_B T n^\infty \kappa^{-2} tanh^2 \left(\frac{ze\psi_0}{4k_B T}\right) \exp(-\kappa x) \qquad (1.3)$$

where x is the distance of separation between the two spheres. It is important to understand the electrostatic interaction energy between two particles in order to model the overall colloidal interaction between them. In the next section, we will see how we can combine the interaction potentials in colloidal systems to qualitatively explain their behavior as a function of separation distance.

1.2.3   Forces in colloid-polymer mixture

For the case of binary colloid-polymer mixture, different kinds of forces can exist depending on the kind of interaction between the colloids and polymer molecules. When polymer molecules are added to a colloidal suspension, two possible situations arise: *a)* the polymer molecules adsorb onto the surface of the colloid, where the polymer chains can induce attractive bridging forces between the colloids, repulsive steric repulsive forces   (caused by the unfavorable entropic penalty associated with compression or overlap of polymer chains), or *b)* the polymer molecules are non-adsorbing and can act as smaller colloidal particles (assuming they exist as random coils in the given solvent with a radius of gyration R_g) that can generate depletion interactions (entropic in origin) between the bigger colloids. When the separation between the two big colloidal particles is less than the hydrodynamic diameter of the polymer, depletion

8

of the latter from the gap between the colloids leads to anisotropy of the local osmotic pressure, which gives rise to an attractive depletion force between the colloids. A great deal of our research work has to do with depletions interactions in colloid-polymer mixtures [15, 16]. In Chapter 2, a versatile new approach for calculating the depletion potential between hard spheres and various simple and complex geometries is presented; the depletion interactions will be described in more detail there. In Chapter 3, experimental studies on depletion interactions are carried out.

1.2.4 Miscellaneous forces

Other important colloidal forces include solvation forces (hydrogen bonding) and hydrophilic/hydrophobic forces. At very short range of separations (a few nanometers), forces such as the solvation forces arise when a liquid is confined in a highly restricted space between two surfaces. The strength of such forces can be even greater than the DLVO forces and hence cannot be ignored. The solvation forces arise mainly due to the arranging of the solvent molecules into semi-ordered layers between the surfaces, which results in repulsive forces caused by the hydrated groups at the surfaces when they approach each other. This short range stabilizing force was observed between solid surfaces, such as silica and mica, across water [17, 18] and was also found to stabilize certain soap films in salty media [19] and biomembrane interactions [18]. Therefore, at short separations, prevention of coagulation was explained by the presence of these short-range repulsive forces. Hydrophilic/hydrophobic forces are also significant in colloidal systems. The origin of these forces can be explained by strong electrostatic cohesion in water molecules. Water molecules tend to form hydrogen bonding with each other, thus excluding non-polar molecules that are incapable of forming hydrogen

9

bonding, e.g.alkanes, hydrocarbons, and fluorocarbons. For this reason, hydrocarbons and halocarbons are poorly soluble in water and separate out in different phases due to what we call "hydrophobic effect".

1.3   Effective interaction potential in colloid-polymer mixtures

Aside from DLVO interaction potentials, colloidal particles also experience entropy induced depletion attractive (sometimes repulsive) potential in the presence of non-adsorbing polymers, the colloidal particles also. Therefore, the net effective potential in these systems should be summation of van der Waals attraction potential, electric repulsion potential (assuming charged particles and surfaces) and depletion potential (see Figure 1.2). In the following chapters, we will try to manipulate the effective potential to
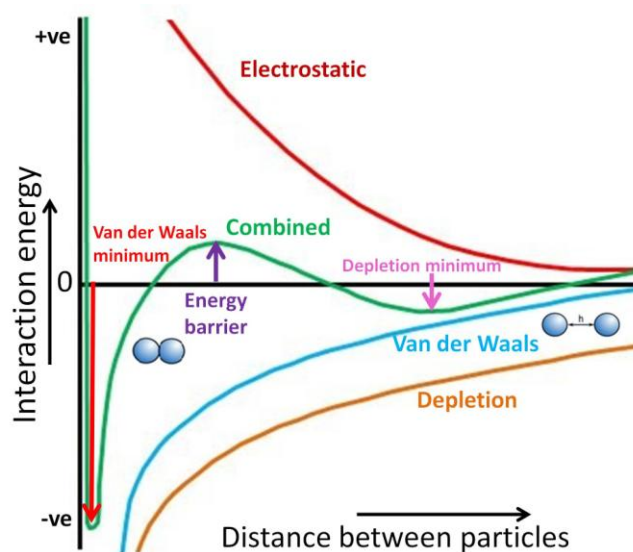
Figure 1.2 A schematic of the van der Waals (blue), electrostatic (red), depletion (brown) and the effective interparticle potential (green) as a function of the interparticle distance. Figure also shows depletion and van der Waals minima.

suit our research needs. So it is important that we understand the characteristics of the effective interactive potential for the binary colloid-polymer mixtures. Consider the effective interaction potential between two colloidal particles or between a colloidal particle and a surface. At large distances of separation, all the individual potentials reduce to zero due to infinitesimal interactions and therefore the effective potential is insignificant. At a very small distance of separation is a deep minimum in the combined effective potential energy produced by the highly influential van der Waals attraction between the two surfaces. An electrostatic repulsive barrier is located a little farther away, as the electrostatic repulsion potential dominates the van der Waals attraction potential in this region. It should be noted that the repulsion is not directly due to the surface charge on particles, but it is due to the interaction between two double layers. We would want the electrostatic barrier to be large enough so that permanent particle aggregation would be avoided in the van der Waals minimum. The secondary minimum shown in the figure is formed due to the presence of depletion potentials which tends to be the influential potential at this distance of separation. If the secondary depletion minimum is established, the effective particle interaction potential can be manipulated to achieve different kinds of particle-particle or particle-surface interactions as we will see in Chapter 2.

1.4 Hydrodynamics of hard and soft colloids

In section 1.2 we discussed various static forces acting in colloidal suspensions. In contrast, hydrodynamic forces, as the name suggests, require dynamics of colloidal particles in order to exist between the particles and neighboring surfaces. Unlike the direct interactions between the particles and fluid, hydrodynamic forces originate from

the interactions of the intervening incompressible fluid molecules whose flow is influenced by the Brownian motion of other colloids or due to other solid interfaces. In short, they are caused by the two-way hydrodynamic coupling between the particles and fluid flow fields. Unlike van der Waals and electrostatic interactions, which have a unique relevance on colloidal length scales, hydrodynamic interactions are significant on macroscopic length scales as well and largely determined by boundary conditions for momentum transfer. A simple and intuitive example can be given in terms of the drag force experienced by a person swimming in a water body. A person swimming in a quiet ocean creates propagating flow fields and experiences a drag force due to hydrodynamic interactions. The same person swimming in a small pool will experience a different (higher) drag force due to the propagated fluid disturbances reflected from the boundary walls of the pool. Similarly, on the colloidal length scales, hydrodynamic forces are important because they control the both the mobility of particles in fluids and the fluid flow behavior. For example, in a concentrated suspension, the effective viscosity and the individual particle mobility depend to a great extent on the hydrodynamic as well as particle-particle interactions [20]. By contributing and responding to a fluid's local flow, colloidal particles experience hydrodynamic interactions with each other and with the confining walls. In the limit of low Reynolds number, for the case of unbounded hard spherical particles (in the dilute limit) with hydrodynamic radius R_H, Stokes-Einstein law gives

$$D = \frac{k_B T}{6\pi\eta R_H} \tag{1.4}$$

12

where η is the viscosity of the medium, D is the particle free diffusivity, T the temperature, k_B is the Boltzmann constant. By measuring the hydrodynamic drag of freely diffusing particles in an unbounded system, we can get useful physical information about the particles as well as the local fluid explored by them. The details of these measurement techniques will be discussed in the next section.

While most researchers agree with the predictions of the Stoke-Einstein relation for hard spheres, true hard spheres do not exist in reality. Few researchers have acknowledged the presence of intrinsic softness in hard-sphere-like systems [21, 22] and have asked the inevitable question "Are hard spheres really hard?" [21]. In terms of hydrodynamic interactions, the exact nature of "hardness" of the particles is incredibly important. When colloidal particles in a solution are moving towards each other or towards a solid interface, the lubrication film between the two interfaces has to thin out meaning, fluid has to escape. So the relevant question here is "What does it mean to be soft?" This is because softness can be appreciated from different perspectives: particle elasticity, particle porosity, variety of soft interactions, and particle volume fraction. To answer that, particle softness in our case pertains to a distinguishing feature which would basically provide the lubrication fluid alternative ways to escape from the lubrication gap. Softness can be of various origins. One form of softness is deformability, i.e. the surfaces of the particle can deform/compress under forces of relevant magnitude, such as the lubrication pressure. Another form of softness is interfacial mobility, which allows the lubrication fluid to move more freely because the no-slip boundary condition no longer exists. One last form of softness is particle porosity, which enables the suspending fluid to penetrate the interface of the particles. Softness can also arise from the interaction

potential, which permits some degree of compression beyond the effective radius of the particles [22]. This can occur as a consequence of the strong electrostatic or steric interactions used to keep the particles apart. Few examples of soft particles relevant to our definition can include emulsion drops, bubbles, microgels, vesicles and hairy particles (also known as polymer brush-grafted particles). All these materials have been known to pack more volume at close-packing compared to hard sphere suspensions due to their deformability [23]. Also, many researchers claim that the interfacial mobility of drops and bubbles diffusing in aqueous solutions can produce substantial differences in their hydrodynamic behavior compared to solid spheres or drops with immobile liquid interfaces [24, 25]. Based on this knowledge, one would expect that the particle softness should considerably reduce the drag experienced by the particle in presence of confining surfaces (or other particles). Despite this, such differences in hydrodynamic coupling behavior for hard and soft spheres is incompletely understood and often debated in the literature. It is therefore important that we understand the hydrodynamic interactions of soft and hard colloidal particles with the surrounding solid surfaces as they are relevant in a number of natural and practical applications like stability of emulsions [8], particle filtration [26], migration through porous media [27], and flow through the small channels of microfluidic devices [28].

In this thesis, we are interested in the latter research problem which is particle-wall hydrodynamics. Specifically, we investigate the effect of particle softness on the particle-wall hydrodynamic interactions by examining their Brownian motion in free and confined volumes. While Brownian motion of free particles is well understood, the dynamics of colloidal particles become a rich problem when wall hydrodynamics

14

becomes important. The presence of a solid wall imposes constraints on the flow field and affects the mobility of particles by hydrodynamic coupling. As a result, Brownian diffusion of colloids is hindered significantly near walls. Brenner [24] and Goldman *et al*. [29] were the first researchers to analytically solve the hindrance coefficients of a near-wall hard sphere using a lubrication formulation. We will discuss these numerical models in more detail in Chapter 4. One way to study these wall interactions experimentally is to measure the hindrance cause to diffusion due to confining walls for different confinement limits. Therefore, hindrance coefficients are obtained as a function of degree of confinement (wall spacing) and are compared for both hard and soft particles as we will see in Chapter 4. For these experiments, we use polystyrene microspheres as hard colloids, toluene-swollen polystyrene particles and core/shell (polystyrene/pNIPAm-co-AAc) microgels as soft colloids.

1.5 Particle tracking video microscopy

Over the past decade, microrheology has emerged as a valuabe technique to interrogate complex fluids at the smaller length scales. 'Microrheology' collectively describes a number of experimental techniques which have the capability to ascertain the rheological properties of complex fluids [30, 31]. While the traditional rheology (or macrorheology) procedures typically operate on a much larger (millimeter or more) length scales, microrheology operates on a much smaller length scales (micro or nano) which would also mean it has the added advantage of needing much smaller sample volumes. This is especially important with analyzing expensive or biological fluids which cannot be produced in large quantities. However, there are not always agreements between the microrheologically and macrorheologically measured properties of a

material. The disparities between the measurements can be indicative of these physically contrasting methods of investigating material properties. By looking closely into these differences in measurements, one might be able to learn more about the material properties.

Particle tracking video microscopy (PTVM) coupled with microrheology uses the mobility of colloidal 'probe' particles to extract information about the particles themselves or the rheological properties of the local environment explored by these particles. Experiments carried using PVTM techniques can be classifies into two modes: firstly, active microrheology which is active manipulation of the probe particles using externally applied forces and secondly, passive microrheology which involves using the intrinsic Brownian diffusive motion of the particles due to random thermal fluctuations of the environment. While passive microrheology can be used only to explore the near-equilibrium or linear response properties of a material, active microrheology is often used to study the nonlinear viscoelastic properties of a material as it involves using external forces like optical traps or magnetic tweezers to push the material out of equilibrium. Regardless of the mode carried out, PVTM identifies and analyzes the individual trajectories of the probe particles from which one can measure the mean-squared displacements. From the mean-squared displacement information, we can get useful physical information like the particle diffusivities, viscosity, frequency-dependent shear modulus of the material [32], temperature of the solvent [33], hydrodynamic radius, and micro-structural morphology/heterogeneity associated with the material [31].

PVTM has been utilized in many diverse systems like biophysics (such as DNA solutions), living cells, microfluidics, colloidal physics, rheology and polymer sciences.

A main advantage of using PVTM is that the information from the individual colloidal probes can be used to provide both ensemble-averaged as well as local spatially-resolved information of the system making. In the following sections, we will discuss this experimental technique in more detail. For this thesis, we primarily focus on the passive version of PTVM which consists of four major steps: recording a movie consisting of the diffusing colloidal particles, identifying particles in each frame of the movie using customized computational algorithms, integrating all the information from the individual frames to form trajectories of all the individual particles, and finally the statistical analysis of these trajectories to get useful physical information [34]. Depending on their needs, various research groups have developed in-house computational algorithms for detecting the positions of the colloidal probes. Usually, it involves one of the following four categories of image analysis algorithms: crosscorrelation, sum-absolute difference, centroid, and direct Gaussian fit [35]. The main difference between these methods is that centroid and direct Gaussian fit algorithms identify the particle positions from a single frame while the cross-correlation and sum-absolute difference algorithms do this by comparing the consecutive frames. In most cases, the centoid algorithm is known to be the most robust against pixel noise and the most fitting for micron size colloidal particles. For the current work discussed in this thesis, we used brightness-weighted centroid algorithm developed in Interactive Data Language (IDL; ITT Visual Information Solutions, Boulder, CO). A typical PTVM experiment for this work was carried out as follows. The Brownian motion of the probe particles in the appropriate samples were monitored via an optical microscope (Leica DM-IRB), and movies were recorded using a CCD camera (Cohu 4920, Poway, CA; 30 frame/s and 640×480 pixel resolution) and

copied directly onto the PC. A typical microrheology movie has 1500 images at 640x480 pixel resolution, so that the file size is 440 Mb. Because Brownian motion leads to small particle displacements on these timescales and is highly sensitive to external vibrational noise, all experiments were performed on a vibration-isolated optical table. Subsequently the recorded movies were analyzed with software developed using IDL. As already stated, we utilized a standard brightness-weighted centroid method to identify the particle trajectories in each frame. This method primarily uses four major steps: restoring the image, locating possible particle centers, refining particle positions/eliminating unwanted particles, and linking particle positions into trajectories [34]. The recorded videos consist of images that are distorted by noise which is a result of microscope optics and the imaging process during digitization. This noise can be minimized using computerized algorithms [36]. The first step aims to reduce spatial frequency noise and large background noise associated with the image. To this end, the images are brushed up to enhance contrast for the recognition of features of interest. The second step locates all the potential particle centers in all the images using the multiple brightness-weighted centroids. The third step applies additional refinement criteria such as eccentricity (aspect ratio) and minimum/maximum brightness to eliminate the particles that are too elongated or particles that are too faint because they are out of focus. This is a particularly effective screening criterion to have a true representative crowd of colloidal probes in the sample. For example, colloidal aggregates have higher eccentricity and brightness than single particles and are eliminated effectively using eccentricity and brightness as selection criteria. Often times, we include an extra step here which is to ensure that we have not induced pixel-biasing. A good description of the phenomenon is provided by Weeks

(http://www.physics.emory.edu/~weeks/idl/). The fourth step creates particle trajectories by linking particle positions from the particle position data for the individual images. Finally, the trajectories can be used for statistical analysis which can further be used to investigate various mechanical/physical properties of the colloidal suspensions. When analyzing these trajectories of colloidal particles, one can easily calculate the mean squared displacement (MSD) as a function of lag time, τ.

For Newtonian regimes, the general Einstein-Stokes relation makes it possible to relate the mean squared displacement of the particles, the mechanical/rheological properties of the medium, hydrodynamic radius of the particle and temperature of the medium. Therefore, for Newtonian fluids, the MSD of the particles as a function of the lag time, τ is given by:

$$MSD = \frac{d k_B T}{3 \pi \eta R_H} \tau \qquad (1.5)$$

where d is the dimensionality. Therefore, a linear relationship can be proposed using equation (1.3.1) with the slope being:

$$slope = \frac{MSD}{\tau} = \frac{d k_B T}{3 \pi \eta R_H} = 2dD \qquad (1.6)$$

Using this above equation, one can easily compute the ensemble-averaged diffusivities of the colloidal particles from the slope of the *MSD* versus lag time plot. Solving for the viscosity, η:

$$\eta = \frac{d \cdot k_B \cdot T}{3 \cdot \pi \cdot R_H \cdot slope} \tag{1.7}$$

Therefore, it should also be possible to calculate the viscosity of a Newtonian fluid using PVTM as long as the hydrodynamic radius of the colloidal probe particle is known. All the other terms in equation (1.4.3) are known or can be measured. In this thesis, we will use these above mentioned relations to estimate the free/hindered diffusivities and viscosities of the colloidal particles and solutions respectively from the *MSD* versus lag time plot.

1.6 Motivation and structure of the thesis

In this thesis, the 'non-bulk' colloid-surface interactions are mediated by two different phenomena: depletion interactions and hydrodynamic interactions of colloidal particles. By carefully fine-tuning the depletion interactions between colloids and surfaces, one can be exploit them for spontaneous organization of colloids on surface microstructures, which can result in the directed self assembly on the micro and nanoscale. Use of small particles to trap larger colloids on sharp corners on a wall was first demonstrated in a series of experiments by Yodh and coworkers [37]. In addition, researchers were able to use depletion forces to deposit particles on patterned templates [38] and onto highly anisotropic structures [39]. Therefore, depletion interactions may have the ability to enable fabrication procedures for materials based on self-organized structures with minimum effort and cost and for this reason it forms a strong motivation for this part of our thesis. Over the years, depletion interactions also paved way for

various other novel applications like fractionation of a bidisperse population of colloidal particles [16], possibility of a novel particle separation method [40] etc. It is quite fascinating that the addition of simple non-adsorbing polymer molecules to a colloidal suspension generates such ordered arrangements in the colloidal particles.

For the second half of the thesis, our motivation is mainly due to our fundamental interest to distinguish hard and soft sphere hydrodynamics under confinement. Also, wall hydrodynamics of soft colloidal particles are becoming an important area of interest, both scientifically and technically. In spite of the fact that soft colloidal systems are ubiquitous and understanding their hydrodynamics is vital to understand their behavior, the effects of confinement on the mobility of soft colloids are poorly understood when compared to hard colloids. Potential areas of application where the hydrodynamic interactions between soft colloidal systems and rigid surfaces is important are tribology of liquid-surface interactions [41], nanolubricants research [42], transport of oil drops in porous media, [43] emulsion flow in microfluidic devices [44, 45] and near-wall motion of drops in packed columns [46]. For example, the hardness of nanoparticles in nanolubricants is an important factor for consideration. It was found that soft nanoparticles results in significantly increased surface smoothness and lubrication behavior compared to hard nanoparticles [42].

The structure of this thesis is as follows. Chapters 2 and 3 are pertaining to the depletion phenomena while Chapters 4 and 5 are pertaining to the wall-hydrodynamic phenomena. In Chapter 2, we introduce the modeling aspect of the depletion attractions of colloids in confined systems and on structured surfaces. We will demonstrate the versatility of the numerical model used for calculating interaction potentials between

colloids and geometrical surfaces with increasing order of complexity. We demonstrate that the numerical model provides us with a certain design rules to optimize these shape-selective interactions. Chapter 3 focuses on the experimental studies of depletion interactions of colloids. Using a phase diagram, we show the rich variety of depletion interactions that were probed for colloid/polymer mixtures on flat and structured substrates as a function of polymer and electrolyte concentrations. Specifically, we show that selective deposition of colloids on different geometries can indeed be achieved. In chapter 4, by utilizing a confinement setup, we demonstrated the confinement effects on hard and toluene-swollen polystyrene beads in an effort to explain the fundamental differences in their hydrodynamic behavior. Excellent agreements for the hard sphere confinements with the numerical models establish the robustness of the experimental protocol. In chapter 5, we describe the confinement dynamics of the specially synthesized core/shell (polystyrene/pNIPAm-co-AAc). By varying the degree of softness in various different ways, we demonstrate the importance of particle softness in these systems. Finally, in chapter 6, the major conclusions of this thesis are presented and recommendations about future research directions are made.

CHAPTER 2

Theory and modeling of depletion attraction between colloids

in confined systems and on structured surfaces

2.1 Introduction

Self-assembly is the spontaneous ordering of building blocks which results in increased internal organization of a system; nature uses this process in cells (such as the self-assembly of the lipid bilayer membrane [47]) and other biological systems (e.g. DNA folding [48]). If we can mimic nature to exploit this phenomenon in an artificial environment, then we potentially have a scalable method to create complex, bottom-up nanoscale structures, instead of using conventional top-down methods like lithography, which are generally expensive and slow, and sometimes have a resolution that is limited by the wavelength of light [49]. But then, nanoscale colloids known as depletion agents can induce depletion attractions between larger colloids which arise solely from physical considerations of excluded volume to form hierarchical assembly dynamics in solution. Therefore, depletion interactions provide new avenues in the field of colloidal self-assembly.

Entropically-driven depletion interactions in colloidal systems are well-known and have been studied for decades [38, 50, 51]. Depletion forces are predominant in crowded colloidal environments where a significant volume of the system is occupied by a smaller species, such as macromolecules (polymers, proteins). Depletion interactions are abundant in nature (blood, milk, clay) and are of great interest for many industrial

23

applications like coatings and paints, drilling fluids, processing/preserving of food products [16], which all involve stabilization and transportation of colloidal dispersions. They are also important in many biological systems because the strength of depletion interactions is roughly comparable to the energy associated with one hydrogen bond in a protein (0.7 kcal/mol ~ 1 $k_B T$) [52]. Depletion forces are important because the addition of a smaller species (polymers/particles) to a colloidal dispersion can have a significant effect on the colloidal dynamics and their properties due to the introduction of depletion interactions. In this work, I restrict the experimental work and most of the discussion to the context where depletion interactions are induced by polymers in colloid-polymer mixtures (although, the term 'small-spheres' is used loosely in this chapter for theoretical/numerical modeling aspects and can often be replaced with polymer).

Depletion interactions exist due to the presence of this excluded volume around the bigger particles (depleted zone) that is inaccessible to the smaller particles in the suspension. Figure 2.1 shows a suspension of large (red) and small (green) particles in
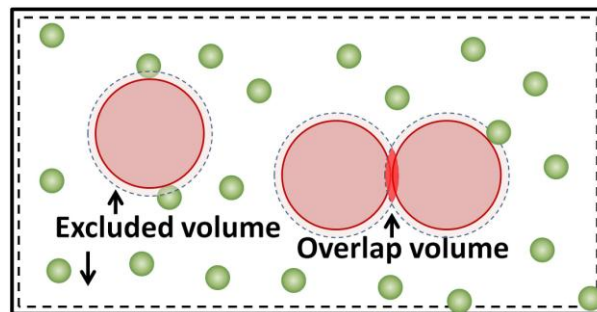
Figure 2.1 Depletion attractions between large-spheres in a suspension of small-spheres. The excluded volume regions indicated by dashed lines is inaccessible to the centre of mass of the small-spheres.

which an 'excluded volume' exists for the small-spheres around each large-sphere and along the walls. The dashed lines in Figure 2.1 denote the excluded volume around the spheres and near the wall. The loss of accessible volume for the small-spheres reduces the number of accessible configurations for the small-spheres, i.e. their entropy. The system then generates an entropic driving force that aims to minimize the excluded volume by promoting 'excluded volume overlap', which is the key concept for the depletion interactions. Pushing the larger colloids together or against other surfaces in the system, increases the overlap volume and maximizes the total accessible volume for the small-spheres, and hence their entropy. The entropy gain of the small-spheres/polymer dominates over the entropy loss of the large-spheres because of their larger number. Alternatively, the (attractive) depletion force can be explained as originating from an uncompensated (osmotic) pressure due to the expulsion of small-spheres/polymer from the gap between the colloidal particles. A unique characteristic of depletion interactions is that they provide us with ways to tune both the depth (strength) and the range of attractive interactions between the large colloids as we will see in their modeling aspect.

Colloids modeled as hard spheres usually lack attractive and long-range interactions. It is fascinating that the addition of smaller spheres/polymer induces interactions which can produce ordered phases for the hard spheres. Before they phase separate into solid crystal phases in the bulk or on a nearby surface, colloidal particles in the absence of polymer molecules are gas-like, diffusing freely in the solvent. Gast et al. has shown experimentally by careful manipulation of the colloid-polymer size ratio and attractive interactions, a stable colloidal liquid phase can also be achieved before a solid crystal phase for hard-sphere polymer mixtures [53]. These fragile liquid crystals are

25

formed with particles spatially arranged in the fluid and are separated by distances comparable to their size. It was shown that the liquid phase can only exist for a colloid-polymer size ratio less than 3. For larger ratios, only solid crystal phases are observed.

Depletion interactions are governed by entropic rather than enthalpic forces, and therefore are material independent. For example, the depleting agents can range from surfactant micelles [54], polymers [51, 55], proteins [56], solid particles [37, 57] as long as they do not adsorb onto the large colloids. Similarly, the underlying principles of depletion interactions should in essence be applicable to nano and macromolecular length scales although we only look into micro length scales in our current work. The discussion on depletion interactions in this thesis is divided into two chapters. In the present chapter we will look into the theory and numerical modeling of depletion interactions between colloids and various geometric surfaces of interest to assess the feasibility of self-assembly experiments. In the next chapter we will present the corresponding experimental results and also discuss how our numerical findings complement these experimental findings. In the following sections will provide some literature background and look into the theory of depletion interactions in more detail. Later on, we investigate how these interaction potentials can be computed using simple numerical models.

2.2 Motivation

The addition of small-spheres/polymer can change the phase behavior of the bigger spheres (by bringing more order in these systems). This property has a lot of practical implications. For example, depletion forces can influence suspension stability, and are of considerable importance in a wide variety of day to day materials ranging from

frozen desserts to paints to living cells[58]. Several novel and useful applications of the depletion interaction have also been demonstrated. For instance, waste water treatment plants use polymers to remove contaminant particles through depletion and bridging flocculation techniques [59]. Depletion flocculation is also used in clarification of drinks such as beer and wine, and in processing of minerals [60]. Zukoski *et al*. have shown that polyethylene glycol can induce crystallization and/or separation of protein solutions [61]. Polysaccharides have been used as thickening agents in milk products, where depletion attraction between casein and micelles arise from the presence of the polysaccharides [62]. Besides these existing practical implications, scientists are investigating depletion interactions in colloidal systems for novel applications like scalable fabrication on the nanoscale.

Therefore, most current applications for depletion interactions involve the method of destabilization of dispersions using a depletant, which are eventually removed through filtration processes. Our ultimate motivation to study the dynamics of colloid-polymer mixtures on structured surfaces is to address depletion induced self-assembly processes as a potentially scalable manufacturing method for preferential deposition of nanoscale building blocks onto surfaces. Use of small-spheres to manipulate larger colloids and confine them to a two-dimensional space next to a wall was first demonstrated in a series of experiments by Yodh and coworkers [58]. This methodology may certainly be useful in combining entropic forces and patterned template surfaces to influence the growth of two/three dimensional structures. An example is scalable fabrication of superlattice structures with nanoscale periodicity which can constitute the building blocks of many

novel nanoscale architectures in various related fields such as photovoltaics, thermoelectronics, plasmonics and optoelectronics [63].

2.3 Modeling of the depletion interactions

Asakura & Oosawa (1958) first noted the depletion effect between two bodies immersed in a solution of rigid spherical macromolecules [15]. Assuming that the rigid small-spheres behave as an ideal gas at low concentrations, they proposed a simple analytical model for the interaction potential in basic sphere-sphere geometry given by:

$$U(r) = \frac{4\pi}{3}(R_L + R_S)^3 \left(1 - \frac{3r}{4(R_L + R_S)} + \frac{r^3}{16(R_L + R_S)^3}\right) \Pi \qquad (2.1)$$

where R_L, R_S and r are the large-sphere radius, small-sphere radius and the center to center separation and Π is the Osmotic pressure of the small-spheres in suspension which is given by the dilute gas law, $3\Phi T/4\pi R_s{}^3$ where Φ is the volume fraction of the small-spheres. The Asakura & Oosawa (AO) model predicts that the energy of attraction is proportional to the volume fraction of the small-spheres and to the ratio of large to small-sphere diameter. In this model, rigid small-spheres can also represent non-adsorbing (ideal) polymer molecules [16]. Geometric correction factors can be used to modify this equation to account for the differences in overlap volume. Since the rigid small-spheres behave thermodynamically ideally, the osmotic pressure is given by the Van 't Hoff law:

$$\frac{\Pi}{c} = \frac{RT}{M} \qquad (2.2)$$

where c is the concentration in terms of the 'grams' of solute per liter, M is the molecular weight of the solute, R is the gas constant and T is the temperature of the system. By

28

"thermodynamically ideal", we mean a hypothetical solution in which the solute-solvent, solvent-solvent, and solute-solute interactions are all equivalent. For dilute and semi-dilute polymer solutions, such `ideal-gas-type' models might be expected to provide a good approximation of the physical system. For non-ideal situations, this relationship is a general power series expansion in c given by:

$$\frac{\Pi}{c} = RT\left[\frac{1}{M} + A_2c + A_3c^2 + \cdots\right] \qquad (2.3)$$

where A_2 and A_3 are the second and third virial coefficients which can be empirically determined for a given solute-solvent system. Several researchers have further extended these models to suit their specific problems of interest [55, 64]. At low concentrations of small-spheres, all the simple depletion models (Asakura & Oosawa 1958; Vrij 1976; Gast *et al.* 1983) [55, 64] work on the proposition that the attraction potential is directly proportional to the volume fraction of the small-spheres and to the ratio of large to small-sphere diameter. An alternative approach to get to the same interaction potential expression is from the extended Gibbs adsorption equation which simply states that the Helmholtz free energy of a colloid/polymer mixture decreases by $\Pi \times \Delta V$ (ΔV being the overlap volume) as the spheres approach each other [16]. The upside of this approach is that the Gibbs adsorption equation provides a direct link between the depletion of the particles with depletion interaction potential and also offers approximate expressions for the interaction potential where an exact calculation is not worth considering.

Many researchers have tested the AO theory experimentally. Yodh *et al.* attempted to fit their data with the AO theory and showed that the fits were nearly perfect at low small-sphere volume fractions ($\Phi = 0.04$-0.07). At higher small-sphere

concentrations, a number of researchers have predicted that their liquid structure becomes important and other factors play a role [57, 65-68]. For example, it was shown that there is substantial depletion repulsion ($\Phi > 0.1$) or even an oscillatory component ($\Phi \geq 0.25$) to the interaction at separations of the order of one small-sphere diameter from contact [50]. Clear evidence for the presence of repulsive interactions at separations of the order of one small-sphere diameter has been presented by a number of authors both experimentally [50, 69, 70] and numerically [69]. Due to its entropic argument, the AO theory does not predict such repulsive interactions between large colloids, while the alternate osmotic pressure interpretation explains that the repulsive components of the interaction are due to high small-sphere concentrations for these orders of separations. Long-ranged oscillating depletion forces were experimentally confirmed in systems of charged macromolecules probably due to the contributions of pair-potential correlation effects among the macromolecules [71, 72]. Bechinger *et al*. reported repulsive depletion forces for binary "hard-sphere" mixtures with high R_L/R_S ratios even at low polymer concentrations [70]. These effects have been attributed to the existence of van der Waals forces between large and polymer molecules, thereby increasing their concentrations close to the large-sphere surface even at low polymer concentrations. Therefore, AO theory loses its merit in these special circumstances described above and is ideally applicable when the smaller species are relatively inert.

In our work, we will be using the AO model to model the interactions when the concentration of the (uncharged) polymer is considerably lower than the overlap concentration and for situations where van der Waals forces are not dominant. From the discussion above it is clear that AO model relies on a number of assumptions. Firstly, the

large colloids are modeled as hard spheres and the non-adsorbing polymer in the solution are assumed to be small-spheres of radius $R_S = R_g$ that are mutually interpenetrable, but cannot penetrate the large-spheres. The hard sphere potential is a good approximation for the colloid-colloid interaction for both sterically stabilized particles [73], and charged colloids dissolved in a solvent with a high ionic strength [74, 75]. The assumption that the polymers are interpenetrable is valid for polymers in *theta*-solvents and good solvents [76], or for ideal polymer chains that can be described by the ideal chain model, which states that two different monomers can occupy the same position in space without excluded volume effects [77]. Another important question to think about is "Is it realistic to model a deformable polymer coil as a sphere?" This was addressed by Meijer and Frenkel, who found that, if the radius of gyration of the polymers was less than 70 % of the radius of the large colloids, the AO model works quite well, provided that the polymer solution is dilute [78]. The mean size in these dilute systems is proportional to the radius of gyration (R_g) of the polymers. The depletion overlap thickness on the large-spheres and walls is thus proportional to the R_g of the polymer system. But there does exist a critical concentration, referred to as the overlap concentration, beyond which polymer entanglement effects start to play a role. Therefore, in order for the depletion attractions to be described by the AO model, the concentration of the polymer must be lower than the overlap concentration. Above the overlap concentration, the coils begin to overlap and the polymers form a mesh throughout the entire solution, with sharply increased viscosity; the AO model does not apply in this case. Joanny *et al.* (1979) have shown that the correlation length ζ plays an important role in such cases [79]. The correlation length is defined as the average spatial distance between the neighboring

31

entanglement points. For a non-adsorbing polymer in the overlap regime, depletion attractions still occur, but the thickness of the overlap regime is now proportional to the correlation length (ζ) instead of the radius of gyration (R_g) [79]. Figure 2.2 schematically shows the depletion overlap thickness for both these cases.

To summarize, the AO model treats ideal polymer chains in good approximation as interpenetrable hard spheres with a diameter $2R_g$. For the case of dilute polymer solutions, the ideal chain description is sufficient to predict depletion effects. In the case of small-sphere as depletants, AO model works well for their low concentrations, while unpredictable repulsive components arise at higher concentrations. For non-adsorbing polymers with excluded volume, the AO model predicts that the depletion overlap thickness depends on the size ratio R_L/R_g and the polymer concentration.

2.3.1 Other important Interactions

Aside from depletion interactions, two other forces that can affect the colloidal interactions are Van der Waals and electrostatic forces. Van der Waals forces are very
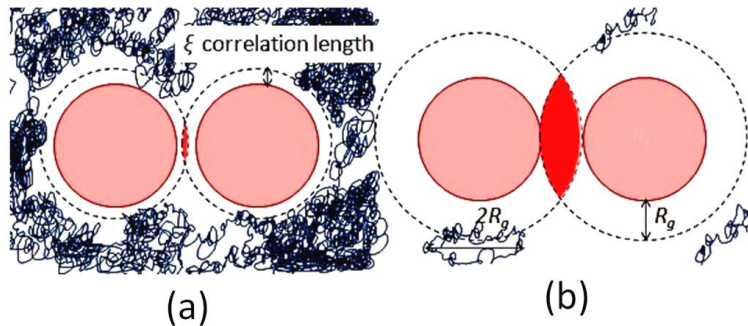
Figure 2.2 Overlap thicknesses in a) overlap concentration regime represented by correlation length, b) dilute regime represented by radius of gyration.

strong at short interparticle separations come into play when the charged colloidal particles overcome the Coulombic barrier from the electrostatic repulsions and strongly adhere to each other forming aggregates. In this work we are not interested in aggregation and therefore disregard modeling of Van der Waals forces. Modeling of electrostatic interactions between the particles was discussed in the Chapter 1. However, the electrostatic interactions between particles and wall surfaces are out of scope of this thesis. The expression for the repulsive electrostatic interaction energy between the charges spheres (Ω^{ss}) is given by:

$$\Omega^{ss} = 64\pi R_L\, k_B T n^\infty \kappa^{-2} tanh^2 \left(\frac{ze\psi_0}{4k_B T}\right) \exp(-\kappa x) \tag{2.4}$$

where n^∞ is the concentration of the electrolyte in the bulk of the solution, κ^{-1} is the Debye screening length, z is the valency of the electrolyte, ψ_0 is the surface potential and x is the distance of separation between the two surfaces, k_B is the Boltzmann constant and T is the temperature. From the equation it is evident that the repulsive interaction energy depends on the electrolyte concentration. This is because the presence of the electrolyte causing binding of the counterions to the surfaces of the charged spheres which in turn decreases the surface potential ψ_0. Obviously, the repulsive energy is low when the surface potential is low. The strength electrostatic repulsion potential influences the strength and the location of the attractive depletion potential well and thus dictates the separation between the colloids and the interacting surfaces which consequently affects the associated excluded overlap volume.

2.4 Selectivity of depletion attractions

The major scientific challenge for this project is to attain high selectivity of the depletion attractions to examine if preferential deposition of large-spheres is possible at specific places of interest on concerned geometries, while simultaneously preventing undesirable interactions or aggregation in the bulk. Can we fine-tune the interaction parameters with sufficient precision so that the colloidal particles exhibit desirable interactions with certain geometric features on 2D/3D substrates while preventing bulk aggregation and undesirable adhesion to the planar surfaces? Yodh and Dinsmore have shown that they can choose the concentrations of spheres and non-adsorbing polymer in such a way that bulk crystallization does not occur, while surface crystallization does [50]. Sacanna, Pine and co-workers used particle-particle interactions to attain an extremely high level of selectivity. They carefully tuned the interactions between specially designed dimpled particles (lock particles) and smaller spheres (key particles), so that the key colloids would only bind to the concave cavities of the lock colloids;
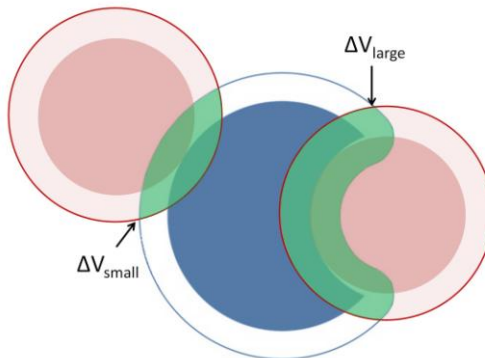
Figure 2.3 A diagram showing the lock-key colloid interactions. Small-sphere interactions are more likely to happen in the cavities due to higher volume overlap.

encounters with the convex exterior failed to result in stable attractions [51]. Figure 2.3 illustrates this visually: the overlap volume (green shaded region) for the key particle with the concave dimple is larger than the overlap volume with the convex exterior. The success of the lock-key interactions was defined on the basis of a single particle-particle interaction. Our interest lies more in self-assembly processes where this selectivity occurs on a much larger scale, involving large numbers of particles interacting with substrates with specific geometric features in a predictable way to form new colloidal structures. The main questions that must be addressed are "Can we precisely fine tune depletion interactions on a much large scale? Can they form the basis for controlled nanoscale self-assembly processes?"

In the past, researchers have worked on the formation of well-ordered structures using depletion interactions. Dinsmore *et al.* self-assembled colloidal particles on the step edges of the rough side of a silicon wafer, which is composed of truncated pyramids. They also showed the ability to entropically direct the colloidal particles to form ordered crystallites in corners prior to forming along the flat wall or in the bulk [50]. In conclusion, there is proof in the literature that selectivity of depletion attractions can be achieved, but very few studies provide a general analysis as to what kind of well-defined geometric structures are needed to maximize the selectivity of desirable over undesirable strucrues. Lin *et al.* showed that it is possible to devise arrays of structures into self-assemble particles in the grooves of a grating template [38]. To get a good quantitative understanding of the selective deposition of the particles onto the structured surfaces, we will perform modeling studies for controlled depletion-induced self-assembly of colloids on specific regions of structured surfaces.
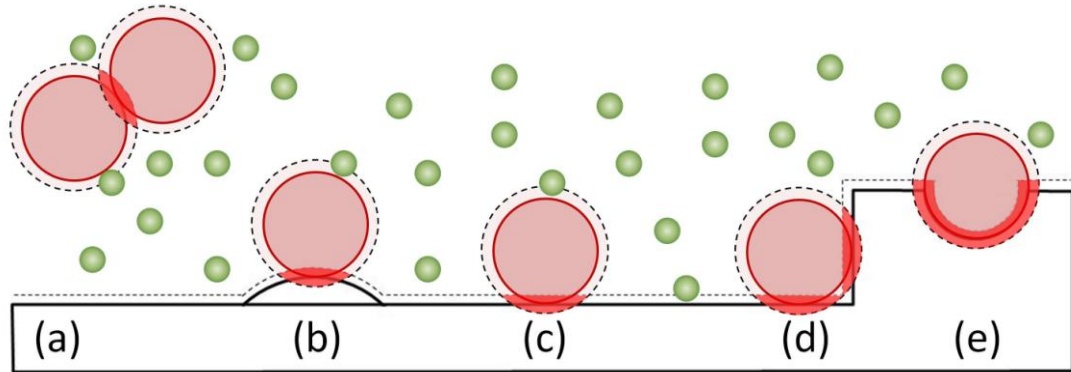
Figure 2.4 Schematic of the depletion attraction on various geometries of interest. The dashed lines represents the excluded volume (with the shaded part being the overlap) which directly correlates with the interaction strength. Figure (a) shows two large colloidal spheres. To the right we have interaction between a sphere and a solid wall for different wall geometries: (b) ridge, (c) planar wall, (d) edge, and (e) cavity.

For a suspension of colloidal particles dispersed in a fluid medium with wall constraints, there are several fundamental surface geometries that can be used to attract colloidal particles. The strength of these particle-particle or particle-wall interactions depends on the magnitude of overlap volume which in turn depends on the contact geometry between two objects. For five basic geometries depicted in Figure 2.4, the attraction increases monotonically from case A to case E due to progressively increasing excluded volume overlap. The dark shaded region in red represents the gain of small-sphere excluded volume (entropy). As one can see from the Figure 2.4, the overlap volume for a particle with an edge (c) is approximately twice as large as for the flat wall (b); both overlap volumes obviously depend on the size and size ratio of the depletant and large colloid. Based on Figure 2.4 we would expect the particle-edge attractions to be stronger than particle-wall attraction. Similarly, the entropic particle-wall force is roughly twice as large as the attraction between two particles in the bulk as we will also see from numerical calculations that are presented below. As discussed before, we use the two key

36

model parameters to fine-tune the interaction strength: (1) the size of the small-spheres (which defines the thickness of the depletion zone), and (2) the number density (volume fraction) of small-spheres, which determines the osmotic pressure. By combining this knowledge with the electrostatics, we intend to achieve the modeling and experimental investigations of these shape-selective interactions.

2.5 Numerical approach for calculating interaction potentials between colloids and complex geometrical surfaces

We developed a numerical code in MATLAB that can compute the shape-selective excluded volume overlap and hence the depletion interaction potential (for a given set of AO key model parameters) between colloidal particles and axially symmetric geometries of any arbitrary shapes, i.e. cylindrical objects with axially variable diameters. For our modeling studies, we used surfaces with increasing geometrical complexity in
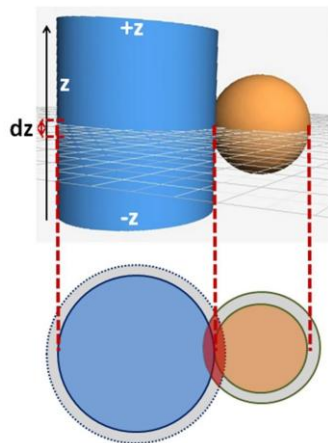
a) *Circle-Circle area of overlap*

$$A_{overlap} = A(R_1, d_1) \cap A(R_2, d_2)$$

b) *Excluded volume overlap*

$$V_{overlap} = \int_{+z}^{-z} A_{overlap} dz$$

Figure 2.5 Figure shows the cross section of cylinder-sphere intersection results in circle-circle overlap. To the right is the two step algorithm for calculating the total excluded volume overlap.

order to assess the feasibility of experiments. To determine the excluded volume overlap between the geometries, the most essential elements are the representative equations of the boundaries of the contact geometries. The numerical method used is versatile in approach and can also be used to determine the magnitude of depletion interactions between two axially symmetric colloids of arbitrary, non-spherical shape, as can be seen in the following sections. Using this numerical method in conjunction with the AO model, we are able to estimate the depletion interaction potentials between various concerned geometrical shapes for different dimensions. The most useful aspect of this approach is we are able to extract certain design criteria in order to optimize desirable specific shape-selective interactions between geometries of interest.

For geometries with spherical and cylindrical symmetries, the excluded area of overlap at any given axial position can be represented by the overlap area between two intersecting circles. A generic algorithm consisting of two major steps was deduced for computing the excluded volume overlap in such geometries: *a)* Computing the area of overlap of the cross-sectional circle-circle overlap and *b)* Determining the excluded volume overlap by integrating over the circle-circle area of overlap along the axis of symmetry with the appropriate integration limits. We first derived the generic numerical solution for computing the area of intersection of two circles of different radii as a function of the distance between their centers and the radii of the circles. The formula for the overlap area has been developed, validated and can also been seen under the section "Circle-Circle Intersection" on the Wolfram Mathworld web resource [80]. Finally, a numerical code was successfully implemented to develop these ideas in the algorithms in MATLAB environment.

The same numerical approach was used to calculate the interaction potentials for simple as well as complex contact geometries. We first computed the overlap volumes of the simplest of cases like sphere-sphere, sphere-wall, and sphere-edge at the point of contact which were represented in Figure 2.4, and steadily increased the geometrical complexity by investigating three dimensional geometric like uniform cylindrical surfaces, which can represent simple nanowires in the real world. We also computed the shape-selective interaction potentials for higher order complex geometries, such as between various diameter-modulated nanowires and spherical particles as we will see in the following sections. For the geometries that were represented in Figure 2.4, the computed interaction potentials are shown in Figure 2.6. They indicate that the attraction strength indeed increases monotonically from sphere-sphere, to sphere-cylinder, to sphere-wall, to sphere-edge due to progressively increasing excluded volume overlap (see the caption of Figure 2.6 for details). For the colloid diameters and polymer sizes chosen here, at a fixed polymer concentration, the attractive potential of particle-edge
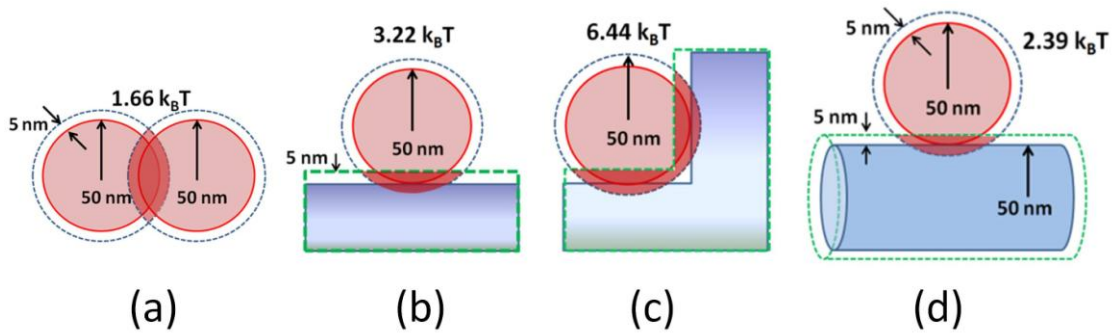
Figure 2.6 Schematic illustration of the depletion interaction ($R_s = 5$ nm, $R_L = 50$ nm at a small-sphere concentration of 0.38 wt %) between (a) two large colloidal spheres and between a sphere and a solid wall for different wall geometries: (b) flat wall, (c) edge and (d) cylinder. From left to right, the interaction strengths are 1.66 k_BT, 3.22 k_BT, 6.44 k_BT and 2.39 k_BT respectively.

interactions is found to be exactly twice as high much as particle-wall and roughly four times as high as particle-particle attraction. Similar numerical estimates were made by Yodh *et al.* during their efforts to selectively deposit particles on flat wall and edge surfaces [58]. In Chapter 3, we will show that this rank order is in agreement with experimental results (although it should be noted that we did not perform direct measurements of entropic potentials of mean force).

On higher order of 2D/3D complex geometries, the objective is to use colloidal self assembly to selectively deposit particles at very specific places on the geometry/template; the key challenge for the depletion interactions is to make these particle-surface interactions extremely selective. Selectivity in these systems is to be some extent designed by the shape of these geometries, for the reason that surfaces that interlock perfectly with the particles maximize their excluded volume overlap and thus particle deposition at these geometries is preferential over geometries that are deemed misfit with the particles and result in a smaller excluded volume overlap. Lin *et al*. showed that it is possible to choose a periodically patterned template and devise arrays of structures on the template to self-assemble colloidal particles in very specific positions on the template [38]. Sacanna, Pine and co-workers attained a high level of selective interactions using their specially designed lock particles and showed that small-spheres would fit nicely in their cavities; encounters with the convex exterior of the lock particles proved to be futile [51]. If we can demonstrate successful deposition of particles at our specific points of interest on the intended complex geometries, we are one step closer towards providing an important paradigm for the creation of three dimensional architectures on the nanoscale. In the following section, we will perform modeling

studies for interactions between spherical particles and diameter-modulated nanowires (step change diameter modulation and undulating nanowires with sinusoidal diameter modulation) followed by modeling studies involving non-spherical geometries for both interacting particles.

2.5.1 Spherical particles on undulating cylinders

For the case of undulating nanowires whose diameter varies sinusoidally, our aim is to engineer the interactions in such a way that particles will deposit reliably in the concave grooves of the undulating nanowires, while preventing other, undesirable interactions like bulk aggregation of particles and adhesion to the convex sections (ridges) of the nanowire. In particular, we aspire to use depletion-induced self-assembly to model high precision periodic deposition of the colloids along the sidewalls of these undulating nanowires. Our objective is to model the desirable shape-selective interactions
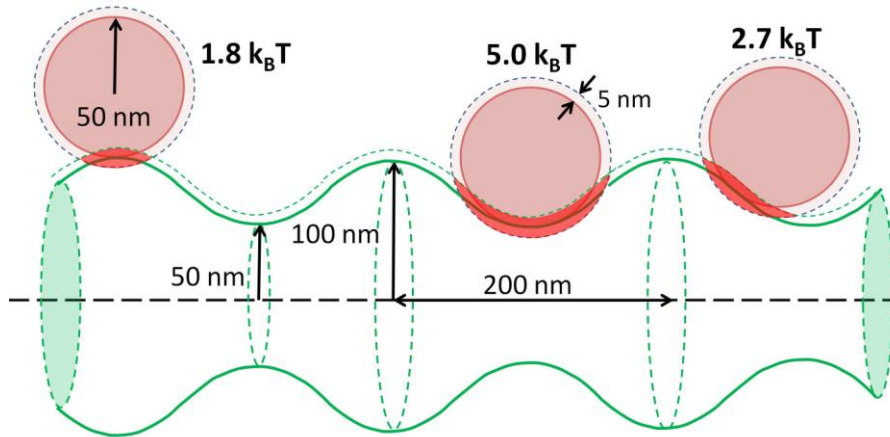
Figure 2.7 Schematic illustration of interaction between an undulating nanowire (radius varying between 50 and 100 nm, a 200 nm pitch) and a spherical colloid ($R_s =$ 5 nm, $R_L = 50$ nm at a small-sphere concentration of 0.38 wt %); from left to right, the interaction strengths are 1.8 k_BT, 5.0 k_BT and 2.7 k_BT respectively.

with magnitudes of 5 k_BT or larger, while undesirable interactions should be kept below 2 k_BT to be incapable of resulting in any substantial interactions. We based these magnitudes on the fact that the strength of depletion potential to induce successful interactions for the case of isotropic spheres was found to be more than 5 k_BT by direct measurements [81] and an interaction from an attraction potential as weak as 2 k_BT can be easily detached by thermal fluctuations resulting in the re-suspension of particles [82]. Taking these magnitudes into account, we have performed calculations for the depletion potential of spherical colloids at specific curvature positions on the sidewall of the undulating nanowire. The shape and dimensions of the colloids and nanowire are shown in Figure 2.7 (refer to the figure caption for details). Polyethyleneglycol (PEG, MW = 11,500 Da; $R_s = R_g = 5$ nm) [83] was presumed to be the hypothetical non adsorbing depleting polymer inducing the depletion attractions for all the interactions considered in this chapter. PEG was chosen because it has been used successfully by several experimental researchersto to generate depletion interactions [70, 81]. The radius of gyration of PEG in aqueous solutions as a function of molecular weight is given by a power law fit [83]. The spherical colloids that were used in Chapter 3 for the depletion interactions were made out of PS, although they can be made of any material as long as there are no specific interactions with PEG. In a hypothetical aqueous solution (on a template with undulating nanowire growth) consisting of a binary mixture of the depletant and spherical colloids, the particles approach the nanowire through diffusion; it is required for us to model the shape-selective interactions such that the particles encountering the grooves of the nanowire anchors and binds, while the particles encountering the ridges fail to bind. The key model parameters (R_L/R_g, R_g and Φ) were
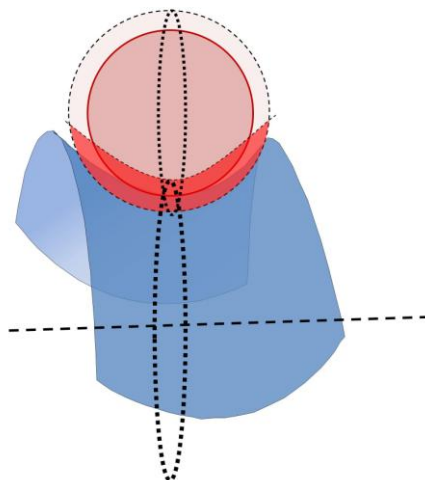
Figure 2.8 3D representation of sphere-saddle geometry for sphere interacting with groove of the undulating nanowire.

adjusted such that the particle-groove interaction had an interactions strength is 5.0 k_BT (middle). Under those conditions, the particle-ridge interaction (left) was found to be 1.8 k_BT, which should be incapable of causing permanent particle deposition. The intermediate case shown in the figure (right) is chosen such that the point of contact is midway between a groove and a ridge and yields interaction strength of 2.7 k_BT. It is anticipated that the particles interacting with this intermediate surface on the cylinder will therefore most likely drift toward a more desirable location with a higher depletion potential (groove), as long as the initial binding is not permanent. These interaction strengths were achieved *in silico* for a PEG concentration of 0.38 wt%, which is well below the overlap concentration of 5 wt% [84]. The numerical modeling to find the excluded overlap volume for these three contact scenarios shown in Figure 2.7 were done on an individual basis by breaking down the undulating cylinder geometry into separate geometries and computing each of these interaction potentials on a case-to-case basis. For example, the particle-groove overlap volume was computed by projecting the groove as saddle geometry as seen in Figure 2.8. The problem again reduces to finding the overlap

area for the cross-sectional circle-circle overlap at every axial position and integrating this area along the saddle/parabolic curve with appropriate integration limits. The key parameters of interest for solving this problem are the dimensions of the wire (minimum and maximum diameter), sphere, depletion layer thickness and the equation that parameterizes the shape of the wire. These calculations are non-trivial because the dimensions of the circular cross-section of the wire change accordingly as a function of axial position. Once computed, one can use these calculations to design the exact dimensions of ridges, grooves, depletion layer thickness and the wavelength of the undulations to maximize the likelihood of particle-groove depositions. For example, by plotting the ratio of excluded volume overlaps for sphere-saddle and sphere-anti-saddle geometries as a function of depletion overlap thickness ($R_s = R_g$), we were able to extract the design rules for optimized interactions; to make the sphere-saddle depositions more favorable over sphere-anti-saddle, one has to minimize the size of the smaller species at any given small colloid concentration. In summary, the numerical model was useful to determine the design criteria of the geometries as well as to roughly evaluate the size and concentration of the smaller species, to make these shape-selective particle-groove interactions.

2.5.2 Spherical particles on diameter modulated cylinders

We also performed modeling studies on nanowire with step-changes in diameter, aside from the sinusoidal variations discussed above. It should be mentioned that the selection of these diameter-modulated nanowires for our modeling studies is not completely random. Researchers have successfully demonstrated fabrication of diameter-modulated nanowires via vapor-liqiud-solid (VLS) technique governed by adsorption and

desorption on the sidewall of the nanowire [85]. As shown in the figure 2.9, the step change in radius (Δr) of the cylinder results in an axially symmetric step edge. Depletion induced modeling studies were done for the particles to deposit specifically and preferentially at these step edge structures. We computed the interaction strength as a function of the magnitude in diameter change Δr (see Figure 2.8); the model parameters (R_L/R_g, R_g and Φ) are same as the ones used in the previous section for sinusoidally modulated nanowires. The magnitudes of interaction strengths obtained were found to be always greater than the sphere-cylinder contact (refer to Figure 2.6 (d)) for any $\Delta r > 0$ as a result of the gain in excluded volume overlap between the spherical particle and the step edge structure. Therefore, the interaction strength was always greater than the sphere-cylinder value of 2.39 $k_B T$ except for the case of $\Delta r = 0$ where sphere-cylinder
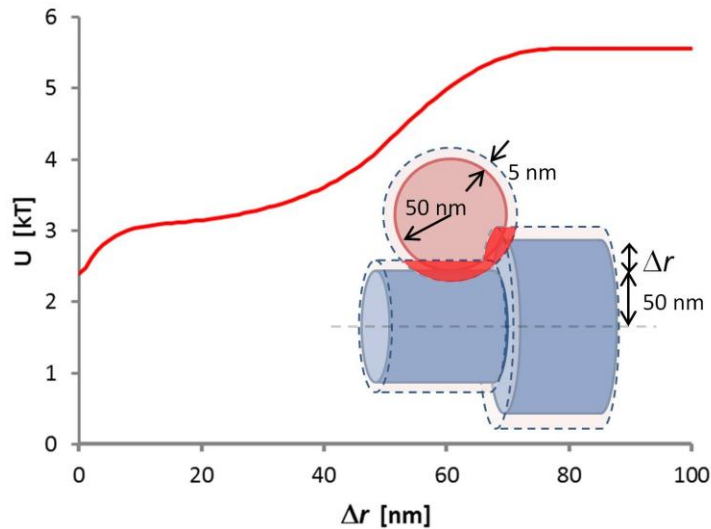
Figure 2.9 Interaction strength between a spherical colloid (radius 50 nm) and a cylindrical nanowire (nominal radius 50 nm) with a step change in radius, as a function of radial step size Δr, in an aqueous PEG solution (MW = 11,500; R_g = 5 nm) at concentration of 0.38 wt.%.

geometry is reinstated. It was expected for sphere-modulated-nanowire contact, as Δr increases, the excluded volume overlap and henceforth the interaction potential was to increase steadily (if not linearly). However, as we plotted the magnitude of this interaction strength for various Δr values, a slight plateau was observed for the range of Δr values between 10 nm and 40nm, which was unforeseen. Moreover, as Δr increases, the edge structure starts to become more pronounced, increasing the excluded overlap volume for the contact geometry. When Δr reaches a certain critical value (75 nm), maximum possible overlap between the geometries occur and any further increase in the Δr does not result in additional overlap volume. Although we were able to mathematically explain the existence of the predicted plateau after a detailed numerical, it was learned that the geometrical complexity involved in these interactions can result in unforeseen overlap volume calculations and non-intuitive variation of interaction strength with geometrical parameters.

2.5.3 Cylinder-cylinder and dumbbell-dumbbell interactions

Finally, we expanded our numerical modeling for calculating shape-selective interactions between two non-spherical cylindrically symmetrical geometries. The specific case of interest is a suspension of well-defined cylindrical and dumbbell shaped particles. Figure 2.10 presents schematic illustrations of parallel interactions between such cylindrical and dumbbell shaped structures. The shape and dimensions of these three dimensional structures are depicted in the schematic. While the end-to-end interactions between these geometries would result in identical overlap volumes, the side-to-side interactions are very much distinguishable due to their different shapes. In the interest of this scenario, the end-to-end interactions are disregarded and we focus attention on the

46

side-to-side interactions of these geometries. A hypothetical question that can be asked here is "If one can somehow fabricate these particles, how should they design the geometric dimensions to make a certain depletion induced assembly very selective?" We used our numerical model for computing the excluded overlap volumes for these side-to-side contact geometries for various overlap lengths and depletant sizes. Dumbbell-cylinder interactions are disregarded due to the smaller overlap volumes of this contact geometry as a result of asymmetry. Compared to the cylinder-cylinder overlap volume calculation, the dumbbell-dumbbell overlap volume calculation is an arduous task due to the additional overlap volume that results from the interlocking of the end-cap of one dumbbell with the indenture in the other dumbbell (see Figure 2.10) giving rise to surplus excluded overlap volume along the overlap length.

We computed the ratio of the overlap volumes of dumbbell-dumbbell (*V(db)*) geometry to cylinder-cylinder geometry (*V(cyl)*) as a function of overlap length (x) for a
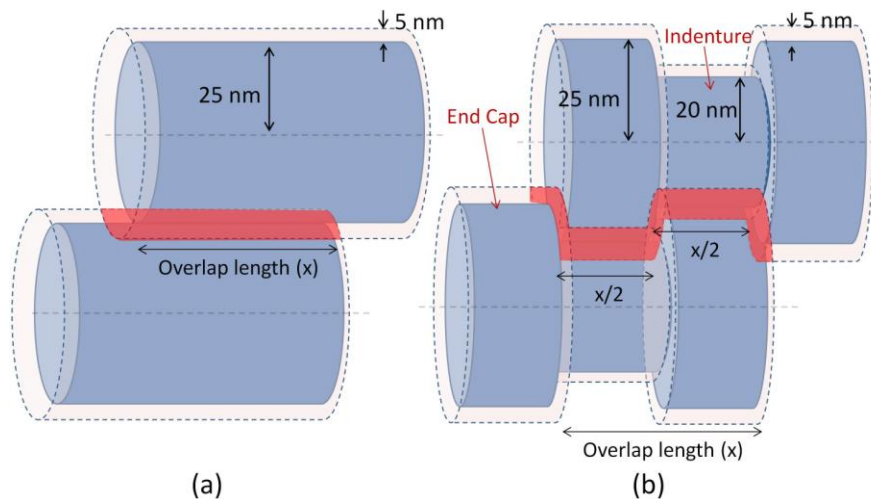
Figure 2.10 Schematic of side-to-side intersection of (a) cylinder-cylinder and (b) dumbbell-dumbbell geometries. The shaded regions in red represent the excluded volume overlap.
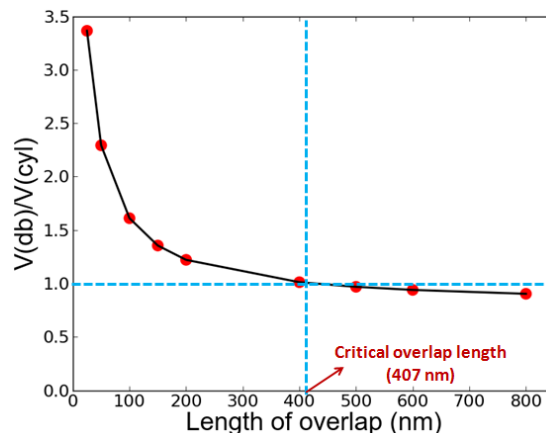
Figure 2.11 The plot showing ratio of the overlap volumes of dumbbell-dumbbell to cylinder-cylinder geometry as a function of overlap length for a depletant size of 5nm. Critical overlap length is denoted on the X axis where the ratio falls below 1.

depletant size of 5 nm. The purpose of this study was to determine the optimal overlap length and depletant size that would strongly favor dumbbell-dumbbell interactions over cylinder-cylinder interactions. The numerical analysis showed that the endcap-indenture overlap contribution was large for small overlap lengths and small for large overlap lengths. Therefore, the ratio *V(db)/V(cyl)* peaked for small values of overlap lengths and decreased gradually as the overlap length increased. As a matter of fact, above a critical overlap length (407 nm) the overlap volume for the cylinder-cylinder geometry was found to exceed the overlap volume of dumbbell-dumbbell geometry at which the ratio *V(db)/V(cyl)* falls below one as seen in the Figure 2.11. This is because the cross-section of cylinder-cylinder overlap consists of identical circles of diameter 25 nm while the cross-section of dumbbell-dumbbell overlap consists of circles of diameter 25 nm and 20 nm which results in a smaller area of overlap. As the overlap length increases above the critical overlap length, this surplus contribution in the cylinder-cylinder overlap caused due to the larger crossectional overlap exceeds the contribution from the endcap-indent overlap volume. Therefore for an overlap length < 407 nm, dumbbell-dumbbell

48
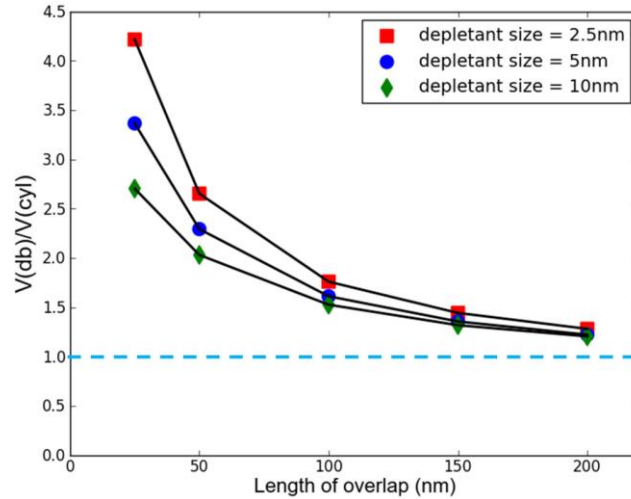
Figure 2.12 The plot shows ratio of the overlap volumes of dumbbell-dumbbell geometry to cylinder-cylinder geometry as a function of overlap length for three different depletant sizes.

interaction is favorable and for overlap length > 407 nm, cylinder-cylinder interaction is dominant.

Furthermore, we investigated the effect of size of the depletant on these non-spherical interactions. We reproduced the plot for two other depletant sizes (2.5 nm, 10nm) keeping rest of the geometric dimensions unaltered (Figure 2.12). Using a smaller depletant size (2.5 nm), we found that the ratio of the overlap volumes of dumbbell-dumbbell geometry to cylinder-cylinder geometry increased for all the overlap lengths considered. On the other hand, increasing the depletant size produced the contrary effect. However, as one can see from figure 2.11, it was observed that these curves converged with the increase in overlap length due to the decreasing contribution from the endcap-indent overlap. Therefore, using this information, the design rules and model parameters which favor the dumbbell-dumbbell interactions over the cylinder-cylinder interactions can be identified. A smaller depletant size and a small length of overlap (below the

49

critical length) favors the dumbbell-dumbbell interactions while the higher values for the same would favor the cylinder-cylinder overlap.

In addition, there is another dimension to specificity. The discussion above distinguishes interactions based on two different geometries interacting with each other: a cylinder-cylinder interaction being weaker than a dumbbell-dumbbell interaction. However, when we have a mixture of dumbbell geometries alone, there are multiple orientations that are possible between two dumbbell geometries. Two dumbbells can either fit in a parallel overlap configuration (as shown in Figure 2.10 (b)) or a crisscross overlap configuration where the axis of the dumbbells are perpendicular to each other. In order to favor the parallel orientation over the crisscross orientation (or vice-versa), we again have to change the design rules of the geometries under fixed conditions (constant polymer concentration) or we need to choose optimum conditions where parallel overlap configurations are more favorable or carry out both these plan of actions simultaneously. Therefore, it is recommended that our design rules should also be such that there is a controllable preferential orientation either by changing the geometry dimensions or by changing the experimental conditions (depletant concentration, size etc). In conclusion, using our versatile numerical model calculations, we were successfully able to extract the optimum conditions needed for a dumbbell-dumbbell interaction over cylinder-cylinder interaction. Calculations such as these performed above can be very helpful for fine-tuning the model and design parameters in order to make these pair wise depletion induced interactions highly preferential. However, future work should be focused on controlling the preferential orientation for dumbbell-dumbbell geometry.

2.6 Conclusion

In this chapter, the basic concept and simple theoretical models along with their assumptions and limitations for depletion interactions were presented. In specific, the original Asakura Osawa model was considered to explain the origin of depletion forces. Throughout the chapter, emphasis was laid on achieving highly selective interactions between particles and geometries of interest by preventing undesirable interactions which is the primary motivation of this work. Numerical models were built based on a simple two-step algorithm using MATLAB tools, to compute the magnitude of excluded volume overlaps (and depletion interactions) for particle-particle, particle-wall interactions for different wall geometries, whose values were shown to be consistent with other researchers. The same numerical approach was used to compute interactions potentials between various kinds of three dimensional spherically and cylindrically symmetrical geometries in the increasing order of complexity. In particular, modeling studies for interactions between spherical particles and diameter modulated nanowires (sinusoidal and step-change) were successfully performed. For the case of sinusoidal nanowires, it was shown that the key model parameters and the geometrical dimensions of the nanowires can be adapted to increase the selectivity of particle-groove interactions as opposed to particle-ridge interactions. Whereas for the case of step-change modulated nanowires, the interaction strength calculations as a function of the characteristic dimension led to unforeseen numerical calculations, cautioning us such geometrical complexities can result in unpredictable outcomes. Furthermore, in the last section of this thesis, this numerical methodology was successfully shown to be applicable to non-spherical cylindrically symmetrical systems where dumbbell-dumbbell and cylinder-

cylinder interactions were studied as a function of their overlap length. Using the numerical models, favorable conditions for both these interactions was explored while reaching at an overlap length where both these interactions were indistinguishable based on their depletion potential. It was shown that a smaller depletant size and a small length of overlap favors the dumbbell-dumbbell interactions while higher values favored cylinder-cylinder overlap. Future work should focus on controlling the preferential orientation of dumbbell-dumbbell interactions which should be feasible using the same numerical model.

The numerical approach presented in this chapter provides us with a versatile way of calculating the magnitudes of interaction strengths for different geometrical shapes and dimensions. We were able to draw out some design rules in order to optimize or prioritize a certain desirable interactions while undermining the undesirable interactions at the same time. Using this numerical methodology, it was concluded that selectivity can be achieved via fine-tuning the interactions using model parameters and by implementing some design criteria for the concerned geometries. In conclusion, it can be said that these numerical models in conjunction with theoretical depletion models are very much capable to assess the feasibility of our future depletion experiments and can also be used to guide the design of the nanoscale three-dimensional structures for highly preferential deposition in the event of their fabrication.

Also, since the depletion interactions are physical in nature, their generality allows us to apply the same principles and calculations to a wide range of physical dimensions. For example, our proposed modeling studies on the deposition on nanowires can be easily applicable to nanowires with diameters between 10 nm and 10 μm by

changing the dimensions of the depleting agent. Therefore, these shape-specific particle deposition experiments can first be performed on microscale structures where visualization is relatively easier using standard optical microscopy methods and it can then be scaled down to nanoscale platforms. The major advantages of using depletion interactions as a self-assembly technique is its unique combination of ultimate scalability, process generality with regarding to the materials and its low investment compared to other techniques. If one can precisely control these shape-selective interactions and make them fairly reproducible, they provide exciting opportunities for scalable fabrication on the nanoscale.

CHAPTER 3

Experimental studies of depletion interactions of colloids in confined systems and on structured surfaces

3.1 Introduction

In this chapter we present experimental findings of depletion interactions which were guided by our modeling studies from the previous chapter. We investigate the influence of polymer (PEG) concentration (C_p) and electrolyte (salt) concentration (C_s) on the self assembly of one of the most commonly used colloidal systems, polystyrene (PS) hard-sphere colloids in confined volumes and on structured surfaces. In what follows, we manipulate two parameters of our model system to control the interaction potentials of colloidal systems in great detail. Using an appropriate polymer system, we will have the ability to precisely fine-tune the strength and the range of the attractive potential that drives the self assembly of the colloids. We manipulate the strength of the depletion interactions using the C_p (expressed in weight % or volume fraction Φ). The second parameter is the ionic strength which can be controlled using a monovalent electrolyte. By changing the C_s (and hence the inverse screening length κ^{-1}), one can experimentally tune the range of the electrostatic repulsion and thus modify the potential barrier. Researchers in the past have been able to fine-tune the interactions in order to induce very specific shape-selective interactions between the geometries of interest. However, previous authors have not studied in detail, the effect of electrostatic interactions in the depletion induced self assembly [37, 38, 51]. Badaire *et al.* lithographically designed their own cylindrical colloidal particles and tailored the

depletion and electrostatic interactions between the particles to self-assemble them into highly anisotropic structures [39]. We intend to manipulate the interactions to obtain many and different kind of interactions between particles themselves and with the neighboring geometries.

Hard-sphere colloids are the simplest systems and can easily provide a beginning point to study colloidal dynamics and the interactions such as the attractive depletion forces and electrostatic repulsions which can result in non-trivial phases. This is because hard-spheres systems are non-interacting at all separations beyond their radius and infinitely repulsive on contact (cannot overlap with each other) [86]. However, true hard-sphere systems do not exist in reality. The PS colloids used in our experiments are charge stabilized and provide us with merely approximate substitutes for hard-sphere systems. Often times, hard-spheres are imperfect as model systems for atoms because, practically speaking, materials have attractions and bonds that help hold the atoms together, as well as repulsive interactions between their nuclei that stabilize them [87]. Thus, it can be more beneficial to study colloids with more or less interactions (attractive and repulsive) than the idealized hard-sphere systems. By definition, hard-sphere colloids lack attractive and long-range interactions, which typically compete with entropic effects to produce ordered phases [58]. It was Asakura & Osawa (1958) who first noted that in mixtures of binary spherical colloidal particles, an ordered configuration of large colloidal spheres as a result of increased entropy of the smaller colloidal spheres can increase the total entropy of the system. This is because the entropy of the small particles prevails over the large particles because of their higher population compared to the large colloids.

In our investigation of self assembly of charged PS colloids, we observed various kinds of interactions between the PS colloids themselves and with the geometries surrounding them by changing C_p and C_s in the suspension. These rich varieties of interactions that were observed are neatly presented using a phase diagram for various C_p and C_s that were explored. This work is unique in a way as we explore the effect of electrostatic interactions on the self assembly process and provide a bigger picture of how these interactions operate under different conditions. The main emphasis was laid on understanding and controlling the depletion interactions between colloidal particles and geometries of interest. The strength of the depletion interactions can be modified using the C_p, while the range of the interactions can be simultaneously modulated using the size (R_g) of the polymer system. The larger the R_g, the larger is the excluded volume for the bigger colloids and the interactions become long ranged. But this also increases the volume fraction of the polymer, so we will have to decrease the number density of the polymer molecules. Therefore, to increase the strength of the depletion interaction one has to face a tradeoff between the number density and size of the polymer system. So, it is important to carefully pick out these parameters simultaneously to cause selective depositions on flat and structured surfaces. The same methodology was used to study surface crystals and rate of crystal growth on a flat glass substrate. Our investigation of self assembly of colloidal spheres on silica surfaces with edges can offer a new approach for directed self-assembly of novel nano and microscopic structures.

3.2 Materials and experimental setup

We carried out systematic experiments using binary colloidal suspensions of PS spheres and non adsorbing depleting polymer Polyethylene glycol (PEG) in aqueous

solutions. PS/PEG colloid-polymer systems have been used as they were successfully studied in the past for depletion interactions [69, 81]. PS spheres (fluorescently labeled) were used as they were the most common commercially available model colloidal systems and are accurately spherical and usually monodisperse. Also, the density of the PS spheres is 1.05 g/cc which make it easier to match their density with heavy water and DI water combination. The density matching is an important criterion for the depletion interaction studies and the investigations related to growth of surface crystals because it keeps the majority of the PS population in the bulk of the sample negating sedimentation. A disadvantage is that the high refractive index of PS (1.59) makes it extremely difficult to observe bulk structure of suspensions at high number density. The PS particles are hydrophobic and thus always tend to agglomerate, so we use particles with a surface charge modification to prevent them from aggregating in aqueous solutions. The surface charge of the particles had an estimated value of 0.3231 C/m^2. These particles are usually functionalized with hydrophilic groups, carboxylate group (-COOH) in our case. These end groups ionize completely in polar solvents releasing counterions (H$^+$) thus making the particles charged (negatively) and stabilized. These counterions stick around the particles forming a "Debye double layer" around the particles leading to double-layer repulsions that decay exponentially. These repulsions between the charged particles can be screened by the solution's ionic strength which is again controlled using a monovalent salt concentration (NaCl) in our case. Screening length (inverse Debye length $1/\kappa$) for a monovalent electrolyte at room temperature (25 °C) can be easily calculated using the simplified relationship

$$\frac{1}{\kappa}(\text{nm}) = \frac{0.304}{\sqrt{I(\text{M})}} \tag{3.1}$$

where I is the ionic strength expressed in molar (mol/L). The polymer used to induce depletion attractions (PEG) is non-ionic, water-soluble and does not adsorb on the PS particles. It is well known that below its critical concentration, PEG forms coiled chains in water with a characteristic R_g. We used three different molecular weights (MW_1 = 1000,000 Da, $R_g \approx$ 60 nm; MW_2 = 600,000 Da, $R_g \approx$ 50 nm; MW_3 = 20,000 Da, $R_g \approx$ 7 nm) for PEG to investigate the depletion interactions between the PS colloids. While both MW_1 and MW_2 as depleting polymers resulted in desirable depletion attractions between the PS colloids, MW_3 was not the ideal depletion polymer probably due to small range of interactions achieved using it. We used two different sizes for charged PS colloids (0.5 μm, 1 μm). The size of the PS particles was chosen in the micrometer range so that they are easily visible under the optical microscope. While the 1 μm PS colloids showed good signs of spontaneous nucleation, it was hard to see desirable interactions using the 0.5 μm particles. This was probably due to the high surface charge of the 0.5 μm PS colloids which had an estimated value of 2.5248 C/m^2 compared to the 1 μm PS colloids with a surface charge of 0.3231 C/m^2. For the various C_s that were used throughout our experiments, the highest value of the screening length that was obtained was 3nm. Since this length span is very small compared to the PS particle diameter used, we can approximate the bare interactions between the PS particles as hard-sphere-like. However, the repulsive interactions cause these PS colloids to behave as hard spheres with an effective radius that is larger than their actual values. The radius of gyration for PEG as a function of molecular weight in aqueous solutions is given by a power law fit [83]. For

the molecular weight which was used in our experiments (10^6 Da), the R_g has been determined using static light scattering to be 67.7 nm [83] which is nearly the same as the value obtained using the power law fit.

We captured the behavior of the PS particles in real time using fluorescence optical microscopy. Stock solutions of polymer and electrolyte were made prior the sample preparation. After mixing the desired amount of electrolyte and polymer (wt %) solutions with the PS particle suspension, the mixtures were mixed using a vortex mixer and gently sonicated for ~ 20 minutes to prevent particle aggregation. The samples were then loaded into ~100 μm thick sample chambers, which were created by placing parafilm spacers between a microscope slide (or structured silica surface) and cover slip, and sealed with vacuum grease to prevent evaporation. Each time, we injected approximately 10 μL of suspension into the sample chamber. The behavior of fluorescent PS particles in the samples was monitored at via an optical microscope (Leica DM-IRB) with a 63× objective, and images/movies were captured using a CCD camera (Cohu 4920, Poway, CA; 30 frame/s and 640 × 480 pixel resolution).

3.3 Selective depletion interactions on flat substrates and in bulk

For all our experiments, we used our existing mathematical models for predicting depletion interactions and electrostatic repulsions between the charged PS particles to guide us with the polymer and electrolyte concentrations. Also the values for C_s were chosen such that the Debye screening length is always smaller than the R_g of PEG at all times (the particles have to get close enough for the excluded volumes to overlap). However the electrostatic interactions between the particles and wall geometries is not a

simple picture and cannot be predicted due to our modest knowledge on the surface charge of the silica/glass substrates immersed in electrolytic solutions and also numerical modeling of electrostatic interaction between particles and various wall structures is out of scope of this thesis. Therefore our numerical modeling for particles and wall geometries can only predict depletion interaction energy but not the total interaction binding energy which is the combination of repulsive electrostatic interaction energy and attractive depletion interaction energy. We use a methodology where we complement the statistical information obtained for depletion attractions from the mathematical models with our experimental findings to get a thorough understanding of the phenomenon.

In Chapter 2 we discussed the depletion interaction between colloidal spheres and various wall geometries. We used a systematic approach where we first obtain the C_s and C_p for the strongest possible interaction and backed off the concentrations to arrive at the desired kind of interactions. Therefore, our first undertaking was to find the favorable
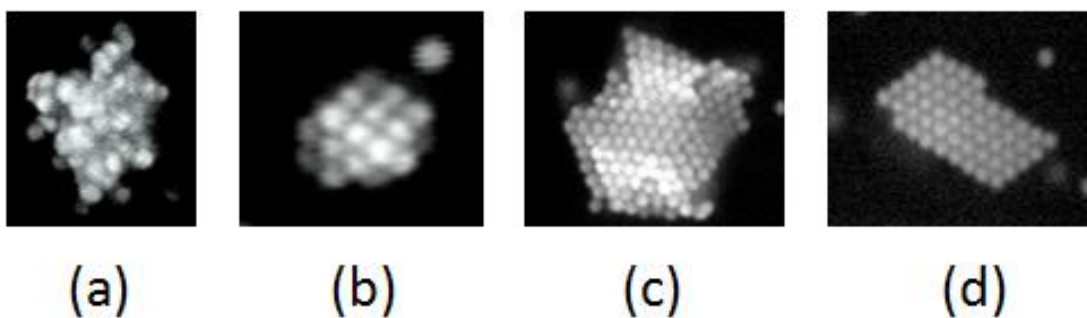
Figure 3.1 Microscopic images of 1 μm diameter particles suspensions in the decreasing order of interaction potential. Figure (a) shows aggregation (0.1 wt % PS, 0.082 wt% PEG, 0.05 M NaCl) (b) shows bulk nucleation (0.1 wt % PS, 0.045 wt% PEG, 0.01 M NaCl) (c) shows surface nucleation growing into the bulk ((0.1 wt % PS, 0.09 wt% PEG, 0.0325M NaCl) and (d) shows surface nucleation (0.1 wt % PS, 0.025 wt% PEG, 0.0325M NaCl).

values for C_s and C_p for which the particles would start to aggregate and permanently adhere in the bulk. Once we determined these conditions, we were able to lower the values of C_s and C_p to first obtain the conditions for nucleation on a flat surface and then nucleation exclusively in bulk. According to our theoretical models, crystals should nucleate in edges before they nucleate on a flat surface or in the bulk as a result of the entropic force on a particle near the wall being roughly twice as large as that between two large particles in the bulk and the entropic force at an edge being roughly twice as large as the entropic force on the particle near a wall. But our first sets of experiments are carried on flat microscope glass substrates and silica substrates which lack sharp edges. Note that there is an innate electrostatic repulsion between the negatively charged carboxylate-modified microspheres and the flat glass (or silica) substrate which are known to acquire negative surface charge density through dissociation of terminal silanol groups [88]. For the case of surface nucleation, this natural repulsion has to be overcome by the depletion attraction much like bulk nucleation where the attractive potential should overcome the repulsion between the particles. In Figure 3.1, we use a series of microscopic images to show the usual trend of these interactions in the bulk and on the wall.

Figure 3.1 (a) shows the aggregation of PS particles caused due to strong depletion attractions in the bulk of the sample. These aggregates can be easily identified as they are highly unstructured and lack long range order. As we arrive at a certain kind of particle-geometry interaction, the interactions in the proximity of these electrolyte & polymer concentrations were probed and the behavior of the particles was duly noted for these concentrations. For slightly lower concentrations, the particle-particle interactions

were still strong but only resulted in smaller unstructured aggregates. The size of the aggregate increased with increase in depletion strength and vice versa. As C_s or C_p (or both) were decreased, we observed a very dense 3D honeycomb like hexagonally packed crystalline structures forming in the bulk of the suspension (see Figure 3.1 (b)). In this case, the interaction strength is such that particles can rearrange to find their sweet spots in order to obtain lowest possible energy state. Aggregates and 3D crystals can easily be distinguished by quantifying the level of ordering using a local order parameter [89]. Details of this quantification method to characterize the order of packing will not be discussed here. For concentrations intermediate between aggregation and honeycomb-like formation, we observed sparsely dense clusters without orientational ordering formed due to strong particle-particle interaction. For these interaction strengths, the particles lack the freedom of rearrangement as they are bound too strongly and are unable to move. Upon further decreasing the concentrations, the bulk crystals appeared to form exclusively (selectively) and spontaneously as they were observed readily after inserting the sample into the chamber.

As we further decreased the concentrations, the activity in the bulk decreased steadily and crystalline structures with hexagonal symmetry were seen to grow along the surface of the wall as seen in the Figure 3.1 (d). The depletion interaction of individual PS colloidal spheres with the wall surfaces alone may not be sufficient to establish a stable interaction. Therefore particle-wall interactions are often associated with additional particle-particle interactions on the side to create a more stable nucleus. However, the particle-wall interaction is stronger than the particle-particle interaction and therefore you don't see crystals growing in/into the bulk. And for this reason, we claim these
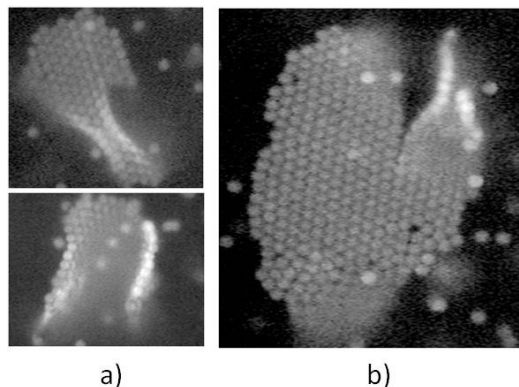
Figure 3.2 Crystal anomalies found in surface crystals due to gravity effect (0.1 wt % PS, 0.035 wt% PEG, 0.025M NaCl): a) crystal-twisting and b) crystal-tearing.

interactions to be selective even though particle-particle interactions play a role in forming the surface nucleus. The size of the nucleus can further grow as a function of time as we will see in the following sections. The crystalline structures appeared on both top (microscope slide) and bottom (coverglass) confining surfaces although the percentage of crystals on the bottom surface was higher due to gravity bias. When silica substrate was used as the top confining surface, the samples were placed on a slow roller to remove bias due to gravity which can favor interactions on the bottom (glass) surface to a greater extent.

While most of the surface crystals were found to be adhered to the wall and are immobile, some large crystals formed at slightly lower depletion potentials appeared to hold very loosely to the wall and a few others even diffused laterally close to the wall surface. These is a result of a wall crystal forming along the wall and the particle-wall interactions not being strong enough and are opposed by the buoyancy and Brownian forces. When large surface crystal structures formed on the top surface, we also saw anomalies in the surface crystal formation like crystal-twisting, crystal-tearing (see

Figure 3.2) due to gravity forces pulling it to the bottom undermining the depletion attractions with the flat wall. This indicates that the assemblies can be reversibly formed in the sense that the structures are not deposited in deep kinetic traps, as in van der Waals interactions.

For intermediate concentrations between the regions of exclusive bulk and surface nucleation, we observed two kinds of behaviors. Firstly, we saw a second layer of crystalline structures (see Figure 3.1 (c)) appearing on the surface crystals as a result of particle-particle interactions being strong enough. And then there is an intermediate concentration regime where both surface and bulk nucleations compete and the particles can form either surface nucleates or bulk nucleates simultaneously depending on where they first collide. Therefore, both particle-particle and particle-surface interactions were observed in the same sample. The bright spots as seen in the Figure 3.1 (c) are due to the formation of a second layer over the first layer of surface crystal. Nucleation experiments were carried out on glass and silica substrates; identical behavior in terms of quality and quantity of surface crystals was observed on both these surfaces for the same concentrations used. Since depletion interactions are material independent and both these surfaces (silica and silicate glass) acquire a negative charge due to dissociation of surface silanol groups, the behavior was expected to be the same on both these substrates. It should also be noted that the experiments were repeated for reproducibility concerns and the results are found to be fairly reproducible. Therefore, from these observations it can be concluded that we can reach at a certain C_s, C_p where each of these interactions are to be mutually exclusive. However, it should be noted for the case of bulk nucleation and aggregation, individual PS particles and aggregates were sometimes seen to bind to the

confining surfaces of the sample chamber. This is probably due to the higher C_s values pushing the particles and sedimentary aggregates closer to surfaces due to decreased repulsive barrier.

If we increase C_p past the proximity of the aggregation region, we again found a region (not included in the phase plot) where the particles are non-interacting with themselves and the surfaces around them. There are two theories that might explain this particular observation. The first theory being, the depleting polymer (PEG; $MW = 1000,000$ Da) reaches its overlap concentration. Water is a good solvent for PEG which has a Flory Huggins interaction parameter between 0.4-0.5 depending on the solution conditions [84]. For good solvents, the threshold concentration for molecular overlap (C^*) depends on the molar mass of the polymer and is related by $C^* \propto MW^{-4/5}$ [84]. Based on this knowledge from the literature we estimated a value for the overlap concentration and it was 0.138 wt %. Surprisingly, it was found that depletion induced attractions vanish at this proximity of the polymer concentration. Above the overlap concentration, the excluded volume overlap radius is decreased because the radius of gyration is no longer the criterion that defines the radius of the polymer. The polymer forms a mesh structure and the correlation length starts to act as the thickness of the excluded volume overlap. So the range of interactions is cut down by a huge factor and the depletion attractions essentially disappear.

A second hypothesis is entropic repulsion. The entropic argument does not capture repulsion. For example, Dinsmore *et al*. have shown that the aggregation kinetics of the large spheres is slowed down considerably as the small spheres are made more concentrated [50]. The osmotic virial expression predicts oscillatory depletion repulsion

force. This is believed to happen because the attractive van der Waals forces between small and big particles can increase the depletant concentration in the gap [50], which leads to a greater concentration of small colloids in the narrow gap between the big colloids and so the osmotic pressure acts in opposite direction. Right now, we are unable to provide substantiated proof experimentally for either of these hypotheses although we are more inclined towards the first hypothesis because of the previously made arguments. One way to prove a definitive answer is to directly measure the entropic forces between the microspheres which are out of scope of this thesis.

3.4 Selective depletion interactions on structured surfaces (edges)

We now know that entropic effects in colloid/polymer mixtures can give rise to particle-particle attractions and even stronger attractions between particles and flat walls. Can we use the same polymer system to cause the particles to position themselves on specific locations on structured substrates? Indeed we can. It is possible to create entropic force fields that can trap the colloidal particles at a certain geometric features on surfaces. Colloidal spheres moving in the vicinity of steps, grooves or edges located on a substrate can be attracted to these geometries, provided they have the desirable depletion potential. Dinsmore *et al*. have reported observations regarding the deposition of particles at step edges [75], near corners [37] and in vesicles [90]. This ability to trap dispersed particles at specific points on a substrate may be a very useful technique for microfabrication technologies employing directed self-assembly. In their work on colloidal crystallization on patterned surfaces, Lin *et al*. urged that particles in contact with walls of a grating groove experience an attractive force roughly 4 times the particle-particle value [38].

To study interactions of particles with edges, we first had to device structured surfaces with periodic surface topologies. Silica substrates were chosen as deposition platforms because of their semiconducting properties and directed self assembly gaining momentum for semiconductor fabrication. We have already shown that we can deposit surface crystals readily on flat silica substrates, so we expect the particle-edge depositions should be every bit feasible on these surfaces. Recurring patterns constituting grooves were etched on silica surfaces using Bosch process on STS ICP etching. The dimensions of the structures were measured using scanning profilometry. The structures consisted of rectangular grooves that are approximately 3 μm deep, but the width (groove) varied from 20 μm to 10 μm. The dimensions of the rectangular structure varied between 70 μm to 100 μm, while the spacing between each of these structures is 1.13 mm. In Chapter 2, we have stated that the excluded overlap volume for particle-edge geometry is exactly twice that of particle-wall. We would therefore expect the particle-edge interaction to occur at concentrations lower than the particle-wall interaction. In our experiments, we tuned the C_s & C_p using our mathematical models such that the particle-edge depletion potential has approximately the same magnitude of particle-wall potential where particle-wall crystals appeared in copious amounts. As seen in Chapter 2, our mathematical models can compute the interaction energies for all possible outcomes, as in particle-particle, particle-wall and particle-edge interactions. We attempted to fine-tune the system parameters (C_s, C_p, R_g, R_L) such that the conditions for particle-edge interactions were optimum whilst other interactions (particle-particle, particle-wall) are less favorable. Obviously, the numerical models cannot capture the precise concentrations at which edge nucleation occur due to model idealization and also due to

the unpredictable electrostatics involved between the particles and surfaces. Although numerical models can state otherwise, it is quite a challenging assignment is to make these edge interactions highly selective. This is a difficult undertaking because of the vast amount of flat surface area available on the substrates where particle-wall collisions can result in deposition reducing the probability of particle-edge collisions in the system. Therefore, in cases where edge-nucleation was expected to occur, but was not found might be a result of kinetic limitation. Oftentimes, edge nucleation was associated with surface nucleation on the flat surfaces or in the grooves. To attain high quality edge nucleation, we slowly diminished the values of C_s and C_p until nucleation on the flat surface is absent and nucleation at the edges remain. Steadily, we observed that crystals would form in the edges before nucleating on the flat surfaces or in the bulk.

Our initial set of experiments in search of edge nucleation raised concerns about the density-mismatch between the particles and water, so the water used in the latter experiments was a mixture of D_2O and H_2O to create near-neutral buoyancy conditions for the PS colloids. The density-mismatch increased the possibility of sedimentation/particle-wall interactions (deposits), thereby decreasing the PS particle concentration in the bulk which minimizes the frequency of particle-edge collisions. The sample chamber consisted of the etched silicon wafer glued to a glass slide and a cover slip on the other side. The sample consisting of the binary solution of PS/PEG suspension is squeezed in-between the cover slip and the etched silicon wafer forcing the colloidal particles to interact with the geometric structures on the substrate. We emphasize that the magnitudes of C_s and C_p have to be chosen in such a way the particle-wall interactions are not too strong, so they can diffuse freely along the surface of the wall to find an edge

where they bind. We recorded images of the samples over a period of days to look for edge crystals of PS spheres. After sample insertion, samples were placed on a slow roller to prevent sedimentation of the particles. This was a necessary step because edge nucleation was not readily observed like surface or bulk nucleation. At a certain values of C_s and C_p, we observed edge crystals as well as a surface crystal forming alongside the edge or on a flat surface (see Figure 3.3 (b)). For these concentrations, the particle-wall, particle-particle interactions still exist and can occur either alongside the edges or on flat surfaces because it further stabilizes the edge nucleate and the Helmholtz free energy is decreased as a result of these multiple interactions. As we decreased the interaction strength, we noticed linear crystals (see Figure 3.3 (a)) forming along the edge meaning the particle-wall interactions were not strong enough anymore. Each particle in this linear crystal was interacting with an edge as well as adjacent particles. As we further decreased, we singled out particle depositions in the edges without any particle-particle interactions. At this point, particle-wall and particle-particle interactions are almost non-

a)   b)
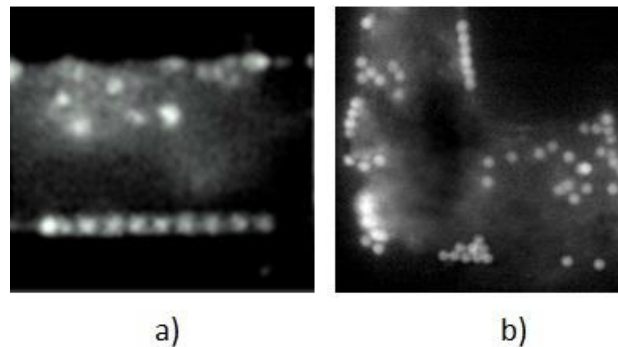
Figure 3.3 a) A linear edge crystal along the edge (0.05 wt % PS, 0.015 wt% PEG, 0.015M NaCl) and b) shows both linear (top) and edge-surface crystal (0.05 wt % PS, 0.015 wt% PEG, 0.02M NaCl).

existent.

Although we observed particles nucleating in the edges, the number of occurrences of edge nucleation was extremely rare and they appeared to take at least 24-48 hours to deposit at the edges unlike surface and bulk nucleation which occurred spontaneously. Also, the edge-surface crystals forming along the edge did not compare with the physical dimensions of the pure surface crystals. This might be due to the undulating sidewall formation and surface roughness caused on the silicon structures created using the Bosch process. Bosch process involves etch/deposit steps that are repeated many times resulting in a large number of very small isotropic etch steps taking place only at the bottom of the etched pits. This two-phase process causes the sidewalls to undulate with an amplitude of about 100–500 nm [91] which is of the order of the size of our depleting agent. Geometrically speaking, depletion forces are maximized for smooth surfaces compared to rough surfaces as excluded volume overlap can be very inefficient when two rough surfaces approach each other. Zhao *et al*. have shown that depletion forces are maximized for smooth surfaces and can be suppressed considerably when the nanoscale surface roughness becomes larger than the depleting agent [92]. Evidently, the depletion interactions in our case will definitely be subdued due to this geometric criterion. Surface roughness of the order of the particle size can cause huge deviations between the actual excluded volume overlap and our model calculations. Therefore, our theoretical and model predictions for the depletion interactions are valid only for regular smooth surfaces and does not entirely apply on these structured substrates. One other reason might be the low concentration of the PS particles used for these experiments. Although the entropy of the smaller species dominates over the larger species, the latter
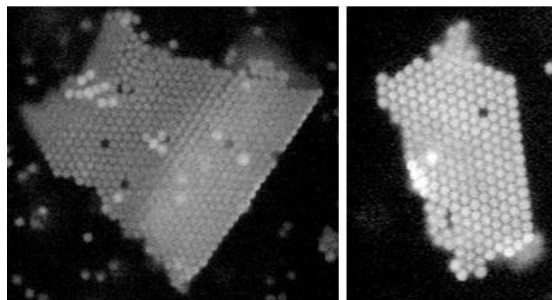
Figure 3.4 Surface crystals found on structured surfaces with linear boundaries on one side (0.1 wt % PS, 0.035 wt% PEG, 0.025M NaCl).

can be of slight importance. For particle-edge binding to occur, it would help if the interaction energy is large enough to overcome the entropy penalty that is accompanied from the particle-edge deposition. The entropy penalty depends on the concentration of PS particles. Higher concentration of PS results in smaller entropy to begin with (for each individual particle), so the energy needed to overcome the loss in configurational free energy is small. A smaller concentration of PS particles would mean more configurations for each individual particle (more entropy), so the price paid for particle deposition is much more in this case. So picking the right concentrations of the bigger species can make things more feasible and can be an important criterion which is not revealed in the numerical modeling. However, larger volume fractions could not be used because of the optical microscopy limitation. Using high concentrations of PS makes it extremely difficult to get clear details of the edge deposition in the silica structures. Dinsmore *et al*. used a volume fraction of 0.015 for the bigger species (PS, 0.474 µm) of the binary suspension to achieve nucleation in the corners [37]. Using a high concentration also increases the frequency of a particle-edge collision which can eventually lead to the formation of an edge crystal. Using a low concentration can make this collision a rare

event. Increasing the concentration increases the likelihood of a particle-edge collision by a large factor. For most of our edge nucleation experiments we used a modest volume fraction of 0.005 for the PS spheres while we used a volume fraction of 0.001 for surface nucleation. Another reason could be that crystals forming along the edges might break loose and diffuse along the flat surfaces making us believe these are surface crystals. It was observed that some of the surface crystals that were formed on these substrates had a nearly linear boundary (see Figure 3.4) on one side which could have very well formed along an edge before breaking off.

3.5 Phase diagram

The phase diagram which has been generated from these systematic experiments to represent these varieties of depletion interactions graphically has polymer concentration (C_p) on the X axis and salt concentration (C_s) on the Y axis. It shows the respective color coded regions where we can almost selectively obtain the various kinds of depletion interactions that were discussed. There is also a region of stagnation inactivity shown on the phase plot (shown in red) where C_s or C_p (or both) is too little to overcome the electrostatic repulsion between the geometries of interest. The first signs of depletion interactions as can be seen in the phase plot are edge nucleation as shown in the pale-blue shaded region. By increasing C_s or C_p (or both), we see a region where surface nucleation is exclusive (green) followed by a region where both surface and bulk nucleation (yellow) compete. As we further increase the concentrations we see a region where bulk nucleation (blue) is exclusive which is followed by a region of aggregation (grey) in the bulk as a result of particles getting too close and van der Waals forces kicking in. Nevertheless, it should be reminded that individual particles and sedimentary

aggregates were seen to be stuck on the confining surfaces for the cases of bulk

nucleation and aggregation probably due to the decreased repulsive barrier. Clearly, our

numerical modeling computations agreed accurately with the order of interaction strength

for the various depletion interactions that were probed here.

Direct measurements for the depletion potential in the isotropic spheres is more

than 5 k_BT [81]. But the electrostatic repulsions between the particles and surfaces play an

important role in determining the depth of the depletion potential well. We computed the

polymer concentration for which the depletion interaction solely is 5 k_BT for the various

kinds of interactions observed and marked them on the X axis. Although edge nucleation

seemed to occur precisely at this checkpoint, surface and bulk interactions occurred for
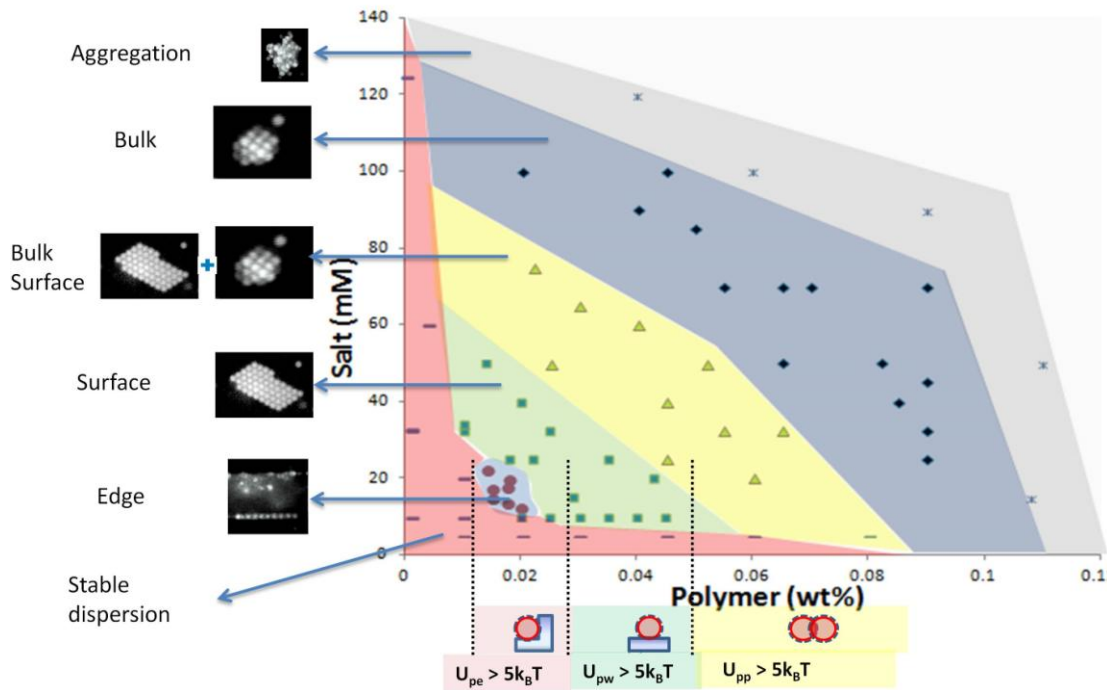
Figure 3.5 A phase plot of all the depletion interactions shown as a function of electrolyte and polymer concentrations. To the left we show the each of the interactions on the phase plot. To the bottom, we show the positions on X axis where each of these interactions are 5 k_BT in magnitude.

73

even lower polymer concentrations as the electrolyte concentration increased. This is because, although the particle-wall interactions are weak, they are associated with particle-particle interactions on the side resulting in a stable hexagonal surface-crystal formation which grows until thermodynamic equilibrium is reached. At this point, each particle not only interacts with the flat surface but also with six other particles in the hexagonal lattice structure. The same is true for bulk interactions as they form honey-comb like hexagonal close packing (HCP) structures and each particle is in contact with as many as twelve other particles which enhance its interaction strength greatly. This can also been seen in the viewpoint that the driving force for forming HCP crystal is much more as the region of excluded overlap volume is tremendously increased for this lattice configuration, thus increasing the entropy of the polymer by a large extent. The electrostatic interactions between the particles and surfaces are probably responsible for the irregularities observed between the model predictions and experimental observations. If one looks closely at the phase plot of the depletion attractions, the phase boundaries of each of the interactions appear to look like the hypotenuse of a right triangle formed with the axis being its two sides. This triangle shape of phase plot clearly indicates that electrostatic interactions are as important as depletion interactions for this self assembly process. This is because the depth of the depletion potential well can be increased by either increasing the electrolyte concentration (which screens the repulsions) or by increasing the polymer concentration (which increases the attractions). As a result the phase plot has a triangular shape which means that once we get above a certain value of electrolyte /polymer concentration; we can only get to a certain kind of interactions. However, this is not an obvious result to see mathematically. Due to the triangular shape,

74

there seemed to exist a certain electrolyte concentration for every interaction above which they cease to exist and a different kind of interaction comes into play. For example, the edge nucleation doesn't exist above the electrolyte concentration of 20 mM. This is possibly a result of kinetic limitation rather than a thermodynamic (energetic) limitation, meaning we seem to believe that this is just a matter of the interactions with the surface being too strong and the particles not being able to diffuse and explore the phase space. It is easier to explain why the horizontal transition occurs. As the polymer concentration is increased, the interactions become too strong and other interactions start to become dominant. It essentially becomes a selectivity effect. It is also easier to see that as you increase the electrolyte concentration, the interactions happen at lower polymer concentration because there are less repulsive forces and it is relatively easier for the particles to get closer to the interacting surfaces. Thus it can be safely concluded from the phase plot that there exist interesting windows of opportunity in these entropy-driven self assembly systems, where highly selective particle assembly is possible for a certain polymer and electrolyte concentrations. Yodh *et al*. has previously generated a "quasi-phase diagram" which shows exclusive regions of particle assembly on surfaces and bulk complications divided by a "liquidus line" [58]. But they have performed this for a fixed ionic strength keeping the electrostatic influences out of the picture. Also, they classified only two kinds of interactions using their phase diagram. Therefore, we are convinced that our phase plot is more informative and can be used as an invaluable tool in investigating these dynamic systems since a potpourri of all possible depletion interactions on these substrates have been depicted using this simple geometric representation.

3.6 Kinetics of crystallization on flat substrates

To investigate the kinetics of crystallization on a flat surface, we conducted deposition studies on flat glass substrates as a function of time. Figure 3.6 shows the rate of crystal growth process of a colloidal crystal on a flat substrate as a result of the depletion interactions. The kinetics of crystal growth can be seen as a two step process: the diffusion of a colloidal particle towards the growing crystal can be seen as a transport step and the deposition of the particle on the growing crystal can be seen as a reaction step. Therefore, PS particles have to diffuse around and reach a location on the crystal to deposit or stick to aid to the crystal growth process. Using this terminology, diffusion
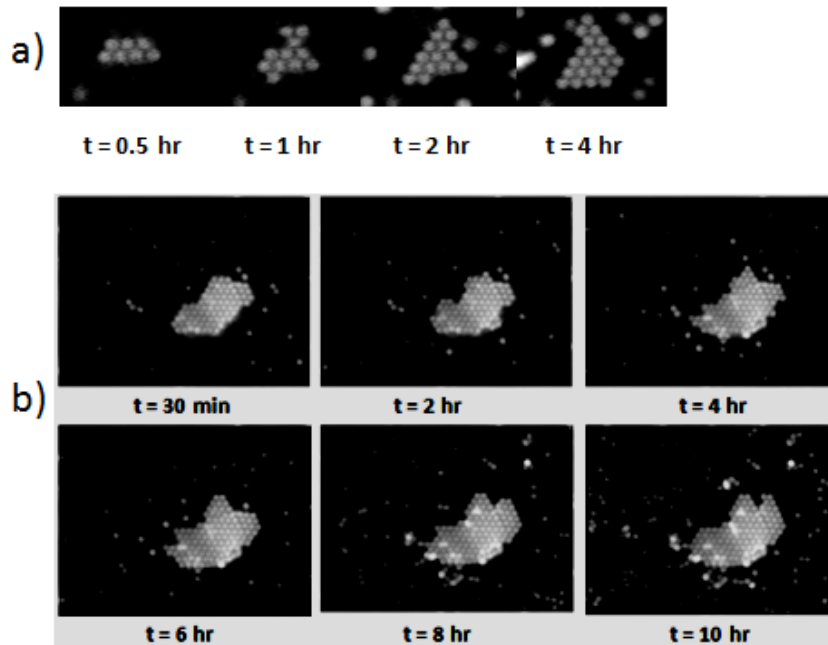
Figure 3.6 Time-sequence of fluorescence microscopy images that show growth of a depletion-induced colloidal crystal of 1 μm (diameter) fluorescent PS particles in an aqueous solution of PEG (MW=1,000,000) on a glass microscope slide for a) 0.15 wt % PS, 0.02 wt% PEG, 0.05 M NaCl (U_{pw} ~ 4.2 kT) and b) 0.1 wt % PS, 0.025 wt% PEG, 0.05 M NaCl (U_{pw} ~ 6 kT).

limited reaction leads to a full blown aggregation and a reaction limited reaction leads to a very weak interaction.

In many cases, the interaction of an individual PS sphere with the flat substrate might be too weak to establish a stable interaction. Therefore, a surface-crystal formation is preferred over a single particle-wall deposition because each particle in the crystal has additional particle-particle interactions depending on the number of neighbors to create a more stable structure. The rate of crystal growth on flat surfaces was investigated in-situ using video microscopy techniques. We used density-matched medium (a mixture of D_2O and H_2O) to create near neutral buoyancy conditions for the PS colloids in order to prevent sedimentation and keep a fair amount of concentration in the bulk. We investigated the surface assembly for a fixed electrolyte concentration but varying PS and PEG volume fraction (see Figure 3.6 for details). We chose these concentrations for electrolyte /polymer because these were deemed to be sweet-spots for surface nucleation from our previous observations. For both the concentrations, the growth rate was relatively slow probably due to low PS particle concentration which can adversely affect the collision frequency of the free particles with the growing crystal.

Crystal growth occurs through formation of a surface nucleus which further grows in size through subsequent addition of surrounding particles to form a hexagonal symmetrical crystal. While the nucleus forms almost spontaneously after the introduction of the non-adsorbing polymer, crystal growth happened slowly and can be considered as the rate determining step for surface crystallization process. While thermodynamics always favor the formation of larger nuclei (Ostwald ripening) because of the greater volume top surface ratio [93], it is mentioned in the literature that the size of the nuclei is

dependent on the interaction potential. A stronger attraction should lead to a smaller critical nuclei and a weaker attraction to a larger nuclei. The growth rate of the cystallization can be significantly enhanced using particles that are an order of magnitude smaller. This is because the free particle collision frequency with the growing nucleus will be enhanced significantly as particle diffusivity is inversely proportional to the size of the particles.

For the concentrations probed in our experiments, it was observed that higher interaction strength resulted in a bigger crystal formation. This can be explained kinetically as diffusion limited reaction where a stronger attraction makes each of the PS-crystal binding more probable resulting in a larger crystal size. Similarly, smaller interaction strength follows a reaction limited mechanism and therefore, the likelihood of a PS-crystal interaction resulting in binding is lesser. It was also observed that the growth rate of the crystallization process was enhanced using a higher concentration of PS particles. This is due to the increased crystal-PS collision frequency due to the increasing bulk concentration of PS. However, this can also result in an increased number of nucleation sites although we have no means to quantify this hypothesis. For now we conclude that more quantitative and qualitative analysis is needed to give more insights into this process.

3.7 Conclusion

In this chapter we have introduced a simple model that exists in literature for the depletion interaction potential in basic geometries. The numerical models that were developed in Chapter 2 to compute depletion interaction strengths for simple geometries

like sphere-sphere, sphere-wall, and sphere-edge geometries were used to guide us (choosing C_s or C_p) with the experimental studies in this chapter to make each of these interactions highly selective. The strength and order of these interaction strengths agree with the numerical predictions. Particle-edge nucleation occurs at very small salt and polymer concentrations followed by particle-wall nucleation followed by particle-particle nucleation followed by aggregation. However, edge nucleation was extremely rare and did not occur spontaneously like the particle-wall and particle-particle interactions. This was most likely due to the surface roughness associated with the structured silica substrates. The different varieties of interactions observed were plotted on a phase plot as a function of polymer and electrolyte concentration. The triangular shape of the phase plot emphasizes the equal importance of electrostatic interactions in obtaining various forms of interactions, which were ignored by previous researchers. However, this triangular shape is not very obvious to see mathematically. We have also performed studies pertaining to the rate of growth of surface crystals where the rate was investigated for different volume fractions of PS and PEG. Due to inadequate amount of experimental data, it is hypothesized that the size of the surface crystal depended on the strength of depletion attraction and the rate of surface crystallization depends on the volume fraction of PS. More quantitative and qualitative analysis needs be done to validate this hypothesis.

While our depletion modeling studies and experiments can paved way for particle depositions on 2D/3D surfaces, these investigations did not examine the permanent deposition of the particles onto surfaces of interest. Once the depositions are allowed to happen, it is important to permanently bind the particles to these positions for a durable

self-assembly process. While using polystyrene (PS) particles as large species, we suggest a mild annealing step above the polymer glass transition temperature (T_g) to cause the polymer to melt and secure the deposition. Since $T_g = 95°C$ for PS, aqueous solutions can no longer be used. Fleming et al. have demonstrated that heating PS colloids to 170–180 °C in ethylene glycol leads to the desired fusing of PS particles into a uniform coating [94]; We suggest these permanent depositions conditions should be investigation for future considerations.

Chapter 4

Hydrodynamic interactions of polystyrene and toluene-swollen

polystyrene spheres in confined systems

4.1 Introduction

In this chapter, we present microscopic observations and quantitative analysis of the hindered diffusion of micrometer-sized hard and soft polymer particles confined between two parallel walls. The fundamental question that motivated this investigation is "Does particle softness affects the particle-wall hydrodynamic interactions?" Particle tracking video microscopy (PTVM) is used to determine the free and confined diffusivities of the hard and soft particles. Hydrodynamic coupling between particles and confining walls is known to hinder Brownian diffusion of hard spheres.

The hydrodynamic interaction between a particle and a wall is of much practical importance in colloidal flow for both thermal diffusion problems (transport in small pores) and pressure driven flows. Here we will focus our study on the low Peclet number regime where Brownian motion (thermal diffusion) is more important and the Stokes-Einstein equation is valid. The hydrodynamic interaction between a hard sphere and a wall is predicted accurately by theory. For gravity driven flows, in the late 19th century Reynolds stated that in the limit of a small gap width, the drag coefficient $f = F/v$ (F being the drag force and v the speed) scales inversely proportional to the distance between the wall and the sphere [95]. Faxen provided asymptotic numerical solutions for

hydrodynamic interactions between a rigid flat wall and a rigid single sphere [96], whereas the Brownian motion of a hard sphere confined between two hard walls has been studied experimentally and numerically by a number of researchers [97, 98]. While the unbounded Brownian diffusion of colloidal spheres in an infinite medium is well understood [99], the dynamics of near-wall hindered colloids is complex when hydrodynamic interactions are involved. Hindered diffusion of colloids confined between parallel walls provides us with a model system to understand complex systems whose boundaries can be modeled as solid walls, for example, particles diffusing in porous media [100], nanoparticles for drug delivery vehicles in tissue [101], or macromolecular diffusion in membranes [102]. Hard sphere confinement between parallel walls has been studied extensively via light scattering [103], PTVM coupled with optical tweezers [104] and total internal reflection microscopy [105]. However, most of these experiments were performed under relatively mild confinement, as defined by particle to gap size ratio [103, 106-108], or quantified hydrodynamic interactions between particles, rather than between particles and walls [104, 109].

Unlike hard colloids, the effects of confinement on the mobility of soft colloids are poorly understood, with very limited experimental data, despite the fact that their confinement is rather common in many fields of study. Potential application areas where lateral hydrodynamic interactions between soft colloids and rigid surfaces at low Reynolds number is important are tribology of liquid-surface interactions [41], transport of oil emulsion drops in porous media (enhanced oil-recovery) [43], biological cells interacting with surfaces [110], rheology of emulsions [111], emulsions in microfluidic devices [44, 45], deposition of droplets on walls, and near-wall motion of drops in packed

columns [46]. For example, tribological properties are governed by hydrodynamic lubrication forces and determine the quality of emulsions or emollients in consumer products (food, skin cream) which can ultimately influence the decision-making process of the consumer [112]. Similarly, the use of oil-water emulsions as mobility control agents in enhanced oil recovery methods requires full understanding of emulsion flow through constricted porous media, during which the drop diameter can be of the same order of magnitude as the pore throats [43]. In the following sections, we will present and discuss the differences between drop and hard sphere behavior, and consider how the softness associated with the drops affects the drop hydrodynamics. In the subsequent sections, we will present the results, analysis and discussion of our research. It should be noted that the word drop is used loosely for highly swollen particles throughout this chapter.

4.2 Deformability and interfacial mobility of drops

When comparing drops to hard spheres, one should consider several significant differences due to the fact that droplet interfaces are mobile and deformable. It is often mentioned in literature that the interfacial mobility of drops and bubbles diffusing in aqueous solutions can produce substantial differences in hydrodynamic behaviour in comparison with hard spheres or even drops with immobile liquid interfaces [24, 25]. For example, the Hadamard-Rybczynski theory predicts that the terminal velocity of a spherical liquid droplet should be up to 50% higher than that of a hard sphere of the same size and density, when interfacial flow is allowed to occur in the drop [113]. Researchers have reported excellent agreement of experimental observations with the Hadamard-Rybczynski drag relationship for surfactant free air bubbles [114] and drops [115].

Specifically, surfactant-free interfaces have been highlighted as being important for enabling flow at the interface, which reduces hydrodynamic drag. However, it is often stated that surfactants are usually unable to fully arrest interfacial mobility, so that interfaces cannot always be treated as immobile in the presence of surfactant [116]. Arresting interfacial mobility with surfactants requires not only the adsorption of surfactant to the interface, but also the presence of localised Marangoni effects that resist the fluid flow at the interface [113]. As a result, it is expected that even surfactant covered drops exhibit enhanced mobilities relative to hard spheres. For example, the mobilities of micron-sized surfactant covered oil (triacylglycerol) droplets through porous media was found to exceed that of latex microspheres by 20% within the same size range and with similar electrostatic properties [117].

When comparing drops to hard spheres, one other important difference is that the drop interfaces are elastically deformable [118]. The capillary number (*Ca*) is the dimensionless group that is used to quantify the balance between deforming shear forces and restoring surface tension forces on a drop. For *Ca* << 1, global deformation is unimportant. However, it should be notes but this statement does not entirely hold in case of drop confinement in narrow gaps with high lubrication pressure [119]. As observed by Mulligan and Rothstein, droplet deformation was evident for *Ca* = 0, due to confinement effects alone [120]. Although small drops possess high capillary pressure that opposes their deformation, they are also subject to more intensive Brownian motion, giving rise to additional shear forces that could enhancing the deformation [121]. There are many situations where small droplets are readily deformed. For example, micro emulsions with low interfacial tension (usually below 10 dynes/cm) are amenable to deformation even

when the drops are smaller than 100nm. Such drops exhibit Brownian motion and deform under the action of hydrodynamic and surface forces [122]. In a recent study by Saiki *et al.,* it was concluded that SDS stabilized PDMS "soft" droplets (1.7±0.5µm) deform at droplet volume fractions well below the colloidal glass transition volume fraction due to hydrodynamic forces [111]. In the same study it was concluded that the absence of shear thickening in emulsion systems at volume fractions greater than random closed packing is due to droplet deformation and surface mobility. However, surfactant stabilized drops are often treated theoretically in the same way as suspensions of solid particles. Although this is certainly true for the case of very small drops (below one micrometer) with high interfacial tension [123], it's applicability for all surfactant drops is somewhat questionable. In addition, researchers have experimentally studied flocculation of micrometer sized drops and interpreted the results using the drop deformation hypothesis under certain conditions [124, 125]. It was also shown that drop deformability will impact both direct (*e.g.*, electrostatic) and hydrodynamic interactions as these interactions are sensitive to the shape of the interacting surface and the thickness of the lubrication film [8].

The above discussions support the hypothesis that the hydrodynamic hindrance of a drop moving near a solid surface will be reduced relative to a hard sphere due to the interfacial mobility and deformability of the drop. This should apply to both laterally translating and laterally diffusing drops close to a rigid surface. To date, very few experimental studies have reported on wall hindrance effects on laterally moving drops [126]. The majority of the existing studies on interactions between droplets and rigid surfaces have focused on normal (perpendicular to surface) rather than lateral (parallel to

surface) hydrodynamic interactions [127-130]. In this work, we demonstrate an experimental set-up using PTVM that enables the indirect measurement of lateral hydrodynamic interactions of colloidal particles (hard and soft) diffusing between two parallel walls. These measurements are followed by control experiments that further highlight the differences in hydrodynamic behaviour between hard and soft colloids under confinement. Monodispersed toluene-swollen polystyrene particles are used as model systems for "non-hard" or soft spheres. Conventional emulsion drops could not be used because it is not a trivial task to synthesize highly monodispersed micron sized emulsions. Polydispersity can significantly increase the error bars in our statistical interpretation, which undermines the ability to draw strong conclusions. Although the toluene-swollen spheres are not a perfect model system for drops due to their residual viscoelasticity, they behave significantly different than hard spheres as we will see in the discussions below.

4.3 Materials and experimental setup

PTVM was utilized to measure the hindrance coefficients for the Brownian motion of colloidal spheres between parallel solid walls. A drop of dilute suspension containing a mixture of the colloids of interest and silica spacer particles (diameters 1.61, 1.85, 2.06, 2.28, 3.01 and 4.63 μm; Bangs Laboratories) was loaded between two microscope cover glasses (VWR: 18x18, Cat. No. 48366; Fisherbrand: 24x50, Cat. No. 12-544-E)   and excess liquid was removed to create a uniform quasi-2D suspension in a confined cell in which the spacing between walls is defined by the size of the mono-disperse silica spacers. For free diffusivity measurements, the samples were loaded into ~100 μm thick sample chambers that were created by placing parafilm spacers between two cover
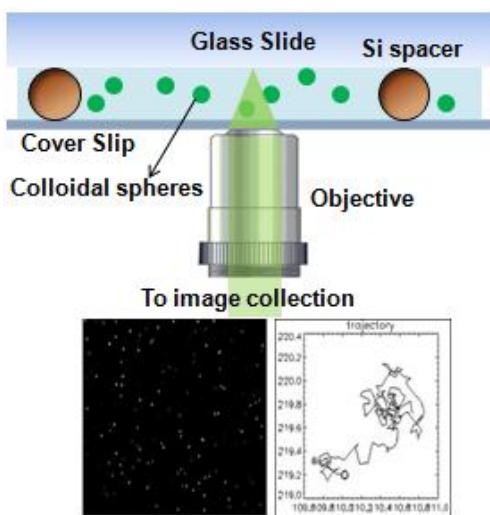
Figure 4.1 Schematic of the experimental setup. A representative particle tracking image of the fluorescent particles obtained using microscopy is also shown.

glasses. The samples were sealed with vacuum grease to prevent evaporation of the sample. The Brownian motion of the colloids was monitored via an inverted optical microscope (Leica DM-IRB) with 63x objective and movies were captured using a CCD camera (Cohu 4920, Poway, CA; 30 frame/s and 640×480 pixel resolution). Subsequently, the recorded movies were analyzed with software developed using Interactive Data Language (ITT Visual Information Solutions, Boulder, CO). Because Brownian motion leads to small particle displacements on these timescales and is highly sensitive to external vibrational noise, all PTVM experiments were performed on a vibration-isolated optical table. The experimental setup is shown schematically in Figure 4.1.

4.4 Creation of monodisperse swollen particles

Equilibrium swelling processes of polymeric colloidal particles with water-insoluble

organic solvents are of considerable interest for different applications, including the optimization and control of emulsion polymerization [131]. A basic understanding of the swelling mechanism is essential in order to determine the factors that govern the equilibrium swelling of latex particles. Highly swollen polymer particles behave more like emulsion drops than solid spheres and exhibit basic fundamentals of drop dynamics, like Ostwald ripening [131]. In this discussion, the swollen latex particles are treated like droplets that contain dissolved polymer. The Morton-Kaizerman-Altier (MKA) equation [132] has been widely used to describe the equilibrium swelling of polymer latex particles. Morton *et al.* assumed that in the absence of a cross-linking agent, the resistance to swelling is simply the interfacial free energy between the latex particle and the surrounding aqueous medium. Therefore, for a swollen particle in equilibrium with free solvent, the partial molar free energy of the solvent can be written as:

$$\Delta G = \Delta G_o + \Delta G_i = 0 \qquad (4.1)$$

where ΔG_o is the osmotic contribution to the Gibbs free energy and ΔG_i is the interfacial free energy contribution to Gibbs free energy. Using the Flory-Huggins theory[133], the expression for ΔG_o can be written as:

$$\frac{\Delta G_o}{RT} = \left[\ln(1 - \phi_p) + (1 - m_{AP})\phi_p + \chi_{AP}\phi_p{}^2\right] \qquad (4.2)$$

where subscripts A, P refer to the solvent and polymer molecules, ϕ_p is the volume fraction of the polymer, m_{AP} is the ratio of equivalent number of molecular segments of solvent to polymer and χ_{AP} is the Flory-Huggins interaction parameter. If r is the radius

of the particle at swelling equilibrium and *dr* represents the increase in radius due to absorption of *dn* moles of solvent, the increase in particle surface area would be $8\pi r dr$. If *γ* represents the interfacial energy at swelling equilibrium, the increase in interfacial energy would then be $8\pi r dr\gamma$. Also, the increase in volume of the swollen particle would be $4\pi r^2 d$, which can also be written as $dn(MW)/\rho$, where *MW* is the molecular weight of the solvent and *ρ* its density. From this, it is obvious that

$$8\pi r dr\gamma = \frac{2dn(MW)\gamma}{\rho r} = \frac{2dn\overline{V}_A\gamma}{r} \tag{4.3}$$

where $\overline{V}_A$ is the molar volume of the solvent. Hence the interfacial free energy contribution can be written as

$$\Delta G_i = 2\overline{V}_A\gamma/r \tag{4.4}$$

Combining equations (4.1), (4.2) and (4.4), we finally arrive at:

$$\left(\frac{\Delta G}{RT}\right)^P_A = \left[\ln(1-\phi_p) + (1-m_{AP})\phi_p + \chi_{AP}\phi_p^2\right] + \frac{2\gamma\overline{V}_A}{rRT} = 0 \tag{4.5}$$

Assuming a high polymer molecular weight (and therefore a high degree of polymerization) at equilibrium, it follows from (4.4) that

$$-\frac{\ln(1-\phi_p) + \phi_p}{\phi_p^2} = \chi_{AP} + \gamma\frac{2\overline{V}_A}{rRT\phi_p^2} \tag{4.6}$$

89

Using Equation (4.6), for a given polymer system, it was deduced that the equilibrium solubility of latex particles is a function of the particle diameter and the interfacial energy at the surface of the particles. For a specific polymer-solvent system, one can estimate the swelling equilibrium of a latex particle, which is only a function of its size, provided that the interfacial energy is kept constant. Under these conditions, one can also predict both χ_{AP} and γ for the system using the equilibrium swelling data. For the case of polystyrene-toluene system, Morton *et al.* estimated these parameters to be 0.48 and 3.5 dynes/cm respectively [132]. The value for χ_{AP} quoted in the literature is 0.44, which is not too far off [134]. Thus, using Equation (4.6), one can estimate the equilibrium solubility in latex particles for any given solvent and this knowledge can be used to control the parameters of the swelling mechanism.

In our study, swollen polystyrene particles were prepared by a simple systematic swelling technique using toluene (99.8% reagent grade, purchased from Alfa Aesar) as a swelling agent and SDS (purchased from Sigma Aldrich) as the anionic surfactant to impart stability to the droplet interface during swelling. Hard fluorescent carboxylate-modified polystyrene FluoSpheres® (Molecular probes, Inc.) with 1.06 μm diameter and 3 % polydispersity (PD) were used (measurements using IDL). Before adding toluene, we first added PS particles (solid content ~2 wt %) to a 5 mM SDS aqueous solution and stirred the resulting suspension for 1 hr. The solid PS beads were then swollen by adding toluene, which is a water-insoluble organic solvent. The size of the swollen particles was varied by adding different amounts of toluene to the aqueous solution of polystyrene suspensions. The resulting suspension was stirred for 5 hrs, which is long enough for the PS particles to reach equilibrium (as we will see in the next section). However, it was

observed that PS particles absorbed only a limited amount of solvent that was added to the aqueous solution. This was evident from our calculations of swelling ratios based on the amount of toluene that was added to the suspension, assuming full incorporation of toluene into the PS particles. After toluene insertion, the PS polymer transitions from a solid state to a dissolved state in toluene, thus increasing its entropy due to increased number of accessible conformations. In addition to the surfactants, coalescence between the swollen beads during the swelling process was further suppressed by choosing PS beads with a negatively charged carboxylate group on the surface as starting material. The number averaged PD of the swollen particles was found to be 9% which is still low and doesn't affect our statistical data largely. One of the key reasons we use swollen particles as our soft spheres is because they are relatively monodisperse when compared to the emulsion systems synthesized on the same order of lengthscale. The increase in PD from 3% to 9% is believed to be caused by the inter-particle collisions and thus exchange of materials between the swollen particles during the stirring process. Swelling processes are commonly associated with heterogeneities and increase in polydispersities [135].

It should be noted that while surfactant was primarily used to provide stability to the particles during swelling, it also reduces the interfacial surface energy of the particles. Researchers have shown that depending on the surface coverage obtained, surfactants can thus strongly enhance the swelling of the polymer latex particles [136]. For example, Morton *et al.* noticed that the PS latexes absorbed more than double the amount of swelling agent (styrene) with surfactant than without [132]. Surfactant micelles can further enhance swelling because they can solubilise the additional solvent, while the

adsorbed surfactant can also attract more solvent due to the interactions between the hydrophobic surfactant tail with the solvent and the polymer within the particles. This super-swelling effect due to surfactants is present only in small particle sizes (< 50 nm) and the effect vanishes for larger particles [136]. The MKA equation was shown to fit fairly well with the experimental swelling data in which the latex surface is saturated with surfactant and has been used by researchers to obtain values for the interaction energy and Flory-Huggins interaction parameter from the equilibrium swelling data.

4.5 Swelling dynamics

To determine the rate at which toluene is absorbed by the PS particles, we measured the radius of the swollen PS particles as a function of time after the insertion of toluene. We performed these measurements both in presence and absence of SDS surfactant to examine its effect. Figure 4.3 shows the swelling curves in the presence and absence of surfactant; the fact that the curves are nearly identical supports literature claims that the surfactant effects on the swelling mechanisms are limited for relatively large particles [136].

After the addition of toluene, it was observed that the saturation of the PS latex was maximum after approximately five hours. The swelling ratio is defined as the ratio of the diameter of the swollen PS latex to the unswollen, hard PS latex. A decrease in size was observed for long times due to evaporation of toluene from the swollen PS beads. When the swollen sphere suspensions were left out to evaporate at room temperature (22 ºC) and exposed to air for 24 hours, they reverted back to their original dimensions, thus confirming the reversible nature of the swelling processes. An important comment is that
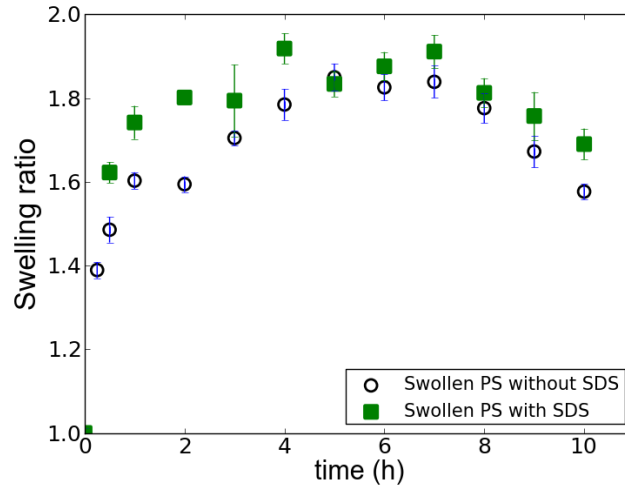
Figure 4.2 Swelling ratio of the PS latex as a function of time is shown for the absence (open circles) and presence (filled squares) of SDS surfactant.

the volumes of polymer particles and solvent are not additive, because toluene is first absorbed into the pervaded (free) volume (V_f) of the PS latex, which effectively increases the density and mass of the particle without inducing volume expansion. Only after the free volume is occupied, additional toluene leads to actual swelling of the particle. As more toluene is added, the particle density quickly drops with increasing swelling ratio due to the lower density of the added toluene. We derived a simple mathematical model to analyse connect the free volume in the PS latex particles to their overall density and the toluene uptake. The first model step is to define

$$V_f = \alpha V_p \tag{4.7}$$

where V_p is the volume occupied by the polymer particle in the solution and α is the fraction of free volume in the polystyrene latex. This allows us to formulate the droplet density (ρ) to predict the density of a given swollen particle:

93

$$\rho = \frac{\rho_p V_i + \alpha V_i \rho_t + (V_s - V_i)\rho_t}{V_s} \tag{4.8}$$

where ρ_t is the density of toluene, ρ_p is the density of the PS particle, V_i is the intitial volume of the particle and V_s is the volume of the swollen particle. While the radius of the swollen particles was determined as a function of time, their buoyancy behaviour was also closely observed to monitor the density distribution of the swollen particles. While highly swollen particles quickly rise to the top (creaming), mildly swollen particles would steadily sediment due to increased density from the toluene occupying the free volume inside the particles. Based on our observations, the swollen particles achieved neutral buoyancy around a swelling ratio of 1.35. Based on observations of neutral buoyancy at 1.35 swelling ratio, α was estimated to be close to 0.2. The values reported in the literature (0.1 at 25 °C [137]) for α are not too far off from our computed value.

Time (hr)	Toluene absorbed (ml./g. PS)	% Saturation of latex
0.25	1.88	35.1
0.5	2.44	45.7
1	3.24	60
2	3.17	59.5
3	4.03	75
4	4.73	88.5
5	5.33	100
6	5.10	95.6
7	5.23	98
8	4.64	87
9	3.77	70
10	3.05	57.1

Table 4.1 Rate of absorption of toluene in PS latex in presence of surfactant. The point of maximum saturation is reached at t = 5 h. Thereafter, evaporation leads to loss of toluene from the swollen PS latex.

For these calculations, the specific gravities of PS and toluene were taken as 1.055 and 0.866 respectively. Scholte performed density measurements of polystyrene-toluene solutions and determined the empirical formula which relates the weight fraction of polystyrene in toluene solutions [138]. We have verified the validity of the value of α by comparing the densities of the swollen particles obtained for various swelling ratios using our numerical model with the density values predicted by the empirical relation. Using this parameter α, the specific gravities of the particles at all swelling ratios were estimated to check on the severity of sedimentation/creaming of the particles. By performing these calculations, we have a reasonable methodology to predict the density-mismatch between the swollen spheres and surrounding medium and we were able to calculate the amount of toluene absorbed by the polystyrene particles as the swelling process took place. Table 4.1 shows the amount of toluene absorbed into the PS latex as a function of time. These density estimates are very useful in estimating the effect of gravity on the hindrance coefficients of heavily swollen particles which are more prone to creaming. The swelling curves presented us with the swollen sphere density estimates and a rough estimate of the equilibration time (5 h) for the particle to obtain maximum saturation. This was the reason the polystyrene particles were stirred for 5 h in the swelling process.

4.6 Hindrance models

Faxen was the first researcher to successfully study the resistance (drag) to the movement of a rigid sphere in a viscous fluid bound by two parallel flat walls. He used the method of reflections under creeping flow conditions and was able to obtain an asymptotic solution for the total hydrodynamic force acting on a sphere. Faxen's

expression for the hydrodynamic force on a sphere moving very slowly along the center line between the two plane walls is given in terms of a "wall drag multiplier, "K". The diffusive motion of a Brownian particle in a solvent of much smaller particles is described by the Einstein relation: $D = k_B T/f$ where D is the bulk diffusion coefficient, k_B is the Boltzmann constant, T the absolute temperature, and f the friction constant of the particle in the solvent. For the case of a rigid sphere in a Newtonian fluid, the friction coefficient is given by $6\pi\eta R_h$,which results in the Stokes-Einstein relation for the diffusivity of rigid spheres given by $D = k_B T/6\pi\eta R_h$, where η is the viscosity of the solvent, and R_h is the hydrodynamic radius of the particle. For a single sphere near a rigid wall, the lateral diffusion is defined as $D_{||} = f_/ D$, where $f_/$ is the hindrance coefficient that is commonly approximated as a power series [96]:

$$f_/ (R_h, h) = \frac{D_{||}}{D} \approx 1 - \frac{9}{16}\left(\frac{R_h}{h}\right) + \frac{1}{8}\left(\frac{R_h}{h}\right)^3 - \frac{45}{256}\left(\frac{R_h}{h}\right)^4 - \frac{1}{16}\left(\frac{R_h}{h}\right)^5 \qquad (4.9)$$

where h is the distance from the center of the particle to the wall, and R_h is the hydrodynamic radius of the particle (Figure 4.3 shows the schematic). While this expression accounts for the so-called far-field part of hydrodynamic interactions in case of dilute suspensions of strongly repelling particles far from the wall surfaces, it does not accurately account for the case of particle-wall interactions for very thin separations. For these more elaborated scenarios, lubrication effects that arise when two spherical particles or a particle and a wall are near contact must be included. Therefore, in order to describe the motion of the particles close to the wall more accurately, lubrication corrections are needed to represent the wall's no-slip boundary condition. The

hydrodynamic function $f_/(R_h, h)$ has been calculated in literature by analytically solving

the Navier-Stokes equation for a hard sphere near a planar wall by Goldman [29] and

Brenner [24], respectively, and can conveniently be expressed as:

$$f_/(R_h, h) = \frac{12420 \left(\frac{h - R_h}{R_h}\right)^2 + 5654 \left(\frac{h - R_h}{R_h}\right) + 100}{12420 \left(\frac{h - R_h}{R_h}\right)^2 + 12233 \left(\frac{h - R_h}{R_h}\right) + 431} \tag{4.10}$$

For a hard sphere confined between two parallel walls, the total hindrance effect of the

two walls, $f_{||}$, can be calculated via the linear superposition approximation (LSA)

suggested by Oseen [96]:

$$f_{||}(R_h, h) = \left[f_/(R_h, h)^{-1} + f_/(R_h, H - h)^{-1} - 1\right]^{-1} \tag{4.11}$$

where H is the wall-spacing. The LSA is mathematically simple and has been shown to

agree quite well with experimental results from prior studies [4]. In our horizontally

mounted sample chamber, gravity introduces an asymmetric distribution of particles with

a slightly higher particle concentration near the bottom wall for the base case of PS

particles in water. This effect is noticeable especially in bigger particles which tend to

sediment faster and reside closer to one surface than the other. Thus, the average

diffusion coefficient for hard spheres is calculated by weighting the diffusion coefficient

at each height with the Boltzmann probability P_B [106]. Using these weighing factors, the

number averaged hydrodynamic hindrance coefficient can be expressed as

$$\overline{f_{||}}(R_h, h) = \frac{\int_{R_h}^{H-R_h} f_{||}(R_h, h) \, P_B(h) \mathrm{d}h}{\int_{R_h}^{H-R_h} P_B(h) \mathrm{d}h} \tag{4.12}$$

where $P_B(h)$ is given by

$$P_B(h) = \left[\frac{1}{L}\right] \left[\frac{e^{-h/L}}{e^{-R_h/L} - e^{(R_h-h)/L}}\right] \tag{4.13}$$

and L is the characteristic Boltzmann length scale given by

$$L = \frac{k_B T}{\frac{4}{3}\pi R_h^{3}(\rho_s - \rho_0) \, g} \tag{4.14}$$

where ρ_s is the density of the hard sphere and ρ_0 is the density of the suspending medium. If the spatial distribution of all the particles were such that they all located exactly in the mid-plane ($h=H/2$) of the sample chamber, we attain what we call "mid-plane model curve" for hard-sphere confinement. The mid-plane curve is an idealized hypothetical model and its hindrance coefficients are always lower than the average values; the diffusion coefficients obtained from the mid-plane model exhibit the lowest possible hindrance, because the particles are furthest away from both confining surfaces.

The literature on droplet motion near substrates is not as developed as for hard spheres. The parallel motion of a drop in a low Reynolds number fluid at any position between two parallel plates was studied by Shapira and Haber (1988) using the method of reflections [139]. The solutions obtained using this approach were approximate and

98

needed further investigation. Magnaudet *et al.* (2002) derived analytical expressions for drag force experienced by a drop translating near a wall with higher order contributions by employing the method of reflections and used Faxen's transformation to satisfy the no-slip condition at the wall [46]. The expression for drag force (F_D) is given by

$$F_D \approx -5\pi V_B \left[1 - \frac{15}{32}\left(\frac{R_h}{h}\right) + \frac{1}{16}\left(\frac{R_h}{h}\right)^3 - \frac{105}{1024}\left(\frac{R_h}{h}\right)^4 - \frac{3}{160}\left(\frac{R_h}{h}\right)^5 \right] \qquad (4.15)$$

where V_B is the absolute velocity of the drop centroid. The same expression can also be applied for a diffusing drop with a few accommodations. Keh and Chen (2001) provided exact solutions for the same problem using a combined analytical-numerical method with a boundary collocation technique [140]. The wall-corrected drag force acting on the drop was obtained with good convergence for various cases including the case of a solid sphere. However, the above investigations were performed assuming a mobile interface for drops under non-deformable conditions. Drop deformation effects were not incorporated into any of these numerical models due to the complexity and ambiguity involved. Although we have the expression for the hydrodynamic drag of a drop near a wall, its interpretation is complicated because of the effects of adsorbed stabilizing surfactant and possible droplet deformation which can further reduce the drag. Vakarelski *et al.* (2010) evaluated the lateral hydrodynamic interactions between a deformable drop with an immobile interface and a flat substrate [126]. They found that the drag on a drop is less than the rigid sphere due to the deforming interface of the drop which increases the lubrication film thickness between the drop and the substrate. Researchers have also

shown that the drag coefficients for toluene-water systems were situated between the two limiting cases for rigid spheres and spherical bubbles [141].

4.7 Results

4.7.1 Dynamics of hard polystyrene particles under confinement

In the last few decades, researchers have investigated the Brownian motion of particles trapped between two walls via dynamic-light-scattering measurements [103] which provides ensemble-averaged results for all particles in the scattering volume and, as a result, cannot give direct insight into the mobility of particles as a function of distance to the walls. We used microscopy-based PTVM methods which provided more direct measurements of hindered diffusion near solid walls because PTVM also provides local spatially-resolved information from individual particles. Hindrance on a sphere trapped between parallel walls is measured using the hindrance coefficient $f_{||} = D_{||}/D$ with a higher hindrance coefficient implying less hindrance. $D_{||}$ is the hindered lateral
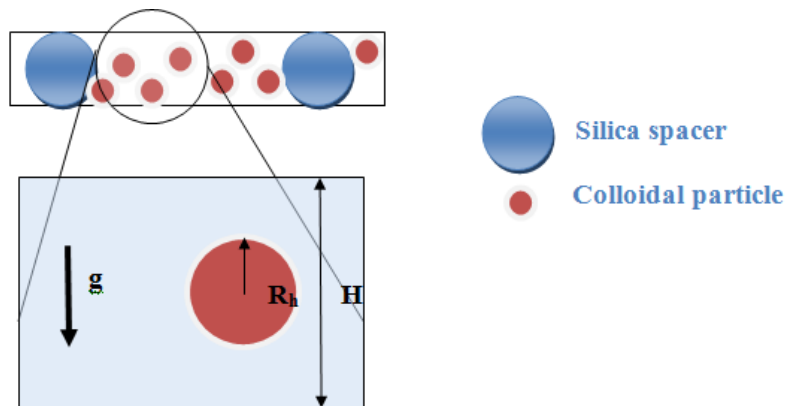
Figure 4.3 Schematic of confinement cell. H represents the spacer diameter, and R_h the hydrodynamic radius, respectively.

diffusivity and D is the Stokes-Einstein diffusion far from the walls ($\sim$ 40μm from the wall). Hindrance coefficients are plotted as a function of degree of confinement (d/H) in this study, where $d=2R_h$ is the diameter of the spherical particle and H is the wall spacing. It should be noted that previous researchers explored a much more limited range of confinement and were restricted to mild values of confinement. The distance between confining hard walls used by them was larger than twice the diameter of the confined sphere [103, 106-108]. On the contrary, our experiments cover a much wider range and strong confinement limits (0.11< d/H <0.97), which was made possible by the excellent control that we have over the wall spacing in our confinement cell through the use of monodispersed silica spacers.

We first performed confinement experiments using 1.06 μm PS hard spheres in three different background fluids: DI water, density matched water (combination of DI water and heavy water) and heavy water; to study the effect of gravity on the hindrance coefficients for various confinement limits (see Figure 4.4 a)). The density of the PS beads used is 1.055 g/cm^3 while the density of DI water and heavy water are 0.997 g/cm^3 and 1.11 g/cm^3 at 23ºC. We compared the hindrance coefficients obtained with mid-plane and average hindrance models for hard sphere confinement. While the hindrance coefficients for PS beads in DI water are in excellent agreement with the average model predictions, PS beads in heavy water and density-matched water deviate from the average model predictions. For mild confinements, the density matched samples are in line with the midplane values because they explore the bulk of the sample more than the near-wall region. For these mild confinements, the difference in diffusivities between the density-matched and unmatched samples ranges between 10 to 15% which goes to show the
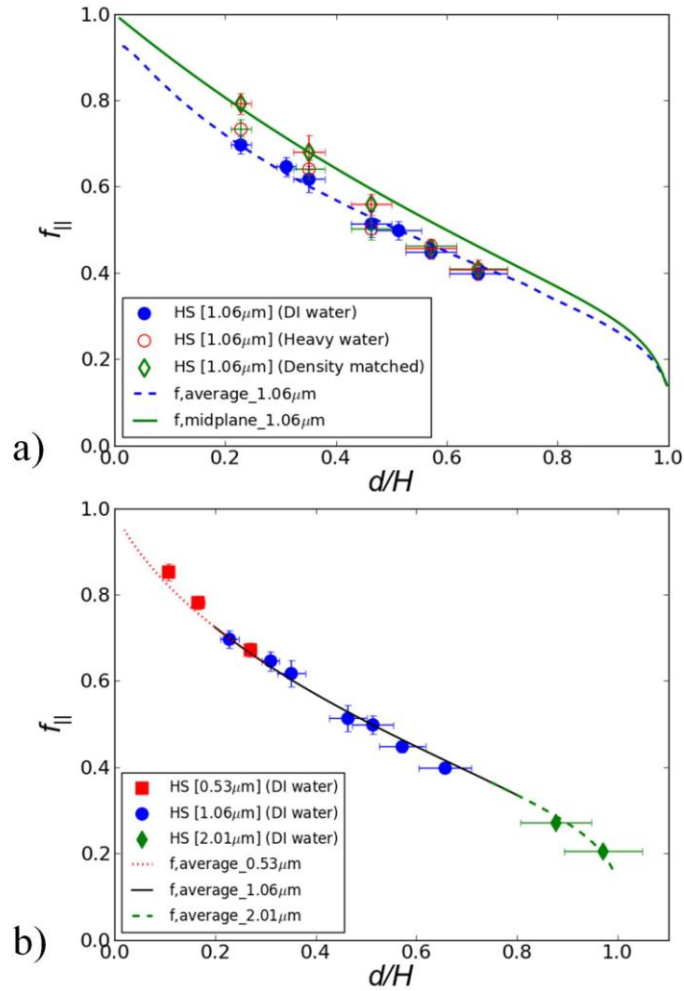
Figure 4.4 a) Hindrance coefficient for 1.06 μm PS in DI water (filled blue circles), heavy water (open red circles) and density matched (green open diamonds) water in comparison with mid-plane and average values. b) Hindrance coefficients and size-dependent average numerical models for 0.53 μm (red squares), 1.06 μm (blue circles) and 2 μm (green diamonds) PS spheres in DI water.

effect of gravity/sedimentation cannot be neglected. However at higher confinements, all three samples behave the same simply because the wall boundaries are playing a much bigger role now as they are too close and gravity/sedimentation effects are almost insignificant. The midplane model predicts higher values as it idealizes the hard sphere diffusivity as being confined to only the midplane of the sample chamber, when in reality

the particles are more likely close to a confining surface at these narrow confinement limits. At this point, we are convinced that the average model predictions accurately captured the confinement behaviour of the 1.06 μm PS hard spheres and further intended to perform the confinement studies for PS particles of different sizes in DI water to cover a wide range of confinement limits.

Figure 4.4 b) shows the color-coded hindrance coefficients for hard spheres (0.5μm, 1.06 μm, 2.01 μm) as a function of confinement. The average numerical model shown in the figure is size dependent and changes colors depending on the particle size it is associated with. These results further convincingly show that there is an excellent agreement between the average model predictions and experimental results within experimental errors over the entire range of wall spacing that were probed. As can be seen from the Figure 4.4 b), Brownian diffusion under strong confinement ($d/H \approx 1$) becomes more hindered and $f_{||}$ drops to 0, indicating that the walls arrest diffusion; whereas in bulk ($d/H \approx 0$), particles experience minimal hindrance and $f_{||}$ tends to 1. As stated, these particles are charge stabilized due to carboxylate-modified groups on the surface (0.0175 meq/g) and therefore it was necessary to examine additional charge effects. Hindrance coefficients were computed for different electrolyte concentrations (not shown) and it was shown that there is no significant effect of the electrostatic interactions to the hindrance as the results were overlapping for experiments in DI water, 2 mM (κ^{-1}=6.7 nm) and 10 mM NaCl (κ^{-1}=3 nm) solutions (see Appendix A). In all the confinement experiments, the total particle concentration was kept below 0.25 wt% to avoid hydrodynamic coupling among the diffusing particles.

4.7.2 Dynamics of swollen soft particles under confinement

Experiments of the hard sphere confinement substantiate our experimental procedure to measure hindrance coefficients. For our initial set of experiments, we used a non-ionic copolymer Pluronic F127 surfactant to stabilize the swelling process. For our confinement experiments, the confinement surfaces initially consisted of a microscope slide (top) and a cover slip (bottom) with silica spacers between them. Since the swollen spheres are not density-matched, they will be close to one surface or the other depending on their density. Surprisingly, we observed that the diffusivities of the drops were
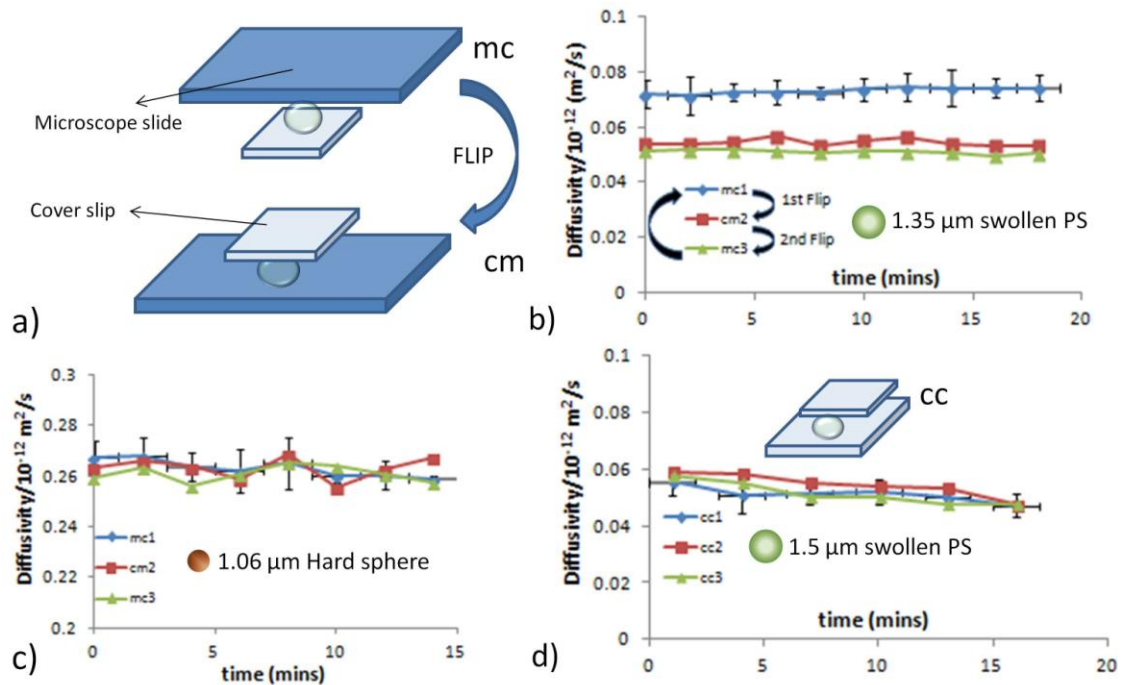
Figure 4.5 a) Schematic of the flipping experiment of swollen sphere confinement. b) Drop diffusivities are higher near the cover glass; bridging effect decreases particle diffusivities at the microscope slides. c) Hard spheres confinements are not affected by flipping. d) Surface effects were not observed for confinement of swollen spheres between two cover glasses.

considerably affected by the nearest confinement surface. To investigate into these surface effects, we did what we called "flipping experiments" where the samples were flipped to interchange the top and bottom surfaces. Clearly, we found that the diffusivities of the swollen spheres were higher near the cover glasses compared to the microscope slides. Even more surprisingly, once the diffusivities were slowed down close to microscope slides, flipping back would not make the diffusivities revert back to their original values. It is speculated there was a bridging effect between the pluronic polymer adsorbed on the swollen spheres and the microscope slide which may be responsible for these differences in diffusivity behaviour of the swollen spheres. In a few cases, we also saw aging effects where the diffusivities decreased as the particles got closer to the microscope slide surfaces as a function of time. It appears that the chemical composition of the cover glasses which are made of borosilicate glass is considerably different from the microscope slide made of sodalime glass. It is still unclear whether it is the morphology or chemical composition or the different levels of oxidation of these surfaces that is leading to these differences. The diffusivities were more consistent on the cover glasses when compared to microscope slides and these strange effects were not observed when both the confinement surfaces were cover glasses. Also, none of these effects were observed in case of hard sphere confinements as the hindered diffusivities were same on both cover glasses and microscope slides. Following experiments using an anionic surfactant SDS showed no such surface effects. However we became cautious and the subsequent confinement experiments of swollen spheres consisted of cover glasses as both the confining surfaces to avoid such dubious surface effects.

In the absence of surfactant, we observed that the swollen particles interacted strongly
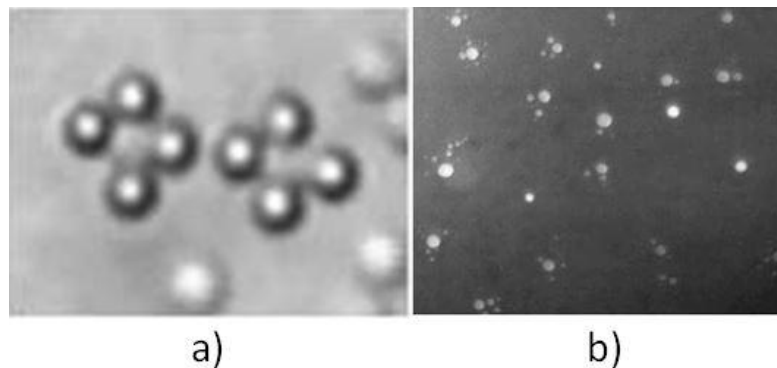
Figure 4.6 Swollen particles (without SDS) a) wrapped around the silica beads and b) interacting/wetting on glass surfaces.

with the confining glass surfaces and with the silica particles that were used as wall-spacers for confinement experiments. The exact causes of these strange particle interactions were not identified, but they were presumed to be wetting or charge-related effects. The wettability issues with the glass walls were quantified using IDL by monitoring the number density of particles sticking onto the glass surface. Also, each swollen particle was seen to collect four to six silica beads on its surface, forming free-floating assembled structures in the sample (refer to Figure 4.6). Silica beads are fairly close to glass in terms of chemical composition. Using an anionic surfactant like SDS helps because it not only stabilizes the particles against wetting; it also creates a repulsive barrier between the particles and the glass. The presence of a surfactant can stabilize the emulsion drops, however it can also strongly affect the hydrodynamic interactions [8]. We studied the confinement behaviour of all swollen particles in presence of a surfactant (5mM SDS). They reduce the interfacial tension and also prevent interfacial mass transfer due to reduced interfacial area. SDS forms a thick protective interfacial film at the drop's interface and also provides an electrostatic repulsive barrier between the drops and the

substrate [142]. Although surfactant systems were found to be much more stable and non-interacting with the confining glass surfaces, we still observed a very small population (<5%) of swollen particles tethered to the wall. The hindered diffusivities were measured for the freely diffusing un-tethered population by using a routine which identifies the stuck particles and excludes them from statistical analysis. Therefore, the diffusivities were increased very slightly (<5%) than what was actually observed in an intent to provide more meaningful diffusivity values for the swollen particles. In the case of non-surfactant systems, the number of stuck particles is very high and removing them from the statistical analysis would affect the values considerably. One of the sanity checks we performed were hard-PS confinement experiments with different SDS concentrations and found the particles to be non-interacting and the confinement behaviour to be unaffected at these low concentrations of SDS. However, for higher concentrations of SDS, the confinement dynamics were affected due to depletion interactions (See Appendix A).

During the course of the swelling mechanism, the hard PS particle changes from a rigid to a soft swollen sphere. Due to the soluble polymer in the swollen spheres, one would expect them to exhibit viscoelastic properties. At low swelling ratios, the swollen spheres should exhibit an elasticity-dominated effect and for higher swelling ratios, they should exhibit a viscosity-dominated effect. Figure 4.7 shows the hindrance coefficients for the swollen particles for various swelling ratios. The vertical color bar on the right side of the plot represents the swelling ratio and the data points are assigned colors based on their swelling ratio. It is very evident from this plot that the confinement behaviour of the swollen spheres depends on the swelling ratio (SR) of the swollen spheres. But a more careful statistical analysis shows that there exists a critical swelling ratio (CSR) above
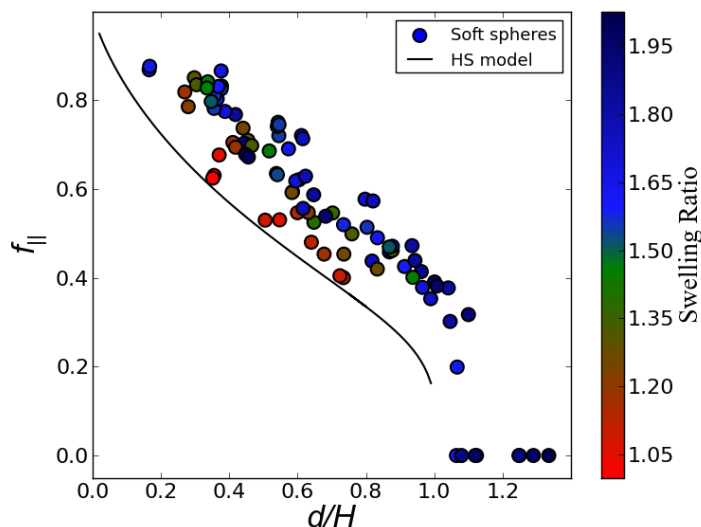
Figure 4.7 Hindrance coefficients of swollen PS particles for all swelling ratios. The color bar on the right represents the size of the swollen particles.

which the confinement behaviour was found to be independent of the swelling ratio. Figure 4.8 shows the statistical analysis for all the data points where the running average of the difference in hindrance coefficients of the soft and hard particles has been plotted as a function of the average swelling ratio. This difference increased almost linearly as the amount of swelling increased, but above a (critical) swelling ratio of 1.52, the increase as a function of swelling ratio is no longer evident implying a change in the particle behaviour. From this analysis, we hypothesize that the drop-like behaviour is achieved above this CSR. Swollen particles above this CSR are referred to as "drops" in the subsequent sections. Surprisingly, mobility of very slightly swollen particles was seen to be enhanced too relative to the hard spheres. This is expected to be an elastic effect where deformation plays a role in limiting the drag force on the particle. When a soft sphere approaches the surface, the main contribution to the hydrodynamic resistance
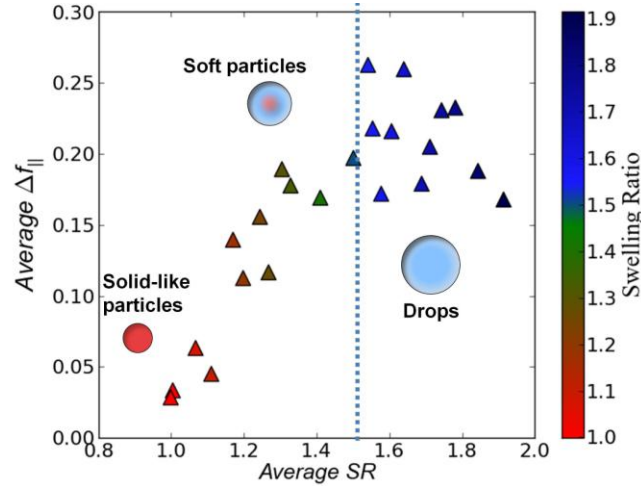
Figure 4.8 The running average $\Delta f_\parallel$ versus running average swelling ratio of the particles. The color bar indicates the swelling ratio (SR). Based on this plot, 1.52 was chosen as the critical Swelling ratio.

(energy dissipation) comes from the thin lubricating liquid film between them. As the soft sphere deforms, the thickness of this film is greater than the thickness for an equivalently sized hard sphere, thus reducing the lateral drag on the deformable particle. It has been shown by researchers that the drag on drops over the ellipsoidal range is still less compared to what would be expected for a rigid immobile sphere [141]. This was also shown by Vakarelski *et al* (2010) where they compared the drag forces on a tetradecane drop and a rigid sphere and found that the drag force on the drops are less than the rigid spheres due to the deforming interface of the drop which increases the thickness of the film between the drop and the substrate [126].

4.7.3 Dynamics of drops

Figure 4.9 shows the cleaned up version of the soft sphere data with the confinement data of just the drops. It is pretty evident from this figure that the hindered diffusivities of

drops are almost 1.5 times that of hard PS sphere diffusivity values at all the confinement values. But the most striking observation from figure 4.9 is that, these drops exhibited large diffusivities even under extreme confinements where the confinement gap is less than the unperturbed diameter of the drop. The trajectories of the drops under these extreme confinement limits are found to be very long without any tethering to the glass surface. As a matter of fact they diffuse at around 20% of their free diffusivities even under such extreme deformations. This might be a result of surfactants imparting an elastic character to liquid interfaces which can make elastic deformation easier for drops under confinement. A fluid particle in presence of a high surfactant concentration can be treated as a deformable particle of tangentially immobile surfaces which can deform easily when pressed against a solid wall. At extreme confinements, we believe that the
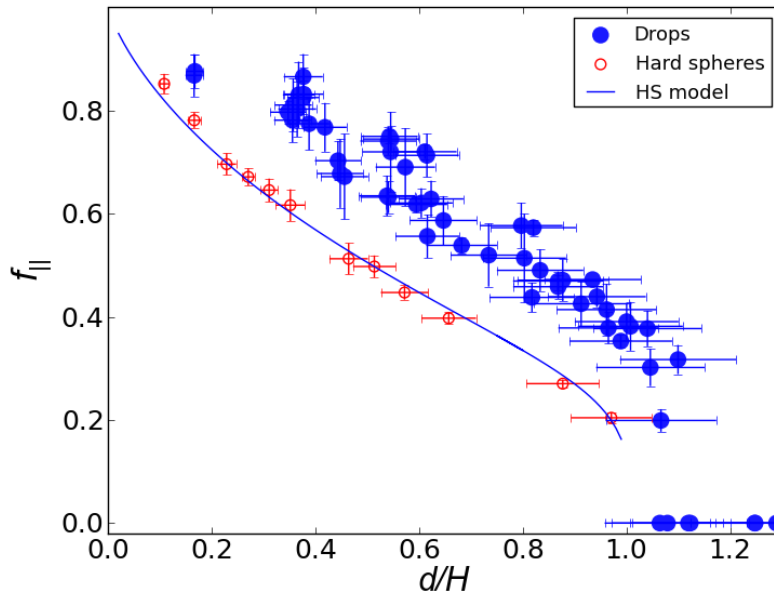
Figure 4.9 Hindrance coefficients for drops (soft particles above the critical swelling ratio) are shown in blue. The open red circles represent the hindrance coefficients for hard spheres. Clearly, drops diffuse even for *d/H* > 1 which is proof for deformation.

drops deform (flatten) under high lubrication pressure from the thin film and diffuse around because of their tendency of not wanting to wet the glass surfaces. It is expected that drop deformation will impact not just hydrodynamic interactions, but also enhance direct interactions like electrostatic repulsions and steric interactions between the drops and the surfaces which keep them further apart. This is due to the fact that all these interactions are sensitive to the specific shape of the interacting surface.[8] Even as we relax the confinement, we found the drops to behave differently from the hard particle counterpart which suggests mobility of the drop interface might have a role to play too. Despite the fact that there is no strong quantitative evidence in this regard, there seems to be a trend that for very swollen particles, the hindrance coefficients are slightly less as these particles are strongly negatively buoyant and would therefore tend to reside closer to the upper confinement surface.

Although we propose drop deformation at extreme confinement, there is no single consolidate theory on how to interpret drop deformation effects and is beyond the scope of this work. To conclude, we interpret the enhanced diffusivities of the drops are due to deformation and Interfacial mobility of the drops (further leading to internal flow). It should be noted that the absence of flow and anisotropy in the system prevents the formation of a stagnant cap which can immobilize the interface. Despite the lack of direct experimental evidence to support internal drop flow, scaling analysis of micron sized drop coalescence commonly applies a partially mobile boundary condition for empirically fitting drop collision data[143-145]. It should also be noted that to our knowledge, there is no evidence that drop diffusion occurs without mass transfer at the phase boundary for low Reynolds number systems. But the reduction in mass transfer rate

due to the presence of surfactants and other impurities has been reported by many investigators.[146]

4.7.4 Transition from softness to hardness

We further devised a control experiment to elaborate our case of the effect of the added toluene to the PS spheres. If we drive off all the toluene from the swollen particles, they should start behaving like hard spheres. By slowly evaporating the toluene from the drops, we used different drop sizes with different swelling ratios and studied the confinement dynamics using carefully picked wall spacing to show the transitions from soft sphere to hard sphere behaviour. We observed a trend where the diffusivities converge into the hard particle curve at lower swelling ratios as the confinement increased. It should be noted that this transition is due to the decreased swelling ratio and not induced due to the confinement.

In order to more clearly show the transition for swollen to hard particles, we have
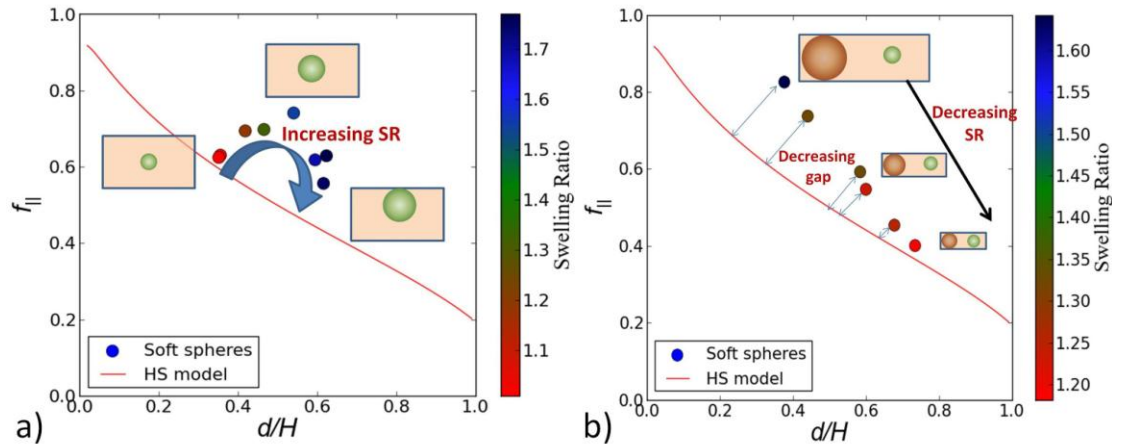
Figure 4.10 Hindrance coefficients for 'evaporating' drops using a) fixed wall spacing and b) variable wall spacings to clearly show the transition. Clearly, as toluene evaporates from the drops, hard-sphere-like behavior is observed.

adopted another experiment where we chose a fixed wall spacing and used different drop sizes (or swelling ratios) as the evaporation took place. The transition from soft sphere behaviour to the hard sphere behaviour is rather instantaneous where we see a big jump in the hindered diffusivities when we de-swell the particles with evaporation. Also, during the same experiment, we observed a subtle density effect, where a more swollen particle has a dip in the diffusivity compared to a moderately swollen particle. As explained earlier, this is a buoyancy effect. Using these control experiments, we clearly show the contrasting behaviour of swollen and non-swollen particles under confinement.

4.8 Conclusion

We have convincingly shown that hinderance for a soft sphere (drop) is considerably less than the hard spheres as the mobilities of soft spheres were clearly greater; In this investigation, polystyrene beads represents hard spheres and toluene-swollen polystyrene particles act like soft spheres. Moreover, droplet diffusivities were found to exist even when the wall spacing was less than the unperturbed drop diameter which indicates drop deformation is the dominant effect causing these anomalous effects. To the best of our knowledge, there are no previous experimental studies that reported reduced lateral hindrance for soft Brownian particles under confinement. We believe that the enhanced diffusivities of the soft spheres under confinement are due to drop deformation, interfacial mobility (which can also result in internal circulation) or a combination of both.

However, the enhanced diffusivities of soft drops even under mild confinements also raise the question whether the Stokes-Einstein equation is the correct relation to describe

the free diffusivity of these soft spheres. The Stoke-Einstein equation states that mobility is inversely proportional to the drag coefficient and the drag coefficient that is being used here meets the requirements for a non-deformable solid sphere with an immobile interface. It should be stated, however, that if the bulk drag is lower for soft spheres, we would be underestimating the size of our particles, which means that the actual confinement (d/H) would be greater, thus further enhancing the discrepancy between the hard and soft sphere hindrance behavior. It is important that we know the precise origin of the enhanced confined diffusivities of the soft spheres and this should remain the subject of future investigation. Surfactant based systems are known to have low mobility of the interface, but our experimental results suggest that they are still very different from hard sphere systems under confinement. Clearly, there seems to exist an obscure coping mechanism of viscous dissipation of energy at these drop surfaces which seems to make them more mobile than hard spheres. Although theoretical and analytical models exist for hindrance on a translating drop close to a solid interface, these models do not consider deformation effects of the drop, so we will refrain from further discussing them. However, it should be noted that both theoretical and analytical models predict reduced lateral hindrance for drops compared to solid spheres. The interfacial boundary condition of micrometer sized drops is often called into question in literature. Nevertheless, for the scaling analysis of micron sized drop coalescence, researchers have usually applied a partially mobile boundary condition in order to empirically fit the drop collision data. Many existing coalescence models assume partially mobile boundary conditions and successfully fit their data for micron-sized drops [145, 147-151]. Nevertheless, direct experimental evidence would put these uncertainties to rest. Particle or solute tracers

114

within drops offer a possible method to provide direct experimental evidence of internal drop flow [152]. The work presented in this chapter has shown that surfactant covered swollen spheres exhibit considerably higher diffusivities than hard spheres under all confinements. Moreover, diffuse even under deformation-induced super confinement limits where hard spheres are completely immobile. Results presented in this work caution against these assumptions such as nondeformability or interfacial immobility in micrometer sized surfactant droplets.

Chapter 5

Hydrodynamic interactions of core/shell microgels

in confined systems

5.1 Introduction

The term "microgel" was first used in a 1949 publication entitled "Microgel, a new macromolecule" by Baker to describe cross-linked polybutadiene latex particles [153]. Microgels can be defined as a colloidal dispersion of gel particles composed of a solvent-swollen cross-linked (chemically or physically) polymer networks. Similar to hairy particles, microgels are considered as soft particles in the perspective that they can adjust both their shape and volume in response to external stimuli like pressure, flow, pH, and temperature because of their variable properties [154]. They share a common attribute of deformability with emulsions; the property that sets them apart from emulsions is that microgels can be compressed due to their porous nature, while emulsions are generally treated as incompressible. The modulus (softness) of microgels depends on many parameters like the cross-link density, co-monomer concentration, solvent quality, presence of ions, and the network architecture [118]. The cross-linker concentration especially has a significant impact on the cross-linking density of microgels; it strongly affects their Young's moduli and swelling ratios. In this chapter, we are interested in distinguishing the confinement dynamics of microgels from their hard sphere counterparts, with the ultimate goal to determine the most important factors that play a role in their confinement dynamics.

116

In order to differentiate between soft and hard spheres, Vlassopoulos *et al*. collected data from various publications and replotted them in a generic compounded plot of the zero-shear viscosity (normalized by the solvent viscosity) as a function of the effective hydrodynamic volume fraction [118]. This plot reveals the role softness plays in reducing the relative viscosity and increasing the effective maximum packing fraction. It was clearly shown in the plot that the soft colloidal systems in the larger volume fraction regime were able to pack considerably higher volumes for the same relative viscosity as the hard sphere systems. However, in the lower volume fraction regime, the scaled viscosity behavior for all particles (hard & soft) collapsed to well-known Einstein–Sutherland and Batchelor curves [155]. This indicates that softness in these colloidal systems comes into play in the presence of particle-particle interactions (high volume fraction regime) where deformation and/or compression of the particle is common.

Likewise, another important phenomenon where softness can play an influential role is particle-wall hydrodynamic interactions [156]. For example, In a recent study, silica particles near a planar silica surface covered with thermally responsive polymer brushes showed significantly reduced hydrodynamic coupling in comparison with numerical predictions for hard walls [157]. Also, it was shown that soft nanoparticles result in significantly increased lubrication behaviour compared to hard nanoparticles pertaining nanolubrication research [42]. These experimental observations indicate that softness may be able to alter hydrodynamic interactions, but raises questions regarding the hindered diffusion of soft spheres under strong confinement between solid walls. Unlike hard particles, microgels are known to exhibit very low static friction at interfaces, which explains their wall-slip in the rheological measurements [158]. While the influence of

particle softness on the rheology of the microgels is well researched [159, 160], their confinement dynamics for small Peclet numbers (Pe << 1) have not been explored, to the best of our knowledge. Most of the research on the microgel wall hydrodynamics was performed on the wall-slip behavior under shear (Pe >> 1) [161-163] where a noncontact elastohydrodynamic lubrication slip model was used to explain their wall-slip as a result of asymmetric deformation and lubrication film coupling [162]. Therefore, it is evident that the softness of these systems matters when they are sheared with surfaces at Pe >>1, when shear leads to deformation in the microgel dispersions. However, for Pe << 1, Brownian forces dominate, and the particle behavior is determined by diffusional relaxation, where the Brownian forces try to restore the equilibrium structure of the microgel dispersions. Therefore, it is very interesting to see if the microgel particles exhibit reduced hindrance due to their associated softness, under confinements in the low Peclet number regime. It should be noted that the softness of these particles has two aspects: deformability and compressibility/porosity. Porosity means that the lubricating fluid film between the microgel and the confining wall can partially flow through the interior of the particle, thus reducing the hydrodynamic coupling between the particle and the wall. However, the fluid passing through the porous network can also exert viscous drag forces on this network [164]. Therefore, it is possible that the confinement dynamics in these systems can be affected by a great degree by their porous nature alone, if not the deformable nature which is usually dominant for high Peclet numbers.

A fundamental question we are trying to answer in this work is "Do microgels behave differently from emulsions and hard sphere systems under confinement?" Based on the elasticity of colloidal particles, they can be rank-ordered in terms of softness as follows

118

[118]: polymeric coils > star polymers > microgels > emulsions > hard spheres. Whether this order of elasticity directs the hydrodynamic drag forces of microgels under confinement is an important question. If elasticity is not the relevant softness parameter for microgels, how does one define softness for microgels? Is porosity the applicable softness parameter for microgels? Another question relevant to the microgel systems which interests us the most is, "How are the confinement dynamics affected by various parameters of interest of microgels?" For example, the cross-linker concentration in the microgel structure strongly affects the microgel properties [165, 166] associated with softness, for example swelling behavior and porosity. Whether this has an impact on the confinement dynamics of microgels is our main interest in this study. Similarly, we are interested in exploring the confinement dynamics as a function of several other factors that can influence the microgel properties: shell thickness (for the case of core/shell microgels), cross-linker concentration, pH, temperature. For example, by increasing the temperature above the LCST of the microgels we can increase the stiffness of the microgels due to the expulsion of the solvent, which also leads to shrinkage. Therefore, by increasing the temperature, the properties of the microgels change from soft-sphere-like to hard-sphere-like. If microgels have distinctly different confinement dynamics compared to hard spheres, the role these factors play in governing their confinement dynamics is intriguing. For this thesis, we have selected multi-responsive core-shell microgels with a polystyrene core and pNIPAm-co-AAc shell, with the objective to provide meaningful insight in the confinement properties of these soft microgels.

5.2 pNIPAm-based microgels

Poly(N-isopropylacrylamide) (pNIPAm)-based microgels have emerged as potentially useful model soft spheres and are the most investigated microgels in the last decade due to their very significant biological applications such as controlled and self-regulated drug delivery [167, 168], biosensing [169], bio-conjugation [170], tissue engineering [171], bio-separation [172] and other practical applications like emulsion stabilization [173], microcontainers and switchable microlens preparation [174]. We chose pNIPAm systems mainly because of their ease of handling and extensive literature available on their preparation and properties. Colloidal pNIPAm microgels undergo an entropically favored volume phase transition (VPT) at the lower critical solution temperature (LCST) of 32 °C. While pNIPAm is in a swollen state (due to hydration) below the LCST, heating changes the solvent quality of water from good to poor, resulting in the expulsion of water molecules from the polymer network, which renders pNIPAm microgels temperature-responsive. One can introduce additional functionality to the polymer network by copolymerizing NIPAm with other monomers, for example styrene, methyl methacrylate, or acrylic acid. However, the incorporation of ionizable groups into the pNIPAm microgel network can add significant complexities to the system, due to changes in the internal network structure. For example, researchers have shown that functionalized microgel suspensions can crystallize at amazingly low concentrations at which pure pNIPAm microgels remain fluidized [175].

Among these systems, one well-studied microgel is poly-N-isopropylacrylamide copolymerized with acrylic acid (pNIPAm-co-AAc). These microgels use the temperature responsiveness of pNIPAm combined with the pH sensitivity of acrylic acid

to create a dually responsive material [176]. As stated above, incorporation of acrylic acid can considerably change the properties of microgels. For example, pNIPAm-co-AAc microgels still undergo a VPT due to the presence of NIPAm, but they now undergo this transition at elevated temperatures [177]. Addition of ionizable AAc groups provides not only pH-responsiveness due to electrostatic repulsion between deprotonated acid groups and osmotic pressure of counterions, but also responsiveness to ionic strength because of counterion screening. Therefore, it is recommended to use buffer stabilization to maintain a constant ionic strength while working with these microgels. Below the pK_a of acrylic acid ($pK_a = 4.25$), the acidic entities are protonated, resulting in a behavior analogous to that of pure pNIPAm microgels. Above the pK_a, the acid entities are fully charged due to deprotonation and a pH induced volume transition will occur due to electrostatic repulsion between the charged groups and added osmotic pressure from the counterions [178].

In this chapter, core/shell (C/S) (PS/pNIPAm-co-AAc) microgels were used as model microgel systems because of the need for accurate microcsopic imaging, as will be explained in more detail later in this chapter. Keeping in mind that the softness attributes (deformability, porosity) of microgels are different with respect to certain characteristic parameters like the cross-linker concentration, shell thickness and co-monomer content, we investigate the effect of these parameters on the confinement dynamics of core/shell (PS/pNIPAm-co-AAc) microgels.

5.3 Synthesis and characterization of core/shell microgels

An individual pNIPAm-co-AAC microgel particle can be tracked with optical microscopy in differential interference contrast (DIC) mode, but the optical contrast is low, which affects the ability to precisely track the positions of multiple microgel particles simultaneously [179], which is an important in measuring their diffusivity. To overcome this challenge, we synthesized core/shell (C/S) microgel particles with a fluorescent polystyrene (PS) core and pNIPAm-co-AAc shell. The C/S colloidal microgels were synthesized via standardized aqueous precipitation polymerization reaction as reported previously [180, 181] with minor changes in the protocol. Before we continue with this discussion, it should be noted that the synthesis of C/S microgels is always accompanied by growth of pure pNIPAm microgel spheres in the reaction mixture. However, these pure pNIPAm microgels can be easily removed using a few centrifugation/redispersion cycles because of the high density contrast between the C/S microgels and pure microgels.

We used fluorescently labeled carboxylate modified polystyrene (PS) microspheres (FluoSphere®, 0.50 µm diameter, Invitrogen) as seeds and produced a layer
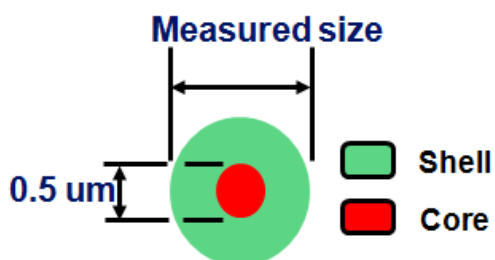
Figure 5.1 Schematic of the core-shell particles.

of pNIPAm-co-AAc microgel as an outer shell. The monomer NIPAm was purified by recrystallization from hexane before use. All the materials were purchased from Sigma-Aldrich unless otherwise noted. The comonomer (acrylic acid (AAc)), cross-linker (N,N'-methylene bis(acrylamide) (BIS)), surfactant (Sodium dodecyl sulphate (SDS)) and initiator (ammonium persulfate (APS)) were all used as received. All the water used in the experiments was deionized before use. In a typical synthesis, after weighing the appropriate amounts of NIPAm, BIS and SDS, the reactants were introduced into 30 mL DI water containing 0.033 wt% purified microspheres. The reaction mixture with the microsphere suspension was dissolved using a slow-roller for 10-15 minutes after which it was pre-heated to 60 ºC and purged with N_2, followed by adding the APS and AAc after 30 minutes, thus initiating the reaction. 5-10 minutes after initiator insertion, the reaction mixture turned turbid, indicating successful initiation. The reaction was performed at 60 ºC for 4 hours while stirring at 400 rpm and being purged by N_2 gas, in a three-neck round bottom flask. The synthesized C/S microgels were first centrifuged/redispersed (30 minutes @ 7300 rpm) to remove the population of pure pNIPAm microgels and then purified extensively by dialysis against DI water over a week to remove the contaminants and unreacted components of the reaction mixture. A fixed concentration of 2 mM was used for SDS for all the microgels prepared in this chapter. Although many researchers reported that SDS influences microgel particle nucleation and thus its final size [182, 183], it was also reported that presence of low SDS concentrations not only imparted additional stability but also gave robust microgel preparations [183]. Also, a fixed proportion of acrylic acid was used (14 mol %). The

number-averaged polydispersity of all the C/S microgels prepared in this chapter was determined to be less than 13 %.

Although microgel particles are generally not hard spheres, it is common practice to determine the size of submicron microgel particles using the Stokes-Einstein equation [164]. The hydrodynamic radius R_H of the C/S microgels was characterized using PTVM methods. We used PTVM instead of Dynamic light scattering (DLS) to determine R_H, because the latter is highly sensitive to the presence of impurities, small aggregates, and pure pNIPAm microgels formed as a result of side reactions. All these species can be easily ignored using fluorescence microscopy coupled with PVTM, during the image analysis step using specific filters. As we will see in the following sections, we also performed the size measurements for the swelling/deswelling dynamics of these microgels induced by both temperature and pH changes. A typical size measurement experiment using PTVM takes place through the following steps. First, the fluorescent C/S pNIPAm-co-AAc microgel particles were first suspended in a buffer solution with low ionic strength (I=20 mM). Diluted microgel suspensions were then placed between a microscope slide and cover slip with parafilm spacers of about 100 μm thickness. An optical video microscope (Leica DM-IRB) with 63x objective lens was used and the

	Size (μm)	NIPAm	BIS	AAc	SDS	APS
a1	1.20 μm	74.5%	4.48%	14%	2 mM	15 mg
a2	0.94 μm	74.5%	4.48%	14%	2 mM	15 mg
b1	1.17 μm	76.2%	2.3%	14%	2 mM	15 mg
c1	1.28 μm	70.1%	8.1%	14%	2 mM	15 mg

Table 5.1 Various C/S microgel particles synthesized and used in this chapter.

movies of 1500 frames were recorded for each sample with a CCD camera (Cohu, Poway, CA; 30 frame/s, 640 × 486 pixels) and analyzed. For the case of size versus temperature measurements, the optical video microscope was used in combination with Peltier-controlled thermal microscope stage (PE100-LI2, Linkam Scientific Instruments Ltd.) and objective heater (PN150819, Bioptechs, Inc.).

5.4 Effect of shell thickness

In this section, the swelling properties and the confinement dynamics of C/S microgels with varying shell thickness and a constant core are investigated as a function of shell thickness. The pNIPAm shell thickness variation on polystyrene cores has been previously studied in polymeric systems to study fundamental swelling and rheological properties of environmentally responsive polymers [184, 185]. Cheng *et al.* used C/S (polystyrene/pNIPAm) to show that shear thickening behavior was non-existent for microgels with large shell thickness, but existed for relatively harder counterparts with thinner shells [186]. Keeping in mind that shear thickening behavior is strongly influenced by a delicate balance between hydrodynamic interactions, Brownian motion and inter-particle interactions [187], we investigate the confinement hydrodynamics as a function of shell thickness. Assuming that the thickness of the shell is directly related to the C/S microgel softness, we question if such form of softness from the shell thickness parameter influences the hydrodynamic drag of the microgels under confinement.

For our experiments, the thickness of the pNIPAm-co-AAc shell is controlled by varying the amount of monomer added during the precipitation polymerization reaction keeping a fixed ratio of the pNIPAm monomer and BIS cross-linker. As shown in the

Table 5.1, particle size increases with increased monomer concentration, providing us with proof of increased shell thickness. The number-averaged polydispersities for both the samples were less than 14%. Although, we associate the shell thickness parameter of the C/S microgels with softness, it is not a trivial task to precisely quantify these intrinsic properties of these microgels. For the purpose of this study, a useful shell thickness parameter (S) has been defined for core-shell particle softness: $S = T_s/(T_s + R_c)$, where T_s is the shell thickness and R_c is the core radius. This parameter is particularly useful when the composition of the microgels remains the same while the shell thickness varies. We first determined the swelling characteristics of the C/S microgels as a function of pH and temperature in the bulk of the samples. The hydrodynamic radius R_H of the C/S microgels as a function of pH and temperature was characterized using PTVM methods. A normalized radius R_N is defined for these systems to compare the change in shell thickness for various responses:
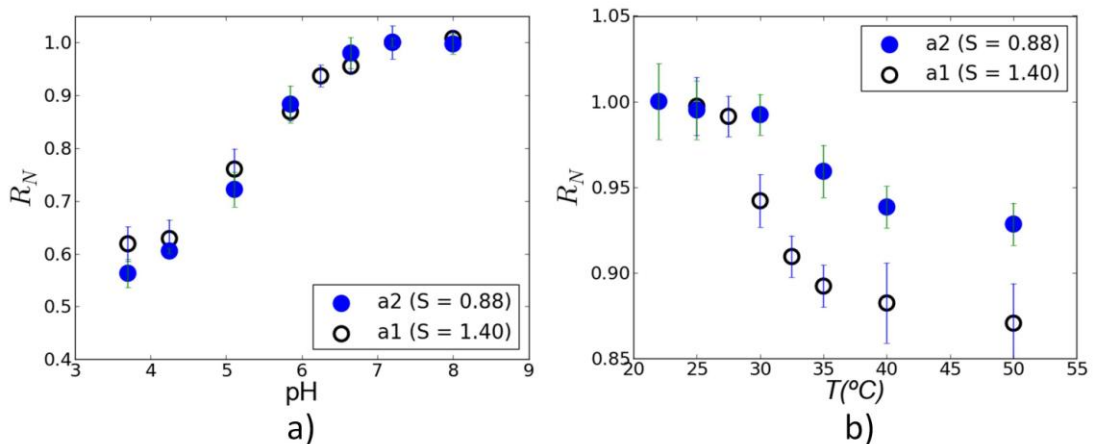
Figure 5.2 Normalized radii, R_N, as a function of a) pH and b) Temperature for microgels with different shell thickness parameters. The swelling/deswelling characteristics are similar for pH changes but differ for temperature changes.

$$R_N = \frac{R_H - R_c}{R_{H,0} - R_c} \tag{5.1}$$

where $R_{H,0}$ is the radius of the C/S microgel at standardized conditions (T = 22 °C, pH = 7.2) for pH induced changes. It was observed that the C/S microgels exhibit temperature and pH responsive properties similar to the pure pNIPAm-co-AAc microgels. For the temperature measurements, the particles were dispersed in a stable phosphate buffer (pH = 7.2, I = 20 mM). For the pH measurements, the C/S pNIPAm-co-AAc microgel particles were suspended in various buffer solutions with pH values ranging from 3.0 to 8.0 and constant ionic strength (I = 20 mM). Prior to each measurement, the sample was allowed to equilibrate at the reported pH or temperature for approximately 10 minutes. The temperature induced VPT and pH induced VPT processes of these microgels are shown in Figure 5.2. While the pH induced VPT transition of a1 and a2 suggests similar behavior, the temperature induced VPT transition for these
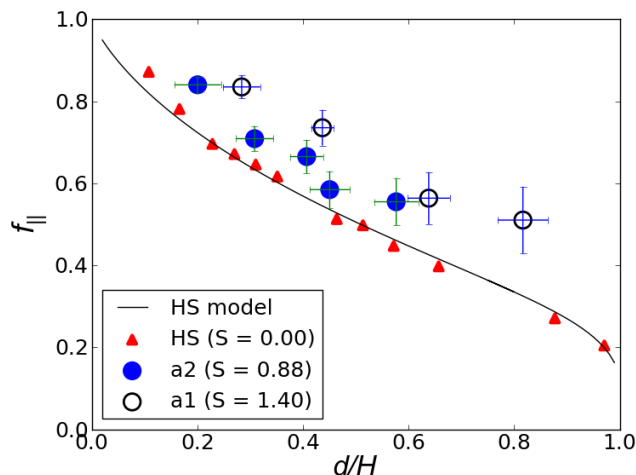
Figure 5.3 Hindrance coefficients for core-shell microgels in a buffer medium for two different shell thicknesses (legend indicates shell thickness parameter S). The data points in red represent the hard sphere coefficients in DI water.

127

particles differed significantly with a1 showing higher temperature-responsiveness, suggesting that the particle with greater shell thickness has higher flexibility associated under temperature changes. It is not completely clear why the thermal response and the pH response were not in agreement. A reasonable assumption is that while surface charge effects and electrostatics are being affected during the pH change, such charge related effects are not associated with thermal changes. To further analyze these differences, we proceeded to investigate the confinement dynamics of these microgels as opposed to the unbounded (bulk) behavior shown above.

The experimental setup and protocol was exactly the same as the confinement experiments for hard spheres and emulsions in Chapter 4. A drop of the suspension was placed between two glass coverslips, excess fluid was removed to reduce the spacing between the slides, and the cell was sealed with vacuum grease. To prevent adhesion between the C/S particles and the coverslips, the coverslips were placed inside plasma cleaner for 10 minutes to create a repulsive barrier between the charged microgels and surfaces. Several researchers observed sticky behavior of pNIPAm based microgels [179, 188] and often used surface treatments as a solution [188].

The confinement experiments for microgels were always done in a pH controlled phosphate buffer medium (pH = 7.2) with a fixed ionic strength (I = 20 mM) where the particles were deprotonated and significantly charged. Similar to the hard spheres, the hindrance coefficient for soft core/shell particles decays with increasing degrees of confinement. However, the soft core/shell spheres diffuse considerably faster than their hard sphere equivalents for all confinement conditions. We believe that the porous structure of the microgel shell allows water to penetrate, thus reducing the hydrodynamic

coupling between the sphere and wall. We performed confinement studies on microgels with two different values for *S*, 0.88 and 1.40 respectively. Figure 5.3 shows the measured hindrance diffusivities for both these microgels plotted in comparison to hard sphere confinement data. From this plot, it is clear that the shell thickness has a considerable impact on the hindrance coefficients of soft core-shell microgels under confinement, as diffusivities increased with an increase in shell thickness, thus increasing the porosity of the C/S microgels. As a result, more solvent can penetrate into the microgel structure, reducing the hydrodynamic coupling between the particle and the confining walls. However, from this investigation, one can still not deduce if it is the deformable nature or the permeable nature of the C/S microgels that causes this distinctive behavior from the hard particle counterparts, since (anisotropic) shrinkage of the microgels due to wall effects could lead to similar observations.

5.5 Effect of cross-linker concentration

In this section, the effect of the amount of cross-linker in core/shell (PS/pNIPAm-co-AAc) microgel particles on their swelling behavior and their confinement dynamics are studied. It was demonstrated by many researchers that the amount of cross-linker content strongly affects the microgel properties [165, 189]. For example, it was shown that the swelling ratio of microgels with higher cross-linker content is smaller than that of lower cross-linked microgels [165, 166, 189, 190]. Therefore, increasing the cross-linker concentration increases the particle stiffness (Young's modulus) and transforms the microgels from soft to hard. The cross-linker is also widely known to modify the internal structure of microgels, because a higher cross-linker content can often result in a heterogeneous core-shell-like structure within the microgel layer: a stiff interior core with

129
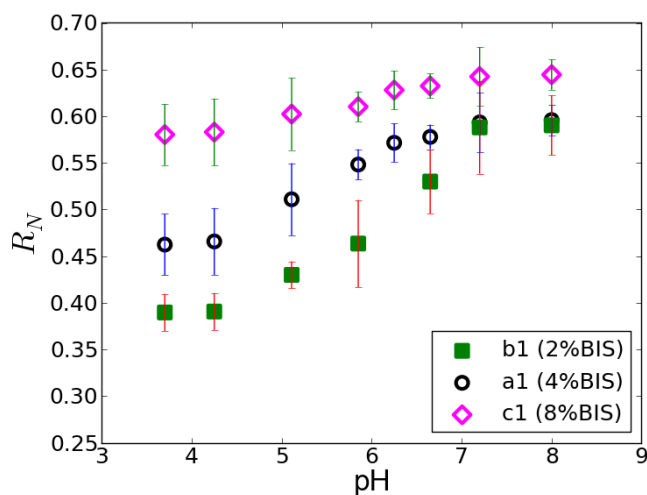
Figure 5.4 Normalized radii, R_N, as a function of pH for microgels with different cross-linking densities.

high cross-linker density and a looser peripheral shell with lower cross-linker density [166]. This is attributed to the cross-linker (BIS) monomer having a higher polymerization rate compared to the NIPAm monomer, which leads to a cross-linker density gradient in the radial direction of the shell structure. This heterogeneity can significantly influence the structural and mechanical properties of the particle like swelling dynamics, deformability, and porosity. Considering this phenomenon, addition of more cross-linker should not only increase the volume-averaged overall stiffness of these microgels, but it should also increase the stiffness of the outer periphery of the shell. This is because the radial cross-linker density gradient decreases with increasing concentration) assuming the polymerization rates of the cross-linker and monomer do not change. Also, many authors have reported that an increase in cross-linking density of pNIPAm microgels leads to a decrease in the microgel porosity due to relatively denser cross-linking [191, 192]. However, since the cross-linking distribution is radial, it is expected that the pore size increases from the core towards the periphery of the microgel

130

[193]. Based on this information, we propose the hypothesis that a higher cross-linker concentration leads to increased hindrance under confinement due to the physical stiffness and decreased porosity caused by denser cross-linking.

We will first discuss the dynamic swelling characteristics of the core/shell (PS/pNIPAm-co-AAc) microgels as a function of cross-linker content induced by the pH change. We speculate that these pH induced changes will help us make a prognosis for the stiffness or softness characteristics of the particles for the various cross-linker concentrations that were used. We compared the swelling dynamics for three different cross-linker concentrations namely 2%, 4% and 8% molar concentrations. It should be noted that we used the same microgels from the previous section with the larger shell thickness (a1) as our sample for the 4% BIS concentration. As one can see from Figure 5.4, the swelling characteristics change significantly with change in cross-linker
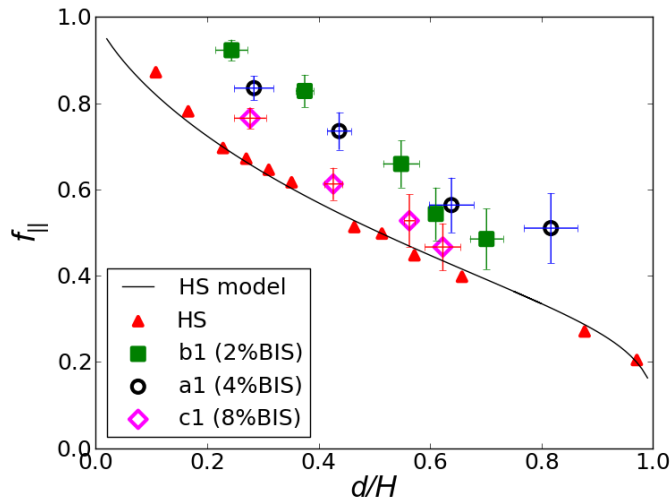
Figure 5.5 Hindrance coefficients for C/S microgels in a buffer medium for three different cross-linker concentrations compared to hard sphere confinements. Large deviations are seen for particles with 8% BIS as they behave more like hard-spheres.

concentration: the swelling ratios of the 2%, 4% and 8% microgels are 1.51, 1.28 and 1.1, respectively. Evidently, for 8% cross-linker concentration, the size variations with pH are not as large as those observed for 2% and 4% concentrations, indicating that the cross-linking restricts the swelling ability.

The confinement experiments for these microgels were done in a phosphate buffer medium with constant ionic strengths. It is important that the ionic strength of the buffer remains low and constant as it can significantly affect the properties of these microgels due to charge effects [194]. Figure 5.5 demonstrates that the hindrance of the C/S microgels under confinement increases with increase in cross-linker concentration. For mild confinements, as the cross-linker concentration increases, we see a gradual shift towards the hard particle diffusivity data, but the same cannot be said for higher confinement limits. As a matter of fact, the hindrance coefficients of 4% and 2% cross-linked particles are not very different for higher confinement limits (above 0.6). Under mild confinements, the plot can be interpreted as showing a slight trend in their behavior. But for higher confinements (above 0.6), it can be translated from the plot that the 4% crosslined particles have higher diffusivities than 2%, contradicting our hypothesis. However, the hindrance coefficients of highly cross-linked particles (8%) show a dramatic decrease shifting their behavior much closer to the hard particle behavior. From these observations, it is reasonable to assume that there may exist a threshold cross-linker concentration at which the microgels behave very much like hard spheres under confinements for the purpose of hydrodynamic wall drag. The conflicting results obtained at higher confinements might be due to surface interactions where the microgels get too close to the surface causing adherence.

5.6 Effect of pH and temperature

These functionalized microgel particles allow examination of volume changes isothermally, as well as a function of pH. Thus, it would be interesting to see if the path taken by a particle (temperature or pH changes) to reach a certain swelling ratio, influences its confinement dynamics. But first, we investigated their behavior as a function of temperature and pH separately to see how these parameters impact the confinement dynamics. It should also be noted that due to their enhanced charge stabilization, these microgels do not flocculate even at temperatures above the VPT. However, it was observed that the particles tend to adhere to the glass walls at lower pH values due to protonation which eventually leads to charge reduction.

In the vicinity of the LCST, the particle diameter starts to decrease as the shell shrinks, because of the lower solubility of pNIPAm in water, which leads to the expulsion of
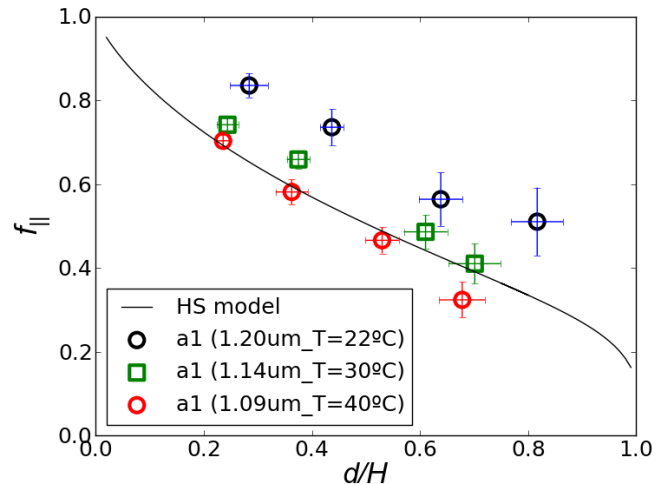
Figure 5.6 Hindrance coefficients for sample a1 as a function of temperature. Hindrance gradually increased as the temperature increased from 22 ℃ to 40 ℃.

water and compression of the porous network which eventually leads to decreased porosity. We used three different temperatures to investigate the confinement dynamics of a1 microgel sample. As expected, the hindrance coefficients decreased with increasing temperature values. However, it was observed that there was a considerable step-down in the values of the hindrance coefficients for even a slight decrease in particle diameter. As one can see from Figure 5.6, the hindrance coefficients decreased drastically as the particle diameter changed from 1.2 µm to 1.09 µm. In fact, the microgel particles start behaving like their hard sphere counterparts inspite of the presence of compressed shell layer on the polystyrene core. Also, these hindrance diffusivities values are much lower when compared to the b1 microgels whose shell thickness is greater than that of the a1 microgels at $T = 40$ ℃. Therefore, for a fixed shell thickness, particles with higher porosities clearly show smaller hindrance. For $T = 40$ ℃, it was observed that the diffusivities were less than the hard sphere values at high confinement limits. This is
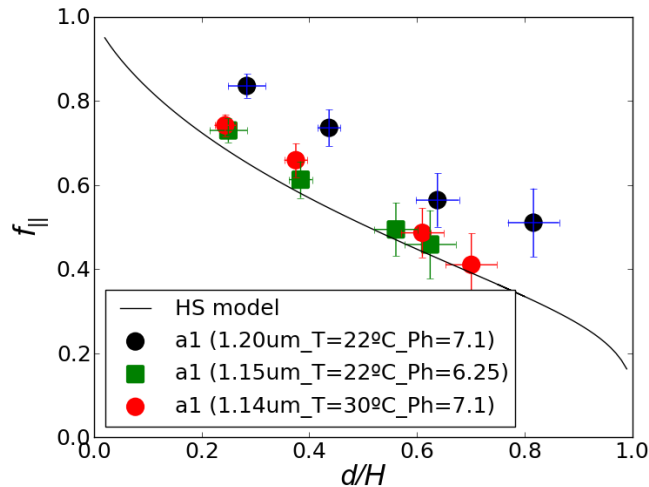
Figure 5.7 Hindrance coefficients for a1 for different conditions. Green squares represents the standardized conditions (T=22 ℃, pH 7.1), red diamonds corresponds to pH 6.25 at 22 ℃ and the blue circles corresponds to T=30 ℃, pH 7.1.

again expected to be a result of surface adhesion effects at close confinements.

Similarly, for smaller pH values, the acidic entities are protonated and the electrostatic repulsions and the osmotic pressure inside the porous structure decreases leading to shell shrinkage and a decrease in porosity. For confinement dynamics of these microgels at lower pH values, we saw increased hindrance as a result of decreased porosity. This can be seen in Figure 5.7 where a change in pH from 7.1 (black) to 6.25 (green) resulted in a size change from 1.2 μm to 1.15 μm which also resulted in increased hindrance under confinement. To compare the temperature and pH effects, we deswelled the microgel sample a1 using these two different routes and chose the pH, temperature values carefully to get to the same diameter and investigated the confinement dynamics at this shrunken size separately (see Figure 5.7). For these two experimental conditions, the like-sized shrunken particles behaved very much alike for all confinement limits explored. In conclusion, the confinement dynamics is independent of the path taken by the microgel particles in order to reach a certain swollen/de-swollen state. This is most likely due to the porosity parameter taking control of the confinement dynamics which should remain the same for a particular swollen/de-swollen state of the particle.

5.7 Conclusion

Our study is the first direct observation of hindered Brownian diffusion of C/S microgel spheres between parallel walls over a moderate range of confinement levels. It was observed that soft C/S microgels, which are porous, compressible and deformable can dissipate hydrodynamic coupling effectively, resulting in enhanced mobility under confinement. Clearly, the behavior of soft C/S microgels cannot be explained with

current numerical predictions for hard spheres and therefore will require further advancements with regards to modeling. In this chapter, only mild confinement limits of microgels were explored to avoid strong particle-surface interactions. It would be interesting to investigate the confinement dynamics of the C/S microgels in the "super-confined" regime where particle deformation is necessary, because the unperturbed microgel diameter is greater than the wall spacing. For our systems, when the wall spacing was decreased past a confinement value (≈0.95), the core/shell particles slowed down and eventually became fully arrested. We suspect this behavior was caused by adhesion between the microgels and glass substrates. Surface modifications of the glass to negate such interactions would certainly help us research this problem. Apart from the parameters that were studied here as having an effect on confinement behavior, other parameters of interest are co-monomer (AAc) concentration, ionic strength, and surface charge density. For example, microgels are known to swell more as the concentration of AAc increases. Also, the confinement dynamics of pure microgels without the hard core might be of interest due to their greater practical implications.

To summarize our work, we have determined that shell thickness, cross-linker concentration, pH and temperature can significantly affect the confinement dynamics of the C/S (PS/pNIPAm-co-AAc) microgels. A higher shell thickness resulted in higher confinement diffusivities most likely due to increased penetration of the surrounding solvent reducing the hydrocoupling between the microgels and the wall structures. However, the swelling dynamics of the microgels with different shell thicknesses were obtained for pH and temperature changes and it was determined that the behavior was not consistent for unknown reasons. While the temperature induced size variation hinted that

greater shell thickness resulted in a higher swelling ratio, pH incuded size variation resulted in identical swelling ratios for different shell thicknesses. It is reasonable to expect that the effect of shell thickness become unimportant at large shell thicknesses. However, we do not have proof for this
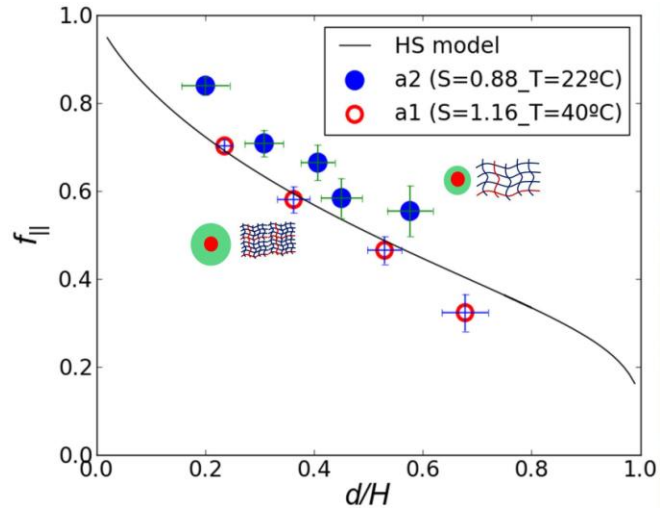
Figure 5.8 Hindrance coefficients for a2 under standardized conditions (T=22 ℃, pH 7.1), and a1 at T=40 ℃, pH 7.1.

argument as we were unable to synthesize particles above a certain shell thickness limit. Also, cross-linker concentration has a significant impact especially at higher cross-linking densities. At higher cross-linker concentrations, hard-sphere-like behavior is approached due to decreased porosity and increased stiffness. However, at lower cross-linker concentrations, the confinement behavior is not very dissimilar indicating that a further decrease in the cross-linker concentrations would not produce vast differences in confinement behavior. It was also shown that a small decrease in particle size as a result of pH or temperature change resulted in a big step-down of the confinement diffusivities indicating porosity is an important element for the confinement hydrodynamics. Figure 5.8 shows hindrance coefficients for a2 at standard conditions and a1 at an elevated temperature (40 ℃). Clearly, a2 with a smaller shell thickness parameter (but more porosity) has higher hindrance diffusivities compared to a1 with a larger shell thickness under shrunken state (lower porosity). Evidently, this suggests that porosity is perhaps a

137

more important criterion than shell thickness for the particle sizes considered here. Also, it was shown that the confinement dynamics is independent of the path taken (temperature/pH) by the microgel particles in order to reach a certain swollen/de-swollen state.

From this chapter, we have found strong evidence in support of the hypothesis that porosity is most important for reducing the hydrodynamic hindrance of microgels. Also, from Chapter 4 we have concluded that deformability and internal flow (caused by interfacial flow) can greatly reduce hindrance under confinement for soft sphere systems. The question then arises "which of these factors are more important for soft sphere systems to reduce their hydrodynamic hindrance under confinement?" If we compare the data for both these soft sphere systems (from Chapters 4 & 5) on the same scale, it can be seen that in our (limited) set of experiments the effects of porosity in microgels never exceeds the magnitude of the effects of internal flow (and deformability) in the swollen sphere systems. This suggests that flow circulation is more important than having flow through the porous structure of the microgels. However, it must be noted that the porosity effect has not been maximized, because lower cross-linker densities (<2 % BIS) were not explored due to challenges with the synthesis of such particles. At the same time, similar arguments can be made for our experiments with toluene-swollen PS spheres, since there is still a fairly significant amount of polymer present inside the drops, which can cause viscoelasticity, and surfactant, which can also suppress internal flow in these systems. Therefore, to fully answer the question posed here, one would need additional experiments to study the behavior of conventional non-viscoelastic drops without surfactant, and microgel particles with lower cross-linker concentration and smaller cores

in order to eliminate potential core effects. In conclusion, soft swollen spheres and C/S microgels show a very different confinement behavior compared to the hard sphere counterparts and will need further investigations both numerically and experimentally to understand their behavior in further detail.

Chapter 6

Conclusions and recommendations

6.1 Conclusions

In this thesis, findings are presented on the non-bulk dynamics of colloids close to surfaces, as a result of depletion interactions and hydrodynamics interactions. While we focused on hard colloidal systems for the studies pertaining to depletion interactions, we explored the differences between the hard and soft colloids behavior in the work associated with hydrodynamic interactions.

Chapter 1 gives a general introduction to the subjects of this thesis, in particular the various kinds of interactions that play a role in colloidal systems, differences in the hard and soft sphere systems with regards to hydrodynamics, characterization techniques used in the projects and finally the structure and motivation that resulted in this research topic.

Chapter 2 introduces the background about the depletion interactions and also introduces analytical solutions that exist in literature for the interaction potential in basic geometries, such as the generalized Asakura-Oosawa model for sphere-sphere interactions. Numerical modeling was developed to calculate depletion interaction strengths for simple geometries like sphere-sphere, sphere-wall, and sphere-edge geometries to provide guidance with regards to the identification of the appropriate range of parameters for experiments (reported in the next chapter). For more complex contact geometries, such as diameter-modulated nanowires, interaction strengths were calculated

numerically by utilizing the axial symmetry of these objects. We were able to identify the model parameters that have a significant impact on their interaction strength. For example, we computed the interaction potentials for interlocking dumbbell-dumbbell geometries and parallel cylinder-cylinder geometries as a function of the overlap length and depletant polymer size. We found that both these parameters play a significant role in making the dumbbell-dumbbell interactions highly selective over cylinder-cylinder interactions. By comparing the overlap volume of the two geometry overlaps, we were able to show that a smaller depletant size and a small length of overlap (below a certain critical length) favors the dumbbell-dumbbell interactions while the higher values for the same would favor the cylinder-cylinder overlap. In conclusion, it can be said that the model provides us with a versatile way of calculating depletion interaction strengths between geometries of different dimensions and hence sheds some light on a certain design rules to optimize desirable shape-selective interactions.

Chapter 3 capitalizes on the fact that while the dynamics on nanoscale is hard to observe, dynamics of micron sized colloidal systems can be easily observed with conventional instruments like optical microscopy. These observations can be used to understand and study nanoscale interactions since depletion interactions exist on both nano and microscale. We employed PTVM technique to study depletion interactions in these colloidal systems in an effort to identify the electrolyte and polymer concentrations using the numerical models in the preceding chapter, to achieve the different kind of highly selective and preferential particle-surface or particle-particle interactions. The observed interactions were geometrically summarized using a color coded phase plot where every interaction has its region of exclusivity mapped on it. Also, it was found that

141

the model predictions of the order of depletion strength that is needed to achieve each of these different kinds of depletion attractions compared nicely with the experimental results. We also studied the rate of surface nucleation and identified the key parameters that can influence the rate: strength of the interactions and volume fraction of the larger species. On the whole, we were successfully able to use the numerical modeling studies in Chapter 2 as guidance to achieve the rich variety of depletion interactions in both bulk and non-bulk regions.

In Chapters 4 and 5, we aim to answer the question: "Does the softness of have an effect on the hydrodynamics of these particles when they are geometrically confined? Firstly, in Chapter 4, we investigated the hindered Brownian diffusion of hard PS colloids and soft, surfactant (SDS) laden toluene-swollen colloidal spheres between parallel walls over a wide range of degrees of confinement using PTVM and a simple yet effective experimental setup which uses monodispersed silica spacers to create uniform confined cells. We observed that the hydrodynamic coupling of both hard and swollen colloidal particles with confining walls suppresses their lateral diffusion significantly. While the experimental results for hard spheres were in excellent agreement with numerical predictions from existing models, SDS stabilized soft toluene-swollen colloidal spheres exhibited significant mobility under confinement compared to the hard PS particles, for all swelling ratios of the latex PS particles. It was observed that the hindrance to confined lateral diffusion decreased with increasing swelling ratio of the particles until a critical swelling ratio (CSR) is reached, above which all the particles behave almost identically. Even more striking is the observation that the drops above CSR diffuse at around 20% of their bulk diffusivities at super confinements when the unperturbed drop diameter is

142

larger than the wall spacing. Although numerical model predicting confined behavior exists for droplets, none of the models give a careful consideration for the deformation and their effects under confinement. To further illustrate the difference in hard and soft sphere behavior, a set of control experiments were performed with evaporating swollen spheres which clearly shows the transition from soft sphere to hard sphere behavior.

In Chapter 5, the confinement dynamics and the swelling curves of core/shell (PS/pNIPAm-co-AAc) microgels were studied using different parameters of interest that can influence the nature of the particle softness. It was shown that the C/S microgels exhibited significantly enhanced mobility under confinement compared to their hard sphere counterparts, which cannot be explained with current numerical models. It is suspected that the porous structure of the microgel shell allows water to penetrate, thus reducing the hydrodynamic coupling between sphere and wall. It was also determined that shell thickness, cross-linker concentration, porosity, pH and temperature can significantly affect the confinement dynamics of the C/S (PS/pNIPAm-co-AAc) microgels as they can influence the microgel swelling (soft) behavior. However, experimental data suggests that porosity is a more significant criterion for reducing their hindrance compared to shell thickness. To summarize, an increase in shell thickness and pH (up to 8.0) decreased the hindrance and increased the confined diffusivities while cross-linker concentration and temperature increased the hindrance causing them to behave like hard-spheres. Therefore, it was concluded that the composition of structure of the microgel network and the operating conditions have a huge impact on their confinement dynamics.

At the end of Chapters 4 and 5, a direct comparison of the experimental data of the hindrance coefficients of swollen spheres and C/S microgels suggests that the effect of internal flow and deformation in the toluene-swollen spheres exceeds the magnitude of the effect of porosity in the microgels under confinement. However, in order to truly compare the influence of these factors on the hindrance coefficients of soft spheres, one should compare the hindrance behavior of conventional drops (without surfactant) and conventional microgels without a core (with very low crosslink density).

6.2 Recommendations

The work described in these thesis Chapters raises several interesting questions that warrant additional experimental work beyond the scope of this thesis:

1. While we used our numerical models to distinguish between two kinds of geometrical interactions (cylinder-cylinder and dumbbell-dumbbell), there is still some works that needs to be done on controlling the preferential orientation within each of these interactions. For example, there are two major configurations possible for the case of dumbbell-dumbbell interactions: parallel configurations and crisscross configurations. Therefore, future work should be focused on controlling the preferential orientation for dumbbell-dumbbell geometry in order to favor one orientation over the other.

2. While our depletion experiments in Chapter 3 paved way for particle depositions on surfaces, these proposed studies did not examine the permanent deposition of the spherical particles onto surfaces of interest. Once the depositions are allowed to happen, it is important to permanently bind the particles to these positions for a durable self-assembly process. While using polystyrene (PS) particles as large

species, we suggest a mild annealing step above the polymer glass transition temperature (T_g) to cause the polymer to melt and secure the deposition. Since $T_g = 95°C$ for PS, aqueous solutions can no longer be used. Fleming *et al*. have demonstrated that heating PS colloids to 170–180 °C in ethylene glycol leads to the desired fusing of PS particles into a uniform coating [94]; we suggest these permanent depositions conditions should be further investigated.

3. In our depletion experiments in Chapter 3, edge nucleation on the structured silica templates was extremely rare and slow paced unlike surface and bulk nucleation due to the surface roughness caused by the Bosch process [195]. The surface roughness decreases the excluded volume overlap and can decrease the depletion strength by a large extent. It is suggested to use smoother and sharp structures in order to cause successful depletion interactions. Therefore, we believe edge nucleation was not thoroughly investigated in this thesis and it needs to be further investigated.

4. In Chapters 4 and 5, the confinement dynamics were investigated for surfactant covered toluene-swollen polystyrene particles and core/shell microgels. While we are trying to investigate the softness on the near wall hydrodynamics, these colloidal models used inherently possess a level of hardness due to the dissolved polystyrene in the swollen particles and the polystyrene core in the core/shell microgels. Also, the presence of a surfactant for the case of swollen spheres and a cross-linker concentration for C/S microgels minimizes the effect of internal circulation and porosity in each of these cases. In order to study the confinement dynamics of truly soft particles, it is suggested to use conventional emulsions (without surfactant) and microgels (very low cross-linker content) without any visco-elastic element

associated with them. Comparing the hindrance coefficients of conventional soft sphere systems would answer an important question – what is the most important criterion (among porosity, internal circulation or interfacial flow, and deformability) for reducing the hydrodynamic hindrance under confinement for soft sphere systems. These experiments would not only offer true fundamental insights regarding soft sphere behavior under confinement, but could also be useful to build numerical models that might explain their behavior. However, it is not a trivial undertaking to synthesize ultra-low cross-linker microgels and highly monodisperse conventional emulsion drops in the micrometer size range.

5. In Chapter 5, only mild confinement limits of microgels were explored to avoid sticky surface interactions with confining glass surfaces. It would be interesting to investigate the confinement dynamics of the C/S microgels under super-confined deformation regime where the unperturbed diameter is greater than the wall spacing. Just like emulsions, microgels are amenable to deformation, so we would expect deformation to play a role under super-confinement. Surface modifications on the glass surfaces negating such interactions would certainly help us research this problem.

6. Apart from the parameters of interest that were investigated in Chapter 5 affecting the confinement dynamics of C/S microgels under confinement, other parameters that might influence their softness and confinement dynamics are comonomer (AAc) concentration, ionic strength, surface charge density, etc. For example, microgels are known to swell more as the concentration of AAc increases[196].

7. In Chapter 4, SDS surfactant was used to avoid wetting issues and help create a repulsive barrier between the particles and glass surfaces. Presence of a surfactant on the particle's surface is known to affect the hydrodynamic interactions by altering the lubrication forces that makes these systems more complicated to understand [197]. Therefore, once again, the true nature of the soft spheres might not be revealed due to the presence of the surfactant. Also, many authors highlight interfacial cleanliness as being important to allow flow at the interface [123]. Using a surfactant can result in a no-slip or partial slip boundary condition impeding flow at the interface and hence increasing drag[8]. Henceforth, it is suggested to investigate the hydrodynamics of drop behavior in the absence of a surfactant near non-interacting surfaces.

8. In Chapters 4 and 5, direct experimental evidence for deformation/interface-mobility/porosity being responsible for softness enhanced confined diffusivities was not provided for both swollen particles and C/S microgel systems. Although, the mobility of the swollen spheres under super-confinement may be considered enough proof, it is still recommended that these hypotheses be supported with more experimental backing.

APPENDIX A

SUPPLEMENTARY INFORMATION FOR CHAPTER 4

1. Effect of Depletion Interactions on confinement dynamics of hard particles

Hard-PS confinement experiments with different SDS concentrations were performed to investigate the effect of SDS concentration on their confinement dynamics. It was found that the confinement dynamics were unaffected for concentrations less than the CMC (0.0082 M) of SDS. However, for conditions above the CMC, hindrance coefficients decreased for all confinements due to depletion interactions induced by the SDS micelles (depletants) between the PS particles and the neighboring confining surface. Therefore, above the CMC, a depletion interaction induces bias in the particle distributions (they no longer follow the Boltzmann distribution) by pushing them closer to the confining walls away from the midplane region and hence increases the wall hindrance. Also, as the concentration of the SDS increased above the CMC, hindrance
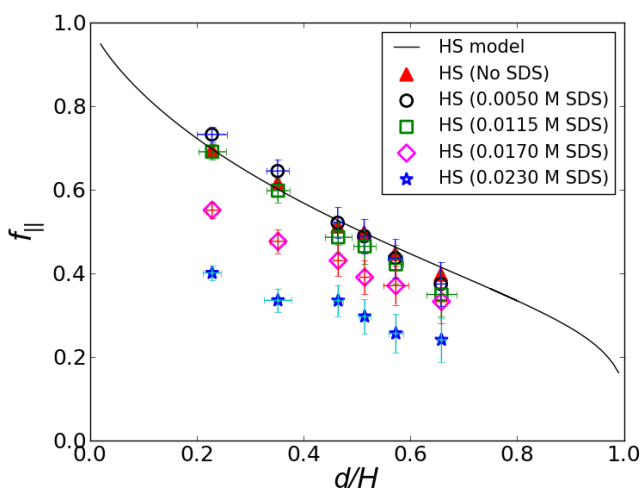
Figure A.1 Hindrance coefficients for 1.06 μm hard-PS for various concentrations of SDS aqueous solutions. Hindrance coefficients decrease above the CMC (0.0082M) of SDS due to depletion-induced wall interactions.

148

coefficients decreased dramatically. This suggests an increase in particle-wall depletion interactions due to the increase in concentration of SDS micelles. Therefore, to eliminate this effect, concentrations less than CMC were used for confinement of toluene-swollen PS spheres.

2. Effect of electrolyte concentration on confinement dynamics of hard particles

PS particles used in the confinement experiments are charge stabilized (0.0175 meq/g) due to carboxylate modified groups on the surface and therefore it is necessary to examine charge effects on their confinement dynamics. Hindrance coefficients were examined for various electrolyte concentrations and it is observed that there are no additional effects due to electrostatics to the wall-hindrance as the hindrance coefficients overlapped for DI water conditions and different electrolytic concentrations: 2 mM (κ^-
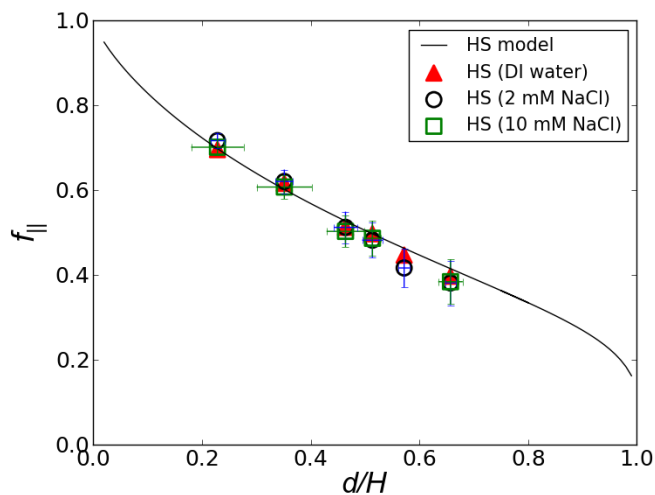
Figure A.2 Hindrance coefficients for 1.06 μm hard-PS at two different NaCl concentrations in comparison with DI water. Overlapping hindrance coefficients indicate that electrostatic effects are insignificant.

^{1}=6.7 nm) and 10 mM NaCl (κ^{-1}=3 nm) solutions.

REFERENCES

1.   Bigg, C., *Evident atoms: Visuality in Jean Perrin's Brownian motion research.* Studies in History and Philosophy of Science Part A, 2008. **39**(3): p. 312-322.

2.   Dieter, M.H., K. Ina, W. Patrick, and H.M. Dirk, *Colloids as model systems for metals and alloys: A case study of crystallization.* Journal of Physics: Condensed Matter, 2010. **22**(15): p. 153101.

3.   Löwen, H., *Melting, freezing and colloidal suspensions.* Physics Reports, 1994. **237**(5): p. 249-324.

4.   Aizenberg, J., P.V. Braun, and P. Wiltzius, *Patterned colloidal deposition controlled by electrostatic and capillary forces.* Physical Review Letters, 2000. **84**(13): p. 2997-3000.

5.   Leighton, D. and A. Acrivos, *Measurement of shear-induced self-diffusion in concentrated suspensions of spheres.* Journal of Fluid Mechanics, 1987. **177**: p. 109-131.

6.   Hotze, E.M., T. Phenrat, and G.V. Lowry, *Nanoparticle aggregation: Challenges to understanding transport and reactivity in the environment.* Journal of environmental quality, 2010. **39**: p. 1909-1924.

7.   Ivanov, I.B., K.D. Danov, and P.A. Kralchevsky, *Flocculation and coalescence of micron-size emulsion droplets.* Colloids and Surfaces A: Physicochemical and Engineering Aspects, 1999. **152**(1–2): p. 161-182.

8.   Dimiter, P., *Emulsions: Structure, stability and interactions*. 2004: Academic Press.

9.   Derjaguin, B. and L. Landau, *Theory of the stability of strongly charged lyophobic sols and of the adhesion of strongly charged particles in solutions of electrolytes.* Progress in Surface Science, 1993. **43**(1–4): p. 30-59.

10.   Verwey, E.J.W., *Theory of the stability of lyophobic colloids.* The Journal of Physical and Colloid Chemistry, 1947. **51**(3): p. 631-636.

11. Israelachvili, J.N., *6 - Van der Waals Forces*, in *Intermolecular and surface forces (third edition)*, J.N. Israelachvili, Editor. 2011, Academic Press: San Diego. p. 107-132.

12. Van Der Hoeven, P.C. and J. Lyklema, *Electrostatic stabilization in non-aqueous media.* Advances in Colloid and Interface Science, 1992. **42**(0): p. 205-277.

13. Roberts, G.S., R. Sanchez, R. Kemp, T. Wood, and P. Bartlett, *Electrostatic charging of nonpolar colloids by reverse micelles.* Langmuir, 2008. **24**(13): p. 6530-6541.

14. Gregory, J., *Interaction of unequal double layers at constant charge.* Journal of Colloid and Interface Science, 1975. **51**(1): p. 44-51.

15. Asakura, S. and F. Oosawa, *Interaction between particles suspended in solutions of macromolecules.* Journal of Polymer Science, 1958. **33**(126): p. 183-192.

16. Lekkerkerker, H.N.W. and R. Tuinier, *Colloids and the depletion interaction.* 2011: Springer.

17. Israelachvili, J.N. and R.M. Pashley, *Molecular layering of water at surfaces and origin of repulsive hydration forces.* Nature, 1983. **306**(5940): p. 249-250.

18. Israelachvili, J. and H. Wennerstrom, *Role of hydration and water structure in biological and colloidal interactions.* Nature, 1996. **379**(6562): p. 219-225.

19. Clunie, J.S., J.F. Goodman, and P.C. Symons, *Solvation forces in soap films.* Nature, 1967. **216**(5121): p. 1203-1204.

20. Mueller, S., E.W. Llewellin, and H.M. Mader, *The rheology of suspensions of solid particles*. Vol. 466. 2010. 1201-1228.

21. Royall, C.P., W.C.K. Poon, and E.R. Weeks, *In search of colloidal hard spheres.* Soft Matter, 2013. **9**(1): p. 17-27.

22. Vlassopoulos, D. and M. Cloitre, *Bridging the gap between hard and soft colloids.* Soft Matter, 2012. **8**(15): p. 4010-4013.

23.   Jose, J., G.A. Blab, A. van Blaaderen, and A. Imhof, *Jammed elastic shells - a 3D experimental soft frictionless granular system.* Soft Matter, 2015. **11**(9): p. 1800-1813.

24.   Brenner, H., *The slow motion of a sphere through a viscous fluid towards a plane surface.* Chemical Engineering Science, 1961. **16**(3–4): p. 242-251.

25.   Edwards, S.A., S.L. Carnie, O. Manor, and D.Y.C. Chan, *Effects of internal flow and viscosity ratio on measurements of dynamic forces between deformable drops.* Langmuir, 2009. **25**(6): p. 3352-3355.

26.   Cheremisinoff, N.P., *1 - An introduction to liquid filtration*, in *Liquid Filtration (Second Edition)*, N.P. Cheremisinoff, Editor. 1998, Butterworth-Heinemann: Woburn. p. 1-18.

27.   McDowell-Boyer, L.M., J.R. Hunt, and N. Sitar, *Particle transport through porous media.* Water Resources Research, 1986. **22**(13): p. 1901-1921.

28.   Pamme, N., *Continuous flow separations in microfluidic devices.* Lab on a Chip, 2007. **7**(12): p. 1644-1659.

29.   Goldman, A.J., R.G. Cox, and H. Brenner, *The slow motion of two identical arbitrarily oriented spheres through a viscous fluid.* Chemical Engineering Science, 1966. **21**(12): p. 1151-1170.

30.   MacKintosh, F.C. and C.F. Schmidt, *Microrheology.* Current Opinion in Colloid & Interface Science, 1999. **4**(4): p. 300-307.

31.   Waigh, T.A., *Microrheology of complex fluids.* Reports on Progress in Physics, 2005. **68**(3): p. 685.

32.   Mason, T.G. and D.A. Weitz, *Optical measurements of frequency-dependent linear viscoelastic moduli of complex fluids.* Physical Review Letters, 1995. **74**(7): p. 1250-1253.

33.   Chung, K., J.K. Cho, E.S. Park, V. Breedveld, and H. Lu, *Three-dimensional in situ temperature measurement in microsystems using Brownian motion of nanoparticles.* Analytical Chemistry, 2009. **81**(3): p. 991-999.

34.   Crocker, J.C. and D.G. Grier, *Methods of digital video microscopy for colloidal studies.* Journal of Colloid and Interface Science, 1996. **179**(1): p. 298-310.

35.   Cheezum, M.K., W.F. Walker, and W.H. Guilford, *Quantitative comparison of algorithms for tracking single fluorescent particles.* Biophysical Journal, 2001. **81**(4): p. 2378-2388.

36.   Breedveld, V. and D.J. Pine, *Microrheology as a tool for high-throughput screening.* Journal of Materials Science, 2003. **38**(22): p. 4461-4470.

37.   Dinsmore, A.D. and A.G. Yodh, *Entropic confinement of colloidal spheres in corners on silicon substrates.* Langmuir, 1999. **15**(2): p. 314-316.

38.   Lin, K.H., et al., *Entropically driven colloidal crystallization on patterned surfaces.* Physical Review Letters, 2000. **85**(8): p. 1770-1773.

39.   Badaire, S., C. Cottin-Bizonne, J.W. Woody, A. Yang, and A.D. Stroock, *Shape selectivity in the assembly of lithographically designed colloidal particles.* Journal of the American Chemical Society, 2007. **129**(1): p. 40-41.

40.   Churaev, N.V. and V.D. Sobolev, *Surface forces in nanostructures*, in *Nanoscience*. 2010, CRC Press. p. 3-29.

41.   N'guessan, H.E., et al., *Water tribology on graphene.* Nat Commun, 2012. **3**: p. 1242.

42.   Akbulut, M., *Nanoparticle-based lubrication systems.* Journal of Powder Metallurgy & Mining, 2012.

43.   Roca, J.F. and M.S. Carvalho, *Flow of a drop through a constricted microcapillary.* Computers & Fluids, 2013. **87**(0): p. 50-56.

44.   Fidalgo, L.M., et al., *From microdroplets to microfluidics: Selective emulsion separation in microfluidic devices.* Angewandte Chemie International Edition, 2008. **47**(11): p. 2042-2045.

45.   Shah, R.K., J.W. Kim, J.J. Agresti, D.A. Weitz, and L.Y. Chu, *Fabrication of monodisperse thermosensitive microgels and gel capsules in microfluidic devices.* Soft Matter, 2008. **4**(12): p. 2303-2309.

46.   Magnaudet, J., S. Takagi, and D. Legendre, *Drag, deformation and lateral migration of a buoyant drop moving near a wall.* Journal of Fluid Mechanics, 2003. **476**: p. 115-157.

47.   Collier, J.H., et al., *Thermally and photochemically triggered self-assembly of peptide hydrogels.* Journal of the American Chemical Society, 2001. **123**(38): p. 9463-9464.

48.   Strong, M., *Protein nanomachines.* PLoS Biol, 2004. **2**(3): p. e73.

49.   Minton, A.P., *Confinement as a determinant of macromolecular structure and reactivity. II. Effects of weakly attractive interactions between confined macrosolutes and confining structures.* Biophysical Journal, 1995. **68**(4): p. 1311-1322.

50.   Crocker, J.C., J.A. Matteo, A.D. Dinsmore, and A.G. Yodh, *Entropic attraction and repulsion in binary colloids probed with a line optical tweezer.* Physical Review Letters, 1999. **82**(21): p. 4352-4355.

51.   Sacanna, S., W.T.M. Irvine, P.M. Chaikin, and D.J. Pine, *Lock and key colloids.* Nature, 2010. **464**(7288): p. 575-578.

52.   Marenduzzo, D., K. Finan, and P.R. Cook, *The depletion attraction: an underappreciated force driving cellular organization.* The Journal of Cell Biology, 2006. **175**(5): p. 681-686.

53.   Gast, A.P. and W.B. Russel, *Simple ordering in complex fluids - Colloidal particles suspended in solution provide intriguing models for studying phase transitions.* Physics Today, 1998. **51**(12): p. 24-30.

54.   Iracki, T.D., D.J. Beltran-Villegas, S.L. Eichmann, and M.A. Bevan, *Charged micelle depletion attraction and interfacial colloidal phase behavior.* Langmuir, 2010. **26**(24): p. 18710-18717.

55.   Vrij, A., *Polymers at interfaces and the interactions in colloidal dispersions.* Pure and Applied Chemistry, 1976. **48**(4): p. 471-483.

56.   Ricci, F., A. Vallee-Belisle, and K.W. Plaxco, *High-precision, in vitro validation of the sequestration mechanism for generating ultrasensitive dose-response curves in regulatory networks.* Plos Computational Biology, 2011. **7**(10): p. 8.

57.   Dickman, R., P. Attard, and V. Simonian, *Entropic forces in binary hard sphere mixtures: Theory and simulation.* Journal of Chemical Physics, 1997. **107**(1): p. 205-213.

58.   Yodh, A.G., et al., *Entropically driven self–assembly and interaction in suspension.* Vol. 359. 2001. 921-937.

59.   Singh, R.P., B.R. Nayak, D.R. Biswal, T. Tripathy, and K. Banik, *Biobased polymeric flocculants for industrial effluent treatment.* Materials Research Innovations, 2003. **7**(5): p. 331-340.

60.   Sierra-Martin, B., et al., *Microscopic signature of a microgel volume phase transition.* Macromolecules, 2005. **38**(26): p. 10782-10787.

61.   Rosenberger, F., *Protein crystallization.* Journal of Crystal Growth, 1996. **166**(1-4): p. 40-54.

62.   Dickinson, E., *Special issue: Food emulsions and foams: Interfaces, interactions and stability.* Colloids and Surfaces B-Biointerfaces, 1999. **12**(3-6): p. 105-105.

63.   Talapin, D.V., J.S. Lee, M.V. Kovalenko, and E.V. Shevchenko, *Prospects of colloidal nanocrystals for electronic and optoelectronic applications.* Chemical Reviews, 2010. **110**(1): p. 389-458.

64.   Gast, A.P., C.K. Hall, and W.B. Russel, *Polymer-induced phase separations in non-aqueous colloidal suspensions.* Journal of Colloid and Interface Science, 1983. **96**(1): p. 251-267.

65.   Piasecki, J., L. Bocquet, and J.P. Hansen, *Multiple time-scale derivation of the Fokker-Planck equation for 2 Brownian spheres suspended in a hard-sphere fluid.* Physica A, 1995. **218**(1-2): p. 125-144.

66.   Biben, T., P. Bladon, and D. Frenkel, *Depletion effects in binary hard-sphere fluids.* Journal of Physics-Condensed Matter, 1996. **8**(50): p. 10799-10821.

67.   Chu, X.L., A.D. Nikolov, and D.T. Wasan, *Effects of particle size and polydispersity on the depletion and structural forces in colloidal dispersions.* Langmuir, 1996. **12**(21): p. 5004-5010.

68.   Gotzelmann, B., R. Evans, and S. Dietrich, *Depletion forces in fluids.* Physical Review E, 1998. **57**(6): p. 6785-6800.

69.   Bechinger, C., D. Rudhardt, P. Leiderer, R. Roth, and S. Dietrich, *Understanding depletion forces beyond entropy.* Physical Review Letters, 1999. **83**(19): p. 3960-3963.

70.   Rudhardt, D., C. Bechinger, and P. Leiderer, *Repulsive depletion interactions in colloid-polymer mixtures.* Journal of Physics-Condensed Matter, 1999. **11**(50): p. 10073-10078.

71.   Sharma, A. and J.Y. Walz, *Direct measurement of the depletion interaction in a charged colloidal dispersion.* Journal of the Chemical Society-Faraday Transactions, 1996. **92**(24): p. 4997-5004.

72.   Sober, D.L. and J.Y. Walz, *Measurement of long range depletion energies between a colloidal particle and a flat surface in micellar solutions.* Langmuir, 1995. **11**(7): p. 2352-2356.

73.   Van Helden, A.K., J.W. Jansen, and A. Vrij, *Preparation and characterization of spherical monodisperse silica dispersions in nonaqueous solvents.* Journal of Colloid and Interface Science, 1981. **81**(2): p. 354-368.

74.   Sharma, A. and J.Y. Walz, *Direct measurement of the depletion interaction in a charged colloidal dispersion.* Journal of the Chemical Society, Faraday Transactions, 1996. **92**(24): p. 4997-5004.

75.   Dinsmore, A.D., A.G. Yodh, and D.J. Pine, *Entropic control of particle motion using passive surface microstructures.* Nature, 1996. **383**(6597): p. 239-242.

76.   Wall, F.T., *Principles of polymer chemistry. Paul J. F.. Cornell Univ. Press, Ithaca, New York, 1953. 688 pp. Illus. $8.50.* Science, 1954. **119**(3095): p. 555-556.

77.   Bower, D.I., *An introduction to polymer physics*. 2002: Cambridge University Press.

78.   Meijer, E.J. and D. Frenkel, *Colloids dispersed in polymer-solutions - a computer-simulation study.* Journal of Chemical Physics, 1994. **100**(9): p. 6873-6887.

79.   Joanny, J.F., L. Leibler, and P.G. Degennes, *Effects of polymer-solutions on colloid stability.* Journal of Polymer Science Part B-Polymer Physics, 1979. **17**(6): p. 1073-1084.

80.   Eric, W. *Circle-circle intersection*. 1999; Available from: http://mathworld.wolfram.com/Circle-CircleIntersection.html.

81.   Rudhardt, D., C. Bechinger, and P. Leiderer, *Direct measurement of depletion potentials in mixtures of colloids and nonionic polymers.* Physical Review Letters, 1998. **81**(6): p. 1330-1333.

82.   Weronski, P., J.Y. Walz, and M. Elimelech, *Effect of depletion interactions on transport of colloidal particles in porous media.* Journal of Colloid and Interface Science, 2003. **262**(2): p. 372-383.

83.   Devanand, K. and J.C. Selser, *Asymptotic behavior and long-range interactions in aqueous solutions of poly(ethylene oxide).* Macromolecules, 1991. **24**(22): p. 5943-5947.

84.   Lee, J.H., H.B. Lee, and J.D. Andrade, *Blood compatibility of polyethylene oxide surfaces.* Progress in Polymer Science, 1995. **20**(6): p. 1043-1079.

85.   Musin, I.R., N. Shin, and M.A. Filler, *Diameter modulation as a route to probe the vapour-liquid-solid growth kinetics of semiconductor nanowires.* Journal of Materials Chemistry C, 2014. **2**(17): p. 3285-3291.

86.   Alder, B.J. and T.E. Wainwright, *Phase transition for a hard sphere system.* The Journal of Chemical Physics, 1957. **27**(5): p. 1208-1209.

87.	Prasad, V., D. Semwogerere, and E.R. Weeks, *Confocal microscopy of colloids.* Journal of Physics-Condensed Matter, 2007. **19**(11): p. 25.

88.	Behrens, S.H. and D.G. Grier, *The charge of glass and silica surfaces.* The Journal of Chemical Physics, 2001. **115**(14): p. 6716-6721.

89.	Borba, J.R., et al., *Quantitative characterization of hexagonal packings in nanoporous alumina arrays: A case study.* Journal of Physical Chemistry C, 2013. **117**(1): p. 246-251.

90.	Dinsmore, A.D., D.T. Wong, P. Nelson, and A.G. Yodh, *Hard spheres in vesicles: Curvature-induced forces and particle-induced curvature.* Physical Review Letters, 1998. **80**(2): p. 409-412.

91.	Laermer, F. and A. Schilp, *Method for anisotropic plasma etching of substrates.* 1996, Google Patents.

92.	Zhao, K. and T.G. Mason, *Directing colloidal self-assembly through roughness-controlled depletion attractions.* Physical Review Letters, 2007. **99**(26): p. 4.

93.	Ratke, L. and P.W. Voorhees, *Growth and coarsening: Ostwald ripening in material processing*. 15 ed, ed. B. Springer. 2002, Berlin.

94.	Fleming, M.S., T.K. Mandal, and D.R. Walt, *Nanosphere−microsphere assembly: Methods for core−shell materials preparation.* Chemistry of Materials, 2001. **13**(6): p. 2210-2216.

95.	Reynolds, O., *On the theory of lubrication and its application to Mr. Beauchamp tower's experiments, including an experimental determination of the viscosity of olive oil.* Philosophical Transactions of the Royal Society of London, 1886. **177**: p. 157-234.

96.	John, H. and B. Howard, *Low Reynolds number hydrodynamucs*. Vol. 1. 1973, Netherlands: Springer Netherlands.

97.	Goldman, A.J., R.G. Cox, and H. Brenner, *Slow viscous motion of a sphere parallel to a plane wall .I. Motion through a quiescent fluid.* Chemical Engineering Science, 1967. **22**(4): p. 637-&.

98.   Dufresne, E.R., D. Altman, and D.G. Grier, *Brownian dynamics of a sphere between parallel walls.* Europhysics Letters, 2001. **53**(2): p. 264-270.

99.   Uhlenbeck, G.E. and L.S. Ornstein, *On the theory of the Brownian motion.* Physical Review, 1930. **36**(5): p. 0823-0841.

100.   Deen, W.M., *Hindered transport of large molecules in liquid-filled pores.* AIChE Journal, 1987. **33**(9): p. 1409-1425.

101.   Goodman, T.T., C.P. Ng, and S.H. Pun, *3-D tissue culture systems for the evaluation and optimization of nanoparticle-based drug carriers.* Bioconjugate chemistry, 2008. **19**(10): p. 1951-1959.

102.   Ganatos, P., S. Weinbaum, and R. Pfeffer, *A strong interaction theory for the creeping motion of a sphere between plane parallel boundaries. Part 1. Perpendicular motion.* Journal of Fluid Mechanics, 1980. **99**(04): p. 739-753.

103.   Lobry, L. and N. Ostrowsky, *Diffusion of Brownian particles trapped between two walls: Theory and dynamic-light-scattering measurements.* Physical Review B, 1996. **53**(18): p. 12050-12056.

104.   Dufresne, E.R., T.M. Squires, M.P. Brenner, and D.G. Grier, *Hydrodynamic coupling of two Brownian spheres to a planar surface.* Physical Review Letters, 2000. **85**(15): p. 3317-3320.

105.   Eichmann, S.L., S.G. Anekal, and M.A. Bevan, *Electrostatically confined nanoparticle interactions and dynamics.* Langmuir, 2008. **24**(3): p. 714-721.

106.   Faucheux, L.P. and A.J. Libchaber, *Confined Brownian motion.* Physical Review E, 1994. **49**(6): p. 5158-5163.

107.   Lin, B., J. Yu, and S.A. Rice, *Direct measurements of constrained Brownian motion of an isolated sphere between two walls.* Physical Review E, 2000. **62**(3): p. 3909-3919.

108.   Feitosa, M.I.M. and O.N. Mesquita, *Wall-drag effect on diffusion of colloidal particles near surfaces: A photon correlation study.* Physical Review A, 1991. **44**(10): p. 6677-6685.

109. Cui, B., H. Diamant, B. Lin, and S.A. Rice, *Anomalous hydrodynamic interaction in a quasi-two-dimensional suspension.* Physical Review Letters, 2004. **92**(25): p. 258301.

110. Florin, E.L., A. Pralle, E.H.K. Stelzer, and J.K.H. Hörber, *Photonic force microscope calibration by thermal noise analysis.* Applied Physics A, 1998. **66**(1): p. S75-S78.

111. Saiki, Y., C.A. Prestidge, and R.G. Horn, *Effects of droplet deformability on emulsion rheology.* Colloids and Surfaces A: Physicochemical and Engineering Aspects, 2007. **299**(1–3): p. 65-72.

112. Bongaerts, J.H.H., K. Fourtouni, and J.R. Stokes, *Soft-tribology: Lubrication in a compliant PDMS–PDMS contact.* Tribology International, 2007. **40**(10–12): p. 1531-1542.

113. Clift, R.C., B.J. Grace, and M.E. Weber, *Bubbles, drops and particles.* 2005: Dover Publications.

114. Redfield, J.A. and G. Houghton, *Mass transfer and drag coefficients for single bubbles at Reynolds numbers of 0·02–5000.* Chemical Engineering Science, 1965. **20**(2): p. 131-139.

115. G, L.V., *Physicochemical hydrodynamics.* 1962, New Jersey: Prentice-Hall.

116. Ivanov, I.B., K.D. Danov, and P.A. Kralchevsky, *Flocculation and coalescence of micron-size emulsion droplets.* Colloids and Surfaces a-Physicochemical and Engineering Aspects, 1999. **152**(1-2): p. 161-182.

117. Travis, M.J., A. Gross, and N. Weisbrod, *Enhanced transport of colloidal oil droplets in saturated and unsaturated sand columns.* Environmental Science & Technology, 2011. **45**(21): p. 9205-9211.

118. Vlassopoulos, D. and M. Cloitre, *Tunable rheology of dense soft deformable colloids.* Current Opinion in Colloid & Interface Science, 2014. **19**(6): p. 561-574.

119. Zinchenko, A.Z. and R.H. Davis, *Chapter 10 - Hydrodynamical interaction of deformable drops*, in *Interface Science and Technology*, D.N. Petsev, Editor. 2004, Elsevier. p. 391-447.

120. Mulligan, M.K. and J.P. Rothstein, *The effect of confinement-induced shear on drop deformation and breakup in microfluidic extensional flows.* Physics of Fluids (1994-present), 2011. **23**(2): p. 022004.

121. Danov, K.D., N.D. Denkov, D.N. Petsev, I.B. Ivanov, and R. Borwankar, *Coalescence dynamics of deformable Brownian emulsion droplets.* Langmuir, 1993. **9**(7): p. 1731-1740.

122. Denkov, N.D., P.A. Kralchevsky, I.B. Ivanov, and C.S. Vassilieff, *Effect of droplet deformation on the interactions in microemulsions.* Journal of Colloid and Interface Science, 1991. **143**(1): p. 157-173.

123. Petsev, D.N., *Chapter 8 - Theory of emulsion flocculation*, in *Interface Science and Technology*, D.N. Petsev, Editor. 2004, Elsevier. p. 313-350.

124. Hofman, J.A.M.H. and H.N. Stein, *Destabilization of emulsions through deformation of the droplets.* Journal of Colloid and Interface Science, 1991. **147**(2): p. 508-516.

125. Tcholakova, S., N.D. Denkov, R. Borwankar, and B. Campbell, *Van der Waals interaction between two truncated spheres covered by a uniform layer (deformed drops, vesicles, or bubbles).* Langmuir, 2001. **17**(8): p. 2357-2362.

126. Vakarelski, I.U., et al., *Lateral hydrodynamic interactions between an emulsion droplet and a flat surface evaluated by frictional force microscopy.* Langmuir, 2010. **26**(11): p. 8002-8007.

127. Horn, R.G., M. Asadullah, and J.N. Connor, *Thin film drainage: Hydrodynamic and disjoining pressures determined from experimental measurements of the shape of a fluid drop approaching a solid wall.* Langmuir, 2006. **22**(6): p. 2610-2619.

128. Mulvaney, P., J.M. Perera, S. Biggs, F. Grieser, and G.W. Stevens, *The direct measurement of the forces of interaction between a colloid particle and an oil droplet.* Journal of Colloid and Interface Science, 1996. **183**(2): p. 614-616.

129. Aston, D.E. and J.C. Berg, *Quantitative analysis of fluid interface–atomic force microscopy.* Journal of Colloid and Interface Science, 2001. **235**(1): p. 162-169.

130. Dagastine, R.R. and L.R. White, *Forces between a rigid probe particle and a liquid interface: Ii. The general case.* Journal of Colloid and Interface Science, 2002. **247**(2): p. 310-320.

131. Tauer, K., *Latex particles*, in *Colloids and Colloid Assemblies*. 2004, Wiley-VCH Verlag GmbH & Co. KGaA. p. 1-51.

132. Morton, M., S. Kaizerman, and M.W. Altier, *Swelling of latex particles.* Journal of Colloid Science, 1954. **9**(4): p. 300-312.

133. Flory, P.I., *Thermodynamics of high polymer solutions.* Journal of Chemical Physics, 1942. **10**(1): p. 51-61.

134. Huggins, M.L., *Thermodynamic properties of solutions of high polymers: The empirical constant in the activity equation.* Annals of the New York Academy of Sciences, 1943. **44**(4): p. 431-443.

135. Skjeltorp, A.T., J. Ugelstad, and T. Ellingsen, *Preparation of nonspherical, monodisperse polymer particles and their self-organization.* Journal of Colloid and Interface Science, 1986. **113**(2): p. 577-582.

136. Farias-Cepeda, L., J. Herrera-Ordonez, and E. Saldivar-Guerra, *Effect of surfactant on the swelling of polymeric nanoparticles: Toward a generalized approach.* Colloid and Polymer Science, 2009. **287**(10): p. 1215-1220.

137. Liu, J., Q. Deng, and Y.C. Jean, *Free-volume distributions of polystyrene probed by positron annihilation: comparison with free-volume theories.* Macromolecules, 1993. **26**(26): p. 7149-7155.

138. Scholte, T.G., *Determination of thermodynamic parameters of polymer–solvent systems from sedimentation–diffusion equilibrium in the ultracentrifuge.* Journal of Polymer Science Part A-2: Polymer Physics, 1970. **8**(6): p. 841-868.

139. Shapira, M. and S. Haber, *Low Reynolds number motion of a drop between two parallel plates.* International Journal of Multiphase Flow, 1988. **14**(4): p. 483-506.

140. Keh, H.J. and P.Y. Chen, *Slow motion of a droplet between two parallel plane walls.* Chemical Engineering Science, 2001. **56**(24): p. 6863-6871.

141. Wegener, M., M. Kraume, and A.R. Paschedag, *Terminal and transient drop rise velocity of single toluene droplets in water.* AIChE Journal, 2010. **56**(1): p. 2-10.

142. Dagastine, R.R., G.W. Stevens, D.Y.C. Chan, and F. Grieser, *Forces between two oil drops in aqueous solution measured by AFM.* Journal of Colloid and Interface Science, 2004. **273**(1): p. 339-342.

143. Yang, H., C.C. Park, Y.T. Hu, and L.G. Leal, *The coalescence of two equal-sized drops in a two-dimensional linear flow.* Physics of Fluids (1994-present), 2001. **13**(5): p. 1087-1106.

144. Borrell, M., Y. Yoon, and L.G. Leal, *Experimental analysis of the coalescence process via head-on collisions in a time-dependent flow.* Physics of Fluids (1994-present), 2004. **16**(11): p. 3945-3954.

145. Podgórska, W., *Influence of dispersed phase viscosity on drop coalescence in turbulent flow.* Chemical Engineering Research and Design, 2007. **85**(5): p. 721-729.

146. Skelland, A.H.P. and Y.F. Huang, *Effects of surface active agents on fall velocities of drops.* The Canadian Journal of Chemical Engineering, 1977. **55**(3): p. 240-245.

147. Chesters, A.K. and I.B. Bazhlekov, *Effect of insoluble surfactants on drainage and rupture of a film between drops interacting under a constant force.* Journal of Colloid and Interface Science, 2000. **230**(2): p. 229-243.

148. Davis, R.H., J.A. Schonberg, and J.M. Rallison, *The lubrication force between two viscous drops.* Physics of Fluids A: Fluid Dynamics (1989-1993), 1989. **1**(1): p. 77-81.

149. Baldessari, F. and L.G. Leal, *Effect of overall drop deformation on flow-induced coalescence at low capillary numbers.* Physics of Fluids (1994-present), 2006. **18**(1): p. -.

150. Oolman, T.O. and H.W. Blanch, *Bubble coalescence in stagnant liquids.* Chemical Engineering Communications, 1986. **43**(4-6): p. 237-261.

151.   Chen, D., R. Cardinaels, and P. Moldenaers, *Effect of confinement on droplet coalescence in shear flow.* Langmuir, 2009. **25**(22): p. 12885-12893.

152.   Martin, J.D., J.N. Marhefka, K.B. Migler, and S.D. Hudson, *Interfacial rheology through microfluidics.* Advanced Materials, 2011. **23**(3): p. 426-432.

153.   Baker, W.O., *Microgel, a new macromolecule.* Industrial & Engineering Chemistry, 1949. **41**(3): p. 511-520.

154.   Bonnecaze, R.T. and M. Cloitre, *Micromechanics of soft particle glasses*, in *High Solid Dispersions*, M. Cloitre, Editor. 2010, Springer Berlin Heidelberg. p. 117-161.

155.   Vlassopoulos, D., G. Fytas, S. Pispas, and N. Hadjichristidis, *Spherical polymeric brushes viewed as soft colloidal particles: zero-shear viscosity.* Physica B: Condensed Matter, 2001. **296**(1–3): p. 184-189.

156.   Manghi, M., X. Schlagberger, Y.-W. Kim, and R.R. Netz, *Hydrodynamic effects in driven soft matter.* Soft Matter, 2006. **2**(8): p. 653-668.

157.   Tu, H., L. Hong, S.M. Anthony, P.V. Braun, and S. Granick, *Brush-sheathed particles diffusing at brush-coated surfaces in the thermally responsive PNIPAAm system.* Langmuir, 2007. **23**(5): p. 2322-2325.

158.   Wyss, H.M., T. Franke, E. Mele, and D.A. Weitz, *Capillary micromechanics: Measuring the elasticity of microscopic soft objects.* Soft Matter, 2010. **6**(18): p. 4550-4555.

159.   Adams, S., W.J. Frith, and J.R. Stokes, *Influence of particle modulus on the rheological properties of agar microgel suspensions.* Journal of Rheology (1978-present), 2004. **48**(6): p. 1195-1213.

160.   Borrega, R., M. Cloitre, I. Betremieux, B. Ernst, and L. Leibler, *Concentration dependence of the low-shear viscosity of polyelectrolyte micro-networks: From hard spheres to soft microgels.* EPL (Europhysics Letters), 1999. **47**(6): p. 729.

161.   Seth, J.R., M. Cloitre, and R.T. Bonnecaze, *Influence of short-range forces on wall-slip in microgel pastes.* Journal of Rheology (1978-present), 2008. **52**(5): p. 1241-1268.

162. Meeker, S.P., R.T. Bonnecaze, and M. Cloitre, *Slip and flow in pastes of soft particles: Direct observation and rheology.* Journal of Rheology, 2004. **48**(6): p. 1295-1320.

163. Meeker, S.P., R.T. Bonnecaze, and M. Cloitre, *Slip and flow in soft particle pastes.* Physical Review Letters, 2004. **92**(19): p. 4.

164. Wyss, H.M., J. Mattsson, T. Franke, A. Fernandez-Nieves, and D.A. Weitz, *Mechanics of single microgel particles*, in *Microgel Suspensions*. 2011, Wiley-VCH Verlag GmbH & Co. KGaA. p. 311-325.

165. Sierra-Martín, B., et al., *Microscopic signature of a microgel volume phase transition.* Macromolecules, 2005. **38**(26): p. 10782-10787.

166. Burmistrova, A., M. Richter, C. Uzum, and R. Klitzing, *Effect of cross-linker density of P(NIPAM-co-AAc) microgels at solid surfaces on the swelling/shrinking behaviour and the Young's modulus.* Colloid and Polymer Science, 2011. **289**(5-6): p. 613-624.

167. Chaterji, S., I.K. Kwon, and K. Park, *Smart polymeric gels: Redefining the limits of biomedical devices.* Progress in Polymer Science, 2007. **32**(8-9): p. 1083-1122.

168. Pan, Y.Z., H.Q. Bao, N.G. Sahoo, T.F. Wu, and L. Li, *Water-soluble Poly(N-isopropylacrylamide)-graphene sheets synthesized via click chemistry for drug delivery.* Advanced Functional Materials, 2011. **21**(14): p. 2754-2763.

169. Islam, M.R., A. Ahiabu, X. Li, and M.J. Serpe, *Poly (N-isopropylacrylamide) microgel-based optical devices for sensing and biosensing.* Sensors, 2014. **14**(5): p. 8984-8995.

170. Ho, H.T., et al., *Thermoresponsive block copolymers containing reactive azlactone groups and their bioconjugation with lysozyme.* Polymer Chemistry, 2013. **4**(3): p. 675-685.

171. Ohya, S., Y. Nakayama, and T. Matsuda, *Thermoresponsive artificial extracellular matrix for tissue engineering: Hyaluronic acid bioconjugated with poly(N-isopropylacrylamide) grafts.* Biomacromolecules, 2001. **2**(3): p. 856-863.

172.   Song, F., X.L. Wang, and Y.Z. Wang, *Fabrication of novel thermo-responsive electrospun nanofibrous mats and their application in bioseparation.* European Polymer Journal, 2011. **47**(10): p. 1885-1892.

173.   Destribats, M., et al., *Water-in-oil emulsions stabilized by water-dispersible poly(n-isopropylacrylamide) microgels: Understanding anti-finkle behavior.* Langmuir, 2011. **27**(23): p. 14096-14107.

174.   Zhang, F., G.H. Hou, S.J. Dai, R. Lu, and C.C. Wang, *Preparation of thermosensitive PNIPAM microcontainers and a versatile method to fabricate PNIPAM shell on particles with silica surface.* Colloid and Polymer Science, 2012. **290**(13): p. 1341-1346.

175.   Debord, S.B. and L.A. Lyon, *Influence of particle volume fraction on packing in responsive hydrogel colloidal crystals.* The Journal of Physical Chemistry B, 2003. **107**(13): p. 2927-2932.

176.   Serpe, M.J. and L.A. Lyon, *Optical and acoustic studies of pH-dependent swelling in microgel thin films.* Chemistry of Materials, 2004. **16**(22): p. 4373-4380.

177.   Wiedemair, J., et al., *In-situ AFM studies of the phase-transition behavior of single thermoresponsive hydrogel particles.* Langmuir, 2007. **23**(1): p. 130-137.

178.   Fernández-Nieves, A., A. Fernández-Barbero, B. Vincent, and F.J. de las Nieves, *Charge controlled swelling of microgel particles.* Macromolecules, 2000. **33**(6): p. 2114-2118.

179.   Cho, J.K., Z. Meng, L.A. Lyon, and V. Breedveld, *Tunable attractive and repulsive interactions between pH-responsive microgels.* Soft Matter, 2009. **5**(19): p. 3599-3602.

180.   Gan, D.J. and L.A. Lyon, *Tunable swelling kinetics in core-shell hydrogel nanoparticles.* Journal of the American Chemical Society, 2001. **123**(31): p. 7511-7517.

181.   Jones, C.D. and L.A. Lyon, *Synthesis and characterization of multiresponsive core-shell microgels.* Macromolecules, 2000. **33**(22): p. 8301-8306.

182. Andersson, M. and S.L. Maunu, *Structural studies of Poly(N-isopropylacrylamide) microgels: Effect of SDS surfactant concentration in the microgel synthesis.* Journal of Polymer Science Part B-Polymer Physics, 2006. **44**(23): p. 3305-3314.

183. McPhee, W., K.C. Tam, and R. Pelton, *Poly(N-isopropylacrylamide) latices prepared with sodium dodecyl-sulfate.* Journal of Colloid and Interface Science, 1993. **156**(1): p. 24-30.

184. Dingenouts, N., et al., *Analysis of thermosensitive core-shell colloids by small-angle neutron scattering including contrast variation.* Physical Chemistry Chemical Physics, 2001. **3**(7): p. 1169-1174.

185. Senff, H., W. Richtering, C. Norhausen, A. Weiss, and M. Ballauff, *Rheology of a temperature sensitive core−shell latex.* Langmuir, 1999. **15**(1): p. 102-106.

186. Zhou, Z., et al., *Effects of particle softness on shear thickening of microgel suspensions.* Soft Matter, 2014. **10**(33): p. 6286-6293.

187. Vermant, J. and M.J. Solomon, *Flow-induced structure in colloidal suspensions.* Journal of Physics: Condensed Matter, 2005. **17**(4): p. R187.

188. Shah, R.K., J.W. Kim, and D.A. Weitz, *Monodisperse stimuli-responsive colloidosomes by self-assembly of microgels in droplets.* Langmuir, 2010. **26**(3): p. 1561-1565.

189. Varga, I., T. Gilányi, R. Mészáros, G. Filipcsei, and M. Zrínyi, *Effect of cross-link density on the internal structure of Poly(N-isopropylacrylamide) microgels.* The Journal of Physical Chemistry B, 2001. **105**(38): p. 9071-9076.

190. Kratz, K., T. Hellweg, and W. Eimer, *Structural changes in PNIPAM microgel particles as seen by SANS, DLS, and EM techniques.* Polymer, 2001. **42**(15): p. 6631-6639.

191. Carregal-Romero, S., N.J. Buurma, J. Pérez-Juste, L.M. Liz-Marzán, and P. Hervés, *Catalysis by Au@PNIPAM nanocomposites: Effect of the cross-linking density.* Chemistry of Materials, 2010. **22**(10): p. 3051-3059.

192.   Bradley, M. and B. Vincent, *Interaction of nonionic surfactants with copolymer microgel particles of NIPAM and acrylic acid.* Langmuir, 2005. **21**(19): p. 8630-8634.

193.   Saunders, B.R. and B. Vincent, *Microgel particles as model colloids: theory, properties and applications.* Advances in Colloid and Interface Science, 1999. **80**(1): p. 1-25.

194.   Kratz, K., T. Hellweg, and W. Eimer, *Influence of charge density on the swelling of colloidal poly(N-isopropylacrylamide-co-acrylic acid) microgels.* Colloids and Surfaces A: Physicochemical and Engineering Aspects, 2000. **170**(2–3): p. 137-149.

195.   Bhardwaj, J.K., L.M. Lea, and E. Guibarra, *Plasma processing wafer, especially for highly anisotropic etches for high aspect ratio trenches, by cyclically adjusting processing parameters between first and second steps and stabilizing plasma during transition.* Surface technology systems Ltd. (surf-non-standard). p. 1088329-A1:.

196.   Burmistrova, A., M. Richter, M. Eisele, C. Üzüm, and R. von Klitzing, *The effect of co-monomer content on the swelling/shrinking and mechanical behaviour of individually adsorbed PNIPAM microgel particles.* Polymers, 2011. **3**(4): p. 1575-1590.

197.   Mewis, J. and N.J. W., *Colloidal suspension rheology.* 2011: Cambridge University Press.